

Ludwig-Maximilians-Universität München



**ROTATIONAL MOTIONS IN SEISMOLOGY:
THEORY, OBSERVATION, MODELING**

Dissertation
zur Erlangung des Doktorgrades
der Fakultät für Geowissenschaften der
Ludwig-Maximilians-Universität München

vorgelegt von
Nguyen Dinh Pham

am
23. Juli 2009

1. Gutachter: Prof. Dr. Heiner Igel
 2. Gutachter: Prof. Dr. Ulrich Schreiber
- Tag der mündlichen Prüfung: 05/11/2009

Contents

Acknowledgments	v
Summary	vii
Introduction	1
Chapter 1. The Effects of Tilt on Interferometric Rotation Sensors	7
Abstract	7
1.1 Introduction	8
1.2 Tilt - Ring Laser Coupling: Theory	9
<i>1.2.1 Observations of Local Earthquakes</i>	11
<i>1.2.2 Observations of Tele-Seismic Events</i>	16
1.3 Tilt - Ring Laser Coupling: Observations in the P Coda	19
1.4 Discussion and Conclusions	23
Chapter 2. Observations and Modeling of Rotational Signals in the P Coda: Constraints on Crustal Scattering	27
Abstract	27
2.1 Introduction	28
2.2 Observations	29
<i>2.2.1 Database</i>	29
<i>2.2.2 Frequency Dependence of Direct Observations</i>	30

2.2.3 Increase in Correlation Right After the Onset of P Wave	33
2.2.4 Frequency Dependence of Correlation	33
2.2.5 Directional Dependence of Correlation	35
2.2.6 Envelopes	41
2.2.7 Energy Equipartitioning	41
2.3 Modeling	45
2.3.1 P-SH Scattering in the 3D Random Crust	46
2.3.2 Topographic Scattering	52
2.4 Discussion and conclusions	54
Chapter 3. Rotational Motions in Homogeneous Anisotropic Elastic Media	57
Abstract	57
3.1 Introduction	58
3.2 Fundamental Theory	59
3.3 Rotation Rates of qP Waves in TI Media: Analytical Expression and Numerical Simulations	64
3.4 Quantification of Peak Rotation Rates of qP Waves in Terms of Thomsen Parameters	67
3.5 Estimation of Peak qP Rotation Rate Values for Weakly Anisotropic Media	72
3.6 Extracting Anisotropic Parameters from Point Measurements of Translational and Rotational Motions of qP Waves	77
3.7 Discussion and Conclusions	80
Outlook	83
Data and Resources	85

Appendix A. Variations of the Normal Unit Vector of a Ring Laser	87
Appendix B. Axis Transformations of Tilts	93
Appendix C. Fundamental Formulas	95
Appendix D. Orthogonal System l, θ, ϕ	97
Bibliography	99
Curriculum Vitae	107

Acknowledgments

I would like to express my gratitude to all those who have made this thesis possible. First of all to my supervisor, Prof. Heiner Igel, for providing me the opportunity to do a doctorate in the Seismology Group at the LMU Munich, for his nice guidance, valuable advice and for raising the first idea for this very interesting and scientifically rich PhD project. I am very grateful for everything that I learned from him. I am also very happy that he totally supported me to attend many international conferences where I learned a lot from a large number of scientists from all over the world and obtained a broad overview of seismology.

Many thanks to Prof. Ulrich Schreiber for accepting to be my second supervisor, and for his outstanding contributions to the installation and operation of the G ring laser at the Geodetic Observatory Wettzell which provides an excellent database not only for geodesists but also for seismologists like me to study further on rotational seismology.

Many thanks also to Martin Käser for accepting to revise and evaluate this thesis, especially for allowing me to use the *SeisSol* code, helping me a lot in applying this code to my studies as well as in publishing my results.

A big and special “*thank you*” to Josep de la Puente, one of my office mates, who helps me a lot in various ways during my whole study period at LMU Munich. All the topics in my dissertation, more or less, bear his impress. I am very thankful to him for the pleasing, intelligent discussions, suggestions, and comments.

Thanks a lot to František Gallovič for providing the code to create random media. Also to Joachim Wassermann, Alain Cochard, Michael Campillo, Nicolai Shapiro, Christoph Sens-Schönfelder for their interesting discussions and comments.

Thanks to all wonderful people at the Department of Earth and Environmental Sciences, LMU Munich, especially to my colleagues at the Seismological Group and my office mates Marco Stupazzini, Verena Hermann, Christian Pelties, and again Josep de la Puente for sharing many stuffs and helping me in many ways.

I strongly acknowledge the Project 322 of the Vietnamese Government and all people who have made it possible. It has provided very nice opportunities to PhD students like me to obtain the best education one could ever wish. The German

Academic Exchange Service (DAAD), the Geophysics Section - LMU Munich, Institute of Geophysics – Vietnamese Academy of Science and Technology, and the European Human Resources Mobility Program (SPICE project) are particularly acknowledged for efficient supports during the time I study in Munich, Germany.

The KONWIHR project and the Munich Supercomputing Center LRZ are acknowledged for computational resources. Also thanks to the excellent IT support at Geophysics in Munich.

The acknowledgement is also addressed to the contributions of the Bundesamt für Kartographie und Geodäsie (BKG) towards the installation and operation of the G ring laser at the Geodetic Observatory Wettzell.

Special thanks to my wonderful Vietnamese relatives and friends in Germany bMan, cHà, chSon, my tiny friends Tí, Tùm, chMạnh, Hoa, Phương, aTân, aDũng, Việt, Cương, and all members in the DAAD-Lớp-tiếng-Đức group for sharing lots of good and bad moments and giving me a lot of help in many ways.

Finally, very especially to all members in my loving family, my parent, my wife Giang, my children Cún, Bổng, and my sister and brother Ngọc, Hải for their constant love and support.

München, July 2009
Pham, Dinh Nguyen

Summary

Theoretically, to fully describe the change in the medium around a point one needs three components of translation, six components of strain, and three components of rotation. It is expected that collocated measurements of translations and rotations may help (1) correcting translation signals recorded by classical seismometers for contamination by ground rotations, (2) extracting additional information on earthquake source properties, soil-structure interactions, and properties of the subsurface, and (3) providing additional ground motion information to earthquake engineers for seismic design. Thus, in addition to translations and strains, the rotational part of ground motions should also be recorded. However, the lack of instrumental sensitivity did not allow seismologists to observe rotational motions for decades. Recently, ring laser technology has provided the means to develop instruments that allow in principle the observation of rotational motions in a wide frequency band and epicentral distance range.

Here we present the observations of rotational ground motions around a vertical axis in the P coda (the section between the onsets of direct P- and S- waves) of tele-seismic signals on a ring laser sensor at the Fundamental Observatory Wettzell, southeast Germany. The studies focus on finding the explanation for the observed P coda rotations as well as the way to extract additional information from the use of co-seismic rotational motions. First, the effects of co-seismic tilts on ring laser measurements are quantified based on magnitude-amplitude relations and translation derived tilts. Then the phenomenon of scattering assuming three dimensional random media and topography that may generate the observed P coda rotations is investigated through analysis of observations and forward modelling. The partitioning of P and S energy indicated by the stabilization of the ratio of energies of the two is used to constrain scattering properties. Finally, an analytical approach focusing on the solution of plane waves in linear elastic anisotropic media is used to quantify the anisotropic behavior through the variations of rotational wavefield. The focus is on quasi-P waves and transverse isotropic media. Kelvin-Christoffel equation and the Thomson parameters, descriptive of the degree of anisotropy, are used. The obtained results show that 1) P-SH scattering in the random crust is the main cause of the P-coda observations; and 2)

rotational motions contain additional information (at least) about scattering properties and anisotropic coefficients and that joint measurements of translational and rotational motions at only one point allow the extraction of additional information. The results demonstrate the potential benefit not only of measurements of co-seismic rotational ground motions but also of the use of the amplitude content of seismic signals.

Introduction

Seismology is the study of the generation, propagation, and recording of elastic waves. It is primarily based on the observation, processing, and inversion of three orthogonal components of translational ground motions (displacement, velocity, or acceleration). Theoretically, to fully describe the change in the medium around a point one needs not only three components of translation but also six components of strain, and three components of rotational motions (see Aki and Richards, 2002; Stein and Wysession, 2003; Cochard et al., 2006). Here, strain indicates a symmetric tensor describing the internal deformations and its tensor components are spatial derivatives of the translational displacement field. Rotational motions are defined as half of the curl of the translational field (Lay and Wallace, 1995; Aki and Richards, 2002; Stein and Wysession, 2003; Cochard et al., 2006). Although geophysical studies associated with translational motions and strain attain a lot of success, the full benefits of rotational motions are still under investigation and this type of signal has been ignored for a long time. It is, at first, because there was a widespread belief that rotational motions are insignificant (Bouchon and Aki, 1982; see also Lee et al., 2009a). For example, Richter (1958) stated that “*theory indicates, and observation confirms, that such rotations are negligible*”. And structural damages associated with earthquakes together with rotations were explained by the asymmetry of the structure (see Suryanto, 2006). However, several field evidences suggest that it is at least not always the case (Galitzin, 1914; Newmark, 1969). The rotation of the monument to George Inglis (erected in 1850 at Chatak, India) as observed by Oldham, 1899 after the 1897 Great Shillong earthquake (see Lee et al., 2009a) revealed that rotational ground motions may contribute to co-seismic structural damages. Moreover, amplitudes of rotation rate and co-seismic translational acceleration are scaled by phase velocity (Cochard et al., 2006). Hence, in the medium whose wave velocity is very small (e.g., soft sediment), rotations might become large and be responsible for structural damage.

This indicates that in addition to translations and strain, rotational ground motions should also be measured (see also Aki and Richards, 2002). This type of

2 INTRODUCTION

observation might be relevant for: (1) correcting translation signals recorded by classical seismometers for contamination by ground rotations (Graizer, 2005; Graizer, 2006; Pillet and Virieux, 2007; Pillet et al., 2009); (2) extracting additional information on earthquake source properties (e.g., Takeo and Ito, 1997; Takeo, 1998), soil-structure interactions (Trifunac and Todorovska, 2001), and properties of the subsurface (Igel et al., 2007; Pham et al., 2009b; Fichtner and Igel, 2009; Bernauer et al., 2009); (3) providing additional ground motion information to earthquake engineers for seismic design (e.g., Awad and Humar, 1984; Li et al., 2001, 2002; Trifunac, 2009). Nevertheless, rotational motions have still been ignored until recently because sensitive measuring sensors were not available. Aki and Richards (1980) pointed out that “*the state-of-the-art sensitivity of the general rotation sensor is not yet enough for a useful geophysical application*”.

Early attempts to observe ground rotations with solid state rotational velocity sensors and fiber-optical gyros were made by Nigbor (1994) and Takeo (1998). However, these observations were limited to large signals close to the sources of strong events (explosion or earthquake) and did not lead so far to an instrument of general interest (see Cochard et al., 2006; Lee et al., 2009a). Several authors tried to derive the rotational components of ground motions from measurements of appropriately sized seismic arrays (Spudich *et al.*, 1995; Singh *et al.*, 1997; Huang, 2003) but never compared to direct measurements of rotations until recently (Suryanto *et al.*, 2006) when consistent rotational observations of a ring laser sensor around a vertical axis become available. The pioneering observations of earthquake induced ground rotations with ring laser sensors were made by Stedman et al. (1995), Stedman (1997), McLeod et al. (1998), and Pancha et al. (2000). Using collocated measurements of ring laser and seismometer for several large earthquakes at Christchurch, New Zealand they were the first to investigate the relationship between translational acceleration and rotation rate under the assumption of plane horizontally polarized wave propagation. They showed that the optical sensors indeed provide sufficient sensitivity to record earthquake induced rotations. Unfortunately, their rotational observations were not fully consistent in phase and amplitude with translational motions in a broad frequency band of interest. This explains for the statement by Aki and Richards (2002) that “*as of this writing seismology still awaits a suitable instrument for making such measurements*”.

Recently, following advances in developing instruments that record rotational motions around one or all three orthogonal axes, consistent observations of rotational ground motions are becoming possible (Schreiber et al., 2005, 2006, 2009; Igel et al., 2007; Nigbor et al., 2009; Wassermann et al., 2009). Especially, the G ring laser sensor is reported as a suitable instrument for making rotational

measurements in seismology that Aki & Richards (2002) were waiting for (Igel et al., 2007). As a consequence, studies based on collocated measurements of both translational and rotational ground motions that try to exploit the new type of information grow rapidly (e.g., Igel et al., 2005, 2007; Cochard et al., 2006; Suryanto, 2006; Pham et al., 2009a, 2009b; Ferreira and Igel, 2009; Fichtner and Igel, 2009; Bernauer et al., 2009). Results of those studies are reviewed by Lee et al. (2009a,b) indicating the emergence of a new branch in observational seismology and earthquake engineering.

One of the key questions to be raised for rotational seismologists is: what additional information – compared to standard translational observations – can be extracted and how? Early studies (Takeo and Ito, 1997) indicated that earthquake rupture histories can be better constrained with measurements of rotational motions. Furthermore, the multi-component point measurements of both rotational and translational motions allow the estimation of wave field properties (e.g. phase velocities, propagation direction, Igel et al., 2007, Cochard et al., 2006), and allow the recovery of shear wave structure without travel time information (Fichtner and Igel, 2009 and Bernauer et al., 2009), as well as allow constraining the scattering properties of the near-receiver crustal structure (Pham et al., 2009b – this study).

Analyzing collocated measurements of both the G ring laser sensor and the broad band seismometer deployed at the Fundamental Wettzell Observatory, southeast Germany, Igel et al. (2007) are the first to recognize that there is a significant rotational motion component around the vertical axis in the P coda of seismic signals. At first, this is a surprising observation because, theoretically, in spherically symmetric isotropic media P and SV waves do not generate rotations around the vertical axis so we should not observe this kind of motions before the arrival times of SH waves. There are several possible explanations for the phenomenon of P coda rotations: (1) tilt – ring laser coupling: when P waves arrive they do generate tilts at the Earth's surface (i.e. rotational motions around horizontal axes). This will contaminate the ring laser measurements through changes of the surface normal with respect to the Earth's rotation axis and may potentially contribute to the phenomenon of rotation in the P coda (Schreiber et al., 2005; Igel et al., 2007); (2) P-SH scattering in the crust; (3) topographic scattering; and (4) anisotropic effects. At the onset of this work, there were several open questions: 1) What is the main cause of the observed P coda rotations? 2) Can we reproduce the observations (i.e., P coda rotations)? 3) Do P coda rotations contain additional information compared to standard translational observations? 4) What can be constrained from both types of translational and rotational measurements? 5) Can an inverse problem be set up that allows the recovery of subsurface properties from a point multi-component measurement only?

4 INTRODUCTION

The main goals of this work are: 1) to present the ring laser observations of rotational ground motions around a vertical axis in the P coda; 2) to understand the origin of the observed P coda rotations; and 3) to investigate the possibility to extract additional information from the use of co-seismic rotational motions.

The thesis is structured in three major chapters, arranged as follows:

Chapter 1: The effects of tilt on interferometric rotation sensors. This chapter aims at investigating quantitatively the effects of co-seismic tilts on ring laser measurements. The focus is on tilt-ring laser coupling in general with specific applications to local and tele-seismic events. The tilt-ring laser coupling is evaluated based on the comparison with the corresponding vertical rotation rate. Because correct measurements of co-seismic tilt are not available, investigations on theoretical tilt-ring laser coupling and estimates of the effects are based on magnitude-amplitude relations to be expected for observations of local earthquakes and tele-seismic events. The application of the theory to the observations in the P coda is also presented. Finally, tilt-ring laser coupling in the P coda of several observed events is estimated based on translation derived tilts (Li et al. 2001). The results of this chapter show that the effects of tilt on ring laser sensors can be neglected for observations of tele-seismic events and for the applicable range of the local magnitude scale.

Chapter 2: Observations and modeling of rotational signals in the P-Coda: constraints on crustal scattering. The goals of this chapter are to present the ring laser observations of P coda rotational ground motions and to investigate the effects of P-SH scattering in the crust as well as of topographic scattering on rotational ground motions around the vertical axis. In this chapter the observed P coda rotations are investigated systematically by examining their energy variations as a function of frequency, incoming direction, and time. The frequency and directional dependence of the P coda rotations is revealed using the zero-phase butterworth first-order filtering and cross-correlation techniques. Normalized envelopes are used to investigate time-dependent variations of energy in the P coda rotations. Furthermore, forward modeling in three dimensional media is implemented to study the generation of P coda rotations under the assumption of P-SH scattering in the crust and of topographic scattering, separately. Seismograms of three components of rotation rate and three components of translational velocity are calculated using the ADER-DG method (the combination of a Discontinuous Galerkin finite element method and an Arbitrary high-order DERivative time integration approach developed by Dumbser and Käser, 2006). The partitioning of P and S energy and the stabilization of the ratio between the two are used to compare the modeling results

with the observations. The results from detailed analysis of the observation and simulation signals show that P-SH scattering in the crust can explain the P coda observations and, under the assumption of this, scattering properties of the crust can be constrained. The contributions of topography scattering on the observed P coda rotations are shown to be small and can be ignored.

Chapter 3: Rotational motions in homogeneous anisotropic elastic media. In this chapter, expected amplitudes of rotational motions in various situations of anisotropy and their dependence on propagation direction are predicted. The main goals are to understand the contributions of anisotropic effects on the observed P coda rotations and to investigate the possible use of collocated measurements of rotational and translational motions for extracting anisotropic properties. The problem is approached in an analytical way focusing on the solution of the wave question for plane waves in linear elastic anisotropic media. The focus is on quasi-P waves and transverse isotropic media. Kelvin-Christoffel equation and the Thomson parameters, descriptive of the degree of anisotropy, are used. The results obtained in this study not only contribute to understanding the origin of the observed P coda rotations but also demonstrate that rotational motions contain additional information about anisotropy and that joint measurements of translational and rotational motions of qP waves at only one point in anisotropic media allow (in theory, at least) constraining anisotropic parameters independently of travel time information, thus might further allow one to recover time dependent changes in anisotropy which may be a matter of interest for volcano and earthquake forecasts.

The above three chapters are presented as three independent papers (Pham et al., 2009a,b,c), thus each one includes its own abstract, introduction, discussions and conclusions. A final **Outlook** will summarize the conclusions of this thesis as well as considerations concerning open problems for future research.

Appendices provide additional information on the basic equations and the coordinate system used.

The numerical simulation results shown in this thesis have been computed by using the *SeisSol* software which is programmed in Fortran90 and uses MPI libraries for parallel computation. The software is a strongly modified version of the original *HydSol* code developed at the Institute of Aerodynamics and Gasdynamics (IAG) Stuttgart, adapted to the seismic wave propagation problem by Dumbser and Käser (2006), and extended for complex rheologies by de la Puente (2008). The facilities at the Munich Leibniz Supercomputing Centre (LRZ) have been used to produce final numerical results.

Chapter 1

The Effects of Tilt on Interferometric Rotation Sensors^{*}

Abstract

Ring laser rotation sensors are contaminated by rotations around horizontal axes (also called tilts) through the vector product between the local normal direction and the vector of the rotation rate composed of Earth's rotation and local ground rotations. In this study, we investigate theoretically this cross-axis sensitivity and estimate the effects based on magnitude-amplitude relations to be expected for observations of local earthquakes and tele-seismic events. We investigate tilt-ring laser coupling for rotational motions in the P coda of several past earthquakes using tilt motions derived from observed translations. The results show that compared to the corresponding vertical rotation rate tilt-ring laser coupling is negligible for observations of tele-seismic events and for the applicable range of the local magnitude scale.

^{*} The contents of this chapter have been published in Pham D.N., H. Igel, J. Wassermann, A. Cochard, U. Schreiber, 2009, The effects of tilt on interferometric rotation sensors, *Bull. Seismol. Soc. Am.*, 99, no. 2B, 1352-1365, doi: 10.1785/0120080181.

1.1 Introduction

With ring laser technology seismologists can now observe rotational ground motions for a wide magnitude and distance range (Pancha et al., 2000; Schreiber et al., 2005, 2006; Igel et al., 2005, 2007). Amplitudes of ring laser rotational signals are used to estimate phase velocities (Igel et al., 2007), or constrain subsurface properties (Pham et al., 2008; Fichtner and Igel, 2008). Moreover, amplitude and waveform modelling of rotational motions requires quantitative understanding of all factors contributing to the signals. Therefore, each effect that contributes to ring laser measurements has to be considered carefully.

Although ring laser rotation sensors are built to be insensitive to translations, their records are contaminated by horizontal components of rotations or co-seismic tilts (McLeod et al., 1998; Schreiber et al., 2005, 2006, 2009). Tilt-ring laser coupling therefore may potentially contribute to ring-laser measurements. However, this effect has so far not been looked at in a quantitative way or in connection with observed rotations. In addition, previous rough estimates of tilt-ring laser coupling were erroneously based on tiltmeter measurements that are primarily sensitive to horizontal acceleration in the frequency band considered.

The main goal of this study is to investigate quantitatively the effects of co-seismic tilts on ring laser measurements. While the problem in itself deserves attention, the main motivation for the present study comes from observation of rotational motions in the P coda (Igel et al., 2007; Pham et al., 2009b). In order to understand the origin of these signals all potential contributions need to be quantified. In the present study the focus is on tilt-ring laser coupling in general with specific applications to local and tele-seismic events. The tilt-ring laser coupling is evaluated based on the comparison with the corresponding vertical rotation rate. Thus, the so-called significant (or negligible) tilt-ring laser coupling in this study means the tilt-ring laser coupling to be significant (or negligible) compared to the corresponding vertical rotation rate.

We first investigate theoretically tilt-ring laser coupling and perform estimates of the effects based on magnitude-amplitude relations to be expected for observations of local earthquakes and tele-seismic events. We then apply the theory to the observations in the P coda. We estimate tilt-ring laser coupling in the P coda of several observed events based on translation derived tilts (Li et al., 2001). We conclude that the effects can be neglected for observations of tele-seismic events and for the applicable range of the local magnitude scale.

1.2 Tilt - Ring Laser Coupling: Theory

Ring laser sensors allow us to observe rotational ground motions with high accuracy through the Sagnac effect (Schreiber et al., 2005, 2006; Igel et al., 2007):

$$\Delta f = \frac{4A}{\lambda P} \mathbf{n}_R \cdot \dot{\mathbf{\Omega}} \quad (1.1)$$

where A , P , and \mathbf{n}_R , respectively, are area, perimeter and normal unit vector of the ring laser, $\dot{\mathbf{\Omega}}$ is the vector of the imposed rotation rate, λ is laser wavelength, Δf is the Sagnac frequency.

Equation (1.1) is called the Sagnac equation demonstrating that there are three contributions that influence the Sagnac frequency Δf : 1) changes of the scale factor $\frac{4A}{\lambda P}$ under the effects of seismic deformation, temperature variation of the medium etc. Since the mechanical instrument was extremely rigid and stable, the effects of the scale factor can be avoided (Schreiber et al., 2006); 2) variations in $\dot{\mathbf{\Omega}}$ itself; 3) changes in orientation of \mathbf{n}_R when the sensor is tilted by seismic waves and as a result of the inner product, it changes the Sagnac frequency (McLeod et al., 1998; Schreiber et al., 2006). This phenomenon called tilt-ring laser coupling, tilt coupling, or tilt effects will be investigated in the following as it is a potential cause for ring-laser signals in the P coda reported by Igel et al. (2007) and Pham et al. (2009b).

To quantify the tilt - ring laser coupling, we look at equation (1.1) in detail. As mentioned by McLeod et al. (1998), $\dot{\mathbf{\Omega}}$ contains both contributions of the Earth's rotation rate and the seismically induced rotation rate. On the surface of the Earth, the seismically induced rotation rate can be expressed by three orthogonal components (vertical, north-south and east-west). Thus, (1.1) can be re-written as

$$\Delta f = \frac{4A}{\lambda P} \mathbf{n}_R \cdot (\dot{\mathbf{\Omega}}_P \mathbf{n}_P + \dot{\mathbf{\Omega}}_Z \mathbf{n}_Z + \dot{\mathbf{\Omega}}_N \mathbf{n}_N + \dot{\mathbf{\Omega}}_E \mathbf{n}_E) \quad (1.2)$$

$\dot{\mathbf{\Omega}}_P$ is rotation rate of the Earth around its rotation axis. $\dot{\mathbf{\Omega}}_Z$, $\dot{\mathbf{\Omega}}_N$, $\dot{\mathbf{\Omega}}_E$ are seismically induced rotation rates around vertical, north-south and east-west axes, respectively.

The unit basis vectors of the rotation axis of the Earth, vertical, north-south and east-west axes are \mathbf{n}_P , \mathbf{n}_Z , \mathbf{n}_N , and \mathbf{n}_E respectively.

Expanding the inner product in (1.2) we have

$$\Delta f = \frac{4A}{\lambda P} [\dot{\Omega}_P \alpha_P + \dot{\Omega}_Z \alpha_Z + \dot{\Omega}_N \alpha_N + \dot{\Omega}_E \alpha_E] \quad (1.3)$$

Here α_P , α_Z , α_N , and α_E are cosines of the angles between \mathbf{n}_R and \mathbf{n}_P , \mathbf{n}_Z , \mathbf{n}_N , \mathbf{n}_E , respectively, that can be calculated as the functions of the east-west and north-south horizontal components of seismically induced rotations Ω_E , Ω_N (or co-seismic tilts) and the latitude of the ring laser location Λ (see Appendix A).

Equation (1.3) contains the cross-axis sensitivity of a ring laser. In case $\Omega_E = 0$ and $\Omega_N = 0$ (there is no tilt), we will have $\alpha_P = \sin(\Lambda)$, $\alpha_Z = 1$, $\alpha_N = \alpha_E = 0$, and equation (1.3) simplifies to

$$\Delta f = \frac{4A}{\lambda P} [\dot{\Omega}_P \sin(\Lambda) + \dot{\Omega}_Z] \quad (1.4)$$

In several past studies (e.g. Suryanto et al., 2006, Igel et al., 2005, 2007) the co-seismic tilts Ω_E , Ω_N are assumed negligible for tele-seismic events, thus the observed vertical rotation rates were extracted from the Sagnac frequency according to equation (1.4). In general, as indicated by equation (1.3), such inferred rotation rate includes the contribution of tilt coupling. Thus, here we call it the contaminated rotation rate $\dot{\Omega}_{Z(cont.)}$ defined as

$$\dot{\Omega}_{Z(cont.)} = \Delta f \frac{\lambda P}{4A} - \dot{\Omega}_P \sin(\Lambda) \quad (1.5)$$

Combining (1.5) and (1.3) leads to

$$\dot{\Omega}_{Z(cont.)} = \dot{\Omega}_P [\alpha_P - \sin(\Lambda)] + \dot{\Omega}_Z \alpha_Z + \dot{\Omega}_N \alpha_N + \dot{\Omega}_E \alpha_E \quad (1.6)$$

In our subsequent calculations, we define tilt – ring laser coupling $\dot{\Omega}_{Tilt}$ as the difference between the contaminated rotation rate $\dot{\Omega}_{Z(cont.)}$ and purely seismically-induced rotation rate $\dot{\Omega}_Z$

$$\begin{aligned}\dot{\Omega}_{Tilt} &= \dot{\Omega}_{Z(cont.)} - \dot{\Omega}_Z \\ &= \dot{\Omega}_P [\alpha_P - \sin(\mathcal{A})] + \dot{\Omega}_Z (\alpha_Z - 1) + \dot{\Omega}_N \alpha_N + \dot{\Omega}_E \alpha_E.\end{aligned}\quad (1.7)$$

Equation (1.7) provides us with tilt-ring laser coupling to be calculated as a function of co-seismic tilts and ring laser location. We note that, to calculate exactly tilt-ring laser coupling, together with (1.7) equations (A9a,b,c,d) need to be applied. With small co-seismic tilts, instead of equations (A9a,b,c,d) equations (A10a,b,c,d) can be used and the scale factors in (1.7) are approximated as follows:

$$[\alpha_P - \sin(\mathcal{A})] \approx -\Omega_E \cos\left(\mathcal{A} - \frac{\Omega_E}{2}\right) \quad (1.8a)$$

$$(\alpha_Z - 1) \approx 0 \quad (1.8b)$$

$$\alpha_N \approx -\Omega_E \quad (1.8c)$$

$$\alpha_E \approx -\Omega_N \quad (1.8d)$$

In the following we investigate tilt-ring laser coupling for observations of local earthquakes and tele-seismic events in connection with the corresponding vertical rotation rate.

1.2.1 Observations of Local Earthquakes

In this section we investigate the tilt coupling that local earthquakes may induce. We first start with the local magnitude scale

$$M_L = \log(\mathcal{A}) - \log(\mathcal{A}_O) \quad (1.9)$$

where \mathcal{A} is the maximum trace amplitude (in millimeters) recorded on a standard short-period seismometer (Wood-Anderson instrument) and $\log(\mathcal{A}_O)$ is the calibration function and can be calculated as a function of hypocentral distance Δ (in km) for Southern California as follows (Hutton and Boore, 1987):

$$-\log(\mathcal{A}_O) = 1.110\log(\Delta/100) + 0.00189(\Delta-100) + 3.0 \quad (1.10)$$

With the magnification factor of the Wood-Anderson instrument being 2080 (see Booth, 2007), from equations (1.9) and (1.10) we can estimate the maximum displacement A_L (in meters) that an earthquake magnitude M_L may induce as

$$A_L = 10^{(M_L + \log \mathcal{A}_O - 3)} / 2080 \quad (1.11)$$

As introduced by Li et al. (2001), in a homogeneous half space the y component of the co-seismic tilt induced by plane harmonic P and SV waves with the propagation direction in the vertical (x, z) plane can be calculated from the corresponding vertical displacement D_Z by

$$\text{- P wave: } \Omega_y^P = i\omega \frac{\sin \theta_P}{\alpha} D_Z, \quad (1.12)$$

$$\text{- SV wave: } \Omega_y^{SV} = i\omega \frac{\sin \theta_{SV}}{\beta} D_Z, \quad (1.13)$$

where $\omega=2\pi/T$, T , θ_P , and θ_{SV} , respectively, are frequency, period, and incident angles of P and SV waves; α and β are P- and S- wave velocities and D_Z is the vertical displacement.

In fact, scattered SV waves generated by 3D effects may be involved randomly in the P coda. Moreover, both P and SV waves are predominant in a vertical component. Thus, the separation of P- and SV- wave types is difficult. To simplify calculations, we consider the maximum tilt to be caused by both P and SV waves. Such maximum tilt can be inferred from equations (1.12) and (1.13) by taking sines of the incident angles with maximum value being 1, wave velocities with minimum value being β :

$$\Omega_{y-max}^{P_{-}SV} = i \frac{2\pi}{T\beta} D_Z. \quad (1.14)$$

Equation (1.14) indicates that at a given period $\Omega_{y-max}^{P_{-}SV}$ reaches the maximum amplitude when D_Z reaches the maximum displacement:

$$\Omega_{y-max}^{P_{-}SV} = \frac{2\pi}{T\beta} D_{Z-max}. \quad (1.15)$$

Assuming that the maximum displacement extracted from local magnitude scale is a representative for vertical displacement (e.g., of SV) and let $T = 0.8$ s (period of the Wood-Anderson instrument), from (1.11) and (1.15) we can estimate the maximum tilt (in radian) induced by a local earthquake of magnitude M_L as follows:

$$\Omega_{y-max}^{M_L} = \frac{\pi}{832\beta} 10^{(M_L + \log A_0 - 3)}. \quad (1.16)$$

Equation (1.16) provides us with the maximum transverse tilt to be expected in the domain of local magnitude and distance range. Using this equation, maximum co-seismic tilts on bed rock site ($\beta = 3200$ m/s) and on soft sediment site ($\beta = 500$ m/s) are calculated for the applicable range of local magnitude. The results are presented in Figures 1.1 and 1.3 (left axes). We can see that in the applicable range of local magnitudes ($M_L < 7$) and distance ($10\text{km} \leq \Delta \leq 600$ km) for both types of ground condition (sediment and bed rock) the maximum tilt motion is about 10^{-3} rad. This implies that the use of approximations (A1-10a,b,c,d) and (1.8) in this section is well accepted and (1.7) can be rewritten as

$$\dot{\Omega}_{Tilt} \approx -\Omega_E \dot{\Omega}_P \cos\left(\Lambda - \frac{\Omega_E}{2}\right) - \Omega_E \dot{\Omega}_N - \Omega_N \dot{\Omega}_E. \quad (1.17)$$

In theory, P and SV waves coming with a back azimuth φ cause no tilt motion for the radial component. Thus, with the maximum transverse tilt provided by (1.16) we can calculate the corresponding north-south and east-west components of tilts as follows (see Appendix B):

$$\Omega_N = -\Omega_{y-max}^{M_L} \sin(\varphi), \quad (1.18)$$

$$\Omega_E = \Omega_{y-max}^{M_L} \cos(\varphi). \quad (1.19)$$

The corresponding components of maximum tilt rates (in rad/s) can be estimated using plane wave assumption

$$\dot{\Omega}_N = \frac{2\pi}{T} \Omega_N = -\frac{2\pi}{T} \Omega_{y-max}^{M_L} \sin(\varphi), \quad (1.20)$$

$$\dot{\Omega}_E = \frac{2\pi}{T} \Omega_E = \frac{2\pi}{T} \Omega_{y-max}^{M_L} \cos(\varphi). \quad (1.21)$$

Combining (1.16), (1.17), (1.18), (1.19), (1.20), and (1.21), we obtain the maximum tilt coupling $\dot{\Omega}_{Tilt}^{max}$ (in rad/s) as a function of local magnitude and distance as follows:

$$\dot{\Omega}_{Tilt}^{max} = \dot{\Omega}_P \frac{\pi}{832\beta} 10^{(M_L + \log A_0 - 3)} + \frac{\pi^3}{276889.6\beta^2} 10^{2(M_L + \log A_0 - 3)}. \quad (1.22)$$

We note that factors $\left[-\cos\left(\Delta - \frac{\Omega_E}{2}\right)\cos(\varphi) \right]$ of the first term and $\sin(\varphi)\cos(\varphi) = \frac{\sin(2\varphi)}{2}$ of the second term in the right hand side of equation (1.22) were separately replaced by their maximum values being 1 and 0.5 respectively, and $T = 0.8s$.

We estimate the maximum value of the corresponding vertical rotation rate to compare with the above tilt coupling. Assuming that A_L is representative of SH-wave amplitudes, the corresponding peak rotation rate (in rad/s) can be estimated by using the relationship between displacement and rotation rate (see Igel et al., 2007):

$$\dot{\Omega}_Z = 2 \frac{\pi^2}{\beta T^2} A_L = \frac{\pi^2}{665.6\beta} 10^{(M_L + \log A_0 - 3)}. \quad (1.23)$$

Equations (1.22), and (1.23), respectively, provide us with maximum tilt-ring laser coupling and vertical rotation rate to be expected in the domain of local magnitude and distance range. We use these equations to investigate the expected values for two cases: bed rock with $\beta = 3200$ m/s and soft sediment with $\beta = 500$ m/s. The results are presented in Figures 1.1, 1.2 (for bed rock) and 1.3, 1.4 (for soft sediment).

The figures show the maximum values to be expected as a function of distance for different magnitudes (left) and as a function of magnitude for different distances (right). We can see that in the applicable range of local magnitudes ($M_L < 7$) and distance ($10km \leq \Delta \leq 600$ km) for both types of ground condition (sediment and bed rock), at the same distance the increase one unit of magnitude leads to the enlargement of about one order of amplitude of tilt and rotation rate. The same tendency is shown for tilt-ring laser coupling at large distance with small magnitude (weak motions). However, at the same distance close to source with large magnitude (strong motions) the raise of one unit of magnitude results in the increase of about two orders of amplitude of tilt-ring laser coupling. The maximum tilt-ring laser coupling predicted for sediment site is two orders of magnitude bigger than corresponding one on the bed rock. Nevertheless, maximum tilt-ring laser coupling predicted for both sites (Figures 1.2 and 1.4) is

at least two orders of magnitude smaller than the corresponding maximum rotation rate (right axes of Figures 1.1 and 1.3) and therefore can be neglected.

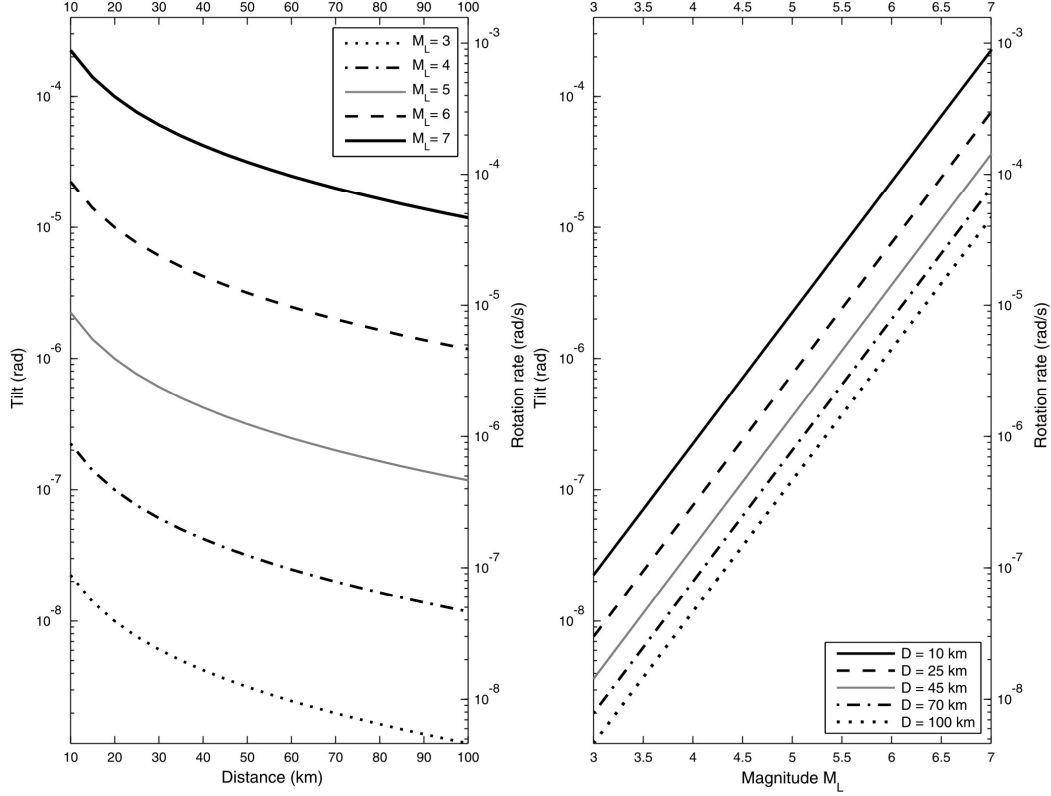


Figure 1.1. Maximum tilt (left axes) and vertical rotation rate (right axes) are predicted for a dominant period $T = 0.8$ s on the bed rock ($\beta = 3200$ m/s) as a function of local magnitude and hypocentral distance.

We note that for strong motions at near source, $\dot{\Omega}_Z$, $\dot{\Omega}_N$, and $\dot{\Omega}_E$ may reach amplitudes on the order of 10^{-2} rad/s (Nigbor, 1994) or greater. This implies that they are much more significant than $\dot{\Omega}_p$ with magnitude order of 10^{-5} rad/s. As a consequence, contribution of the first term in equation (1.7) can be ignored and the ring laser location virtually has no effect. In this case, both horizontal components of seismically induced rotations play the same role on affecting ring laser measurements. At this point it should be noted that ring laser technology is unlikely to play a major role for near source observations. Nevertheless other technologies (e.g. fiber-optic approaches) need to be investigated for cross-axis sensitivity in a similar way.

1.2.2 Observations of Tele-Seismic Events

For tele-seismic events $\dot{\Omega}_P$ are much more significant than $\dot{\Omega}_Z$, $\dot{\Omega}_N$, and $\dot{\Omega}_E$ (order of 10^{-8} rad/s for large earthquakes - see Igel et al., 2007; Pham et al., 2009b). In this case, with scale factors mentioned through equations (1.8), the significant part of tilt - ring laser coupling comes from the first term in (1.7). Thus,

$$\dot{\Omega}_{Tilt} = -\dot{\Omega}_P \Omega_E \cos\left(\lambda - \frac{\Omega_E}{2}\right). \quad (1.24)$$

Equation (1.24) implies that for observations of tele-seismic events, the tilt coupling depends on the location of the ring laser and Ω_E only. With the same tilt motion, the tilt coupling reaches a maximum when $\lambda = \Omega_E / 2$ (ring laser is almost at the equator) and minimum when $\lambda = 90$ deg (ring laser at the pole).

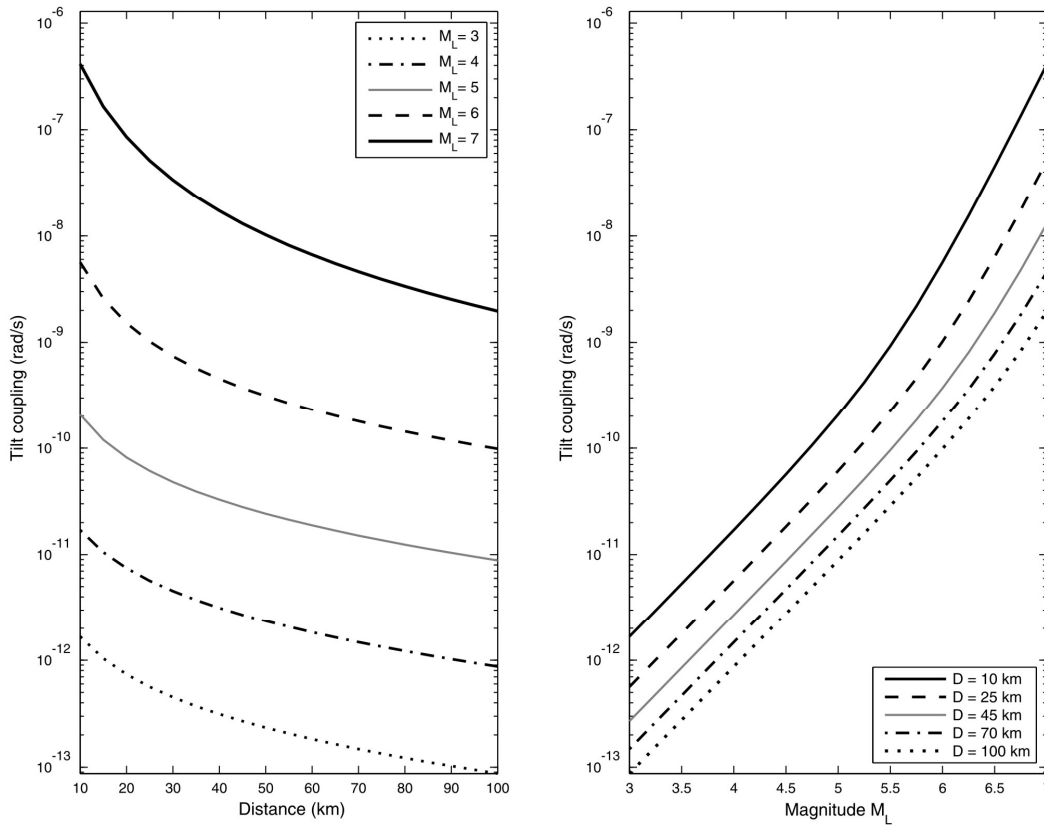


Figure 1.2. Maximum tilt-ring laser coupling is predicted for a dominant period $T = 0.8$ s on the bed rock ($\beta = 3200$ m/s) as a function of local magnitude and hypocentral distance.

We use (1.24) to investigate the variations of maximum tilt coupling that tele-seismic events may induce. We start with the International Association of Seismology and Physics of the Earth's Interior (IASPEI) formula of the surface wave magnitude,

$$M_S = \log (A_S/T) + 1.66 \log D + 3.3, \quad (1.25)$$

where A_S is the peak ground amplitude (in micrometers) of the surface (Rayleigh) wave in the vertical component within the period range $18\text{s} \leq T \leq 22\text{s}$, and D is epicentral distance (in degree) in the range $20^\circ \leq D \leq 160^\circ$.

From (1.25), Rayleigh waves of an earthquake magnitude M_S are expected to induce a maximum vertical displacement (in meters):

$$A_S = T \cdot 10^{(M_S - 1.66 \log D - 9.3)}. \quad (1.26)$$

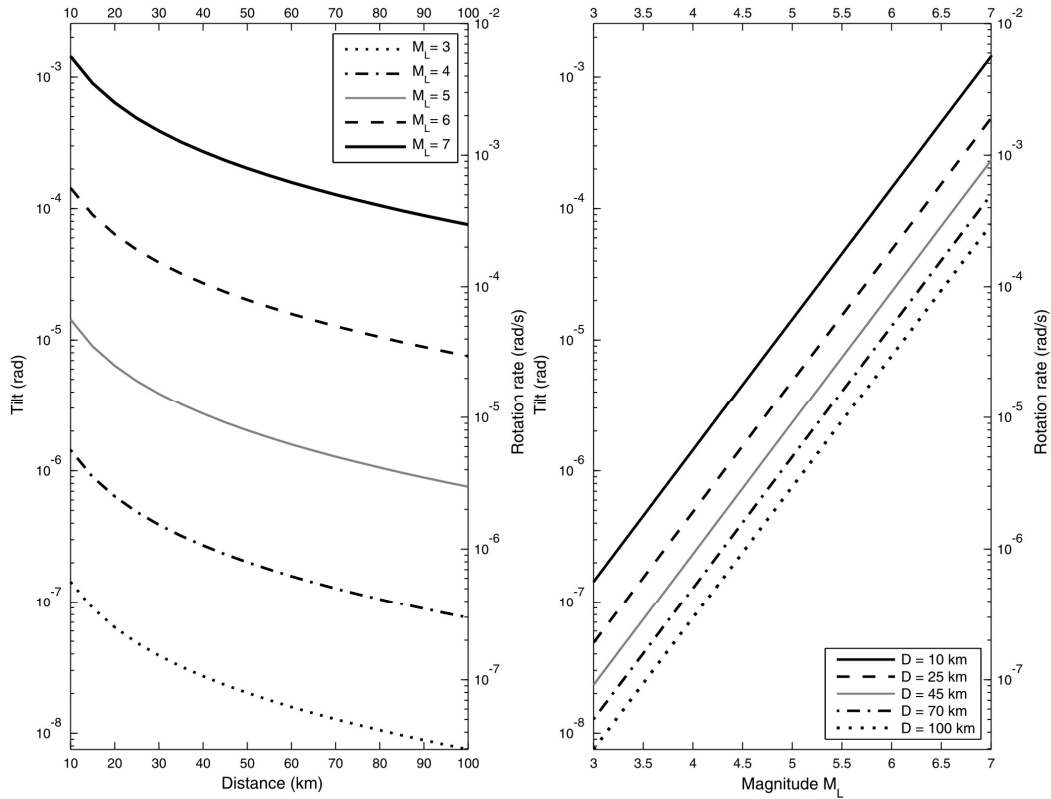


Figure 1.3. Maximum tilt (left axes) and vertical rotation rate (right axes) are predicted for a dominant period $T = 0.8\text{s}$ on the soft sediment ($\beta = 500\text{ m/s}$) as a function of local magnitude and hypocentral distance.

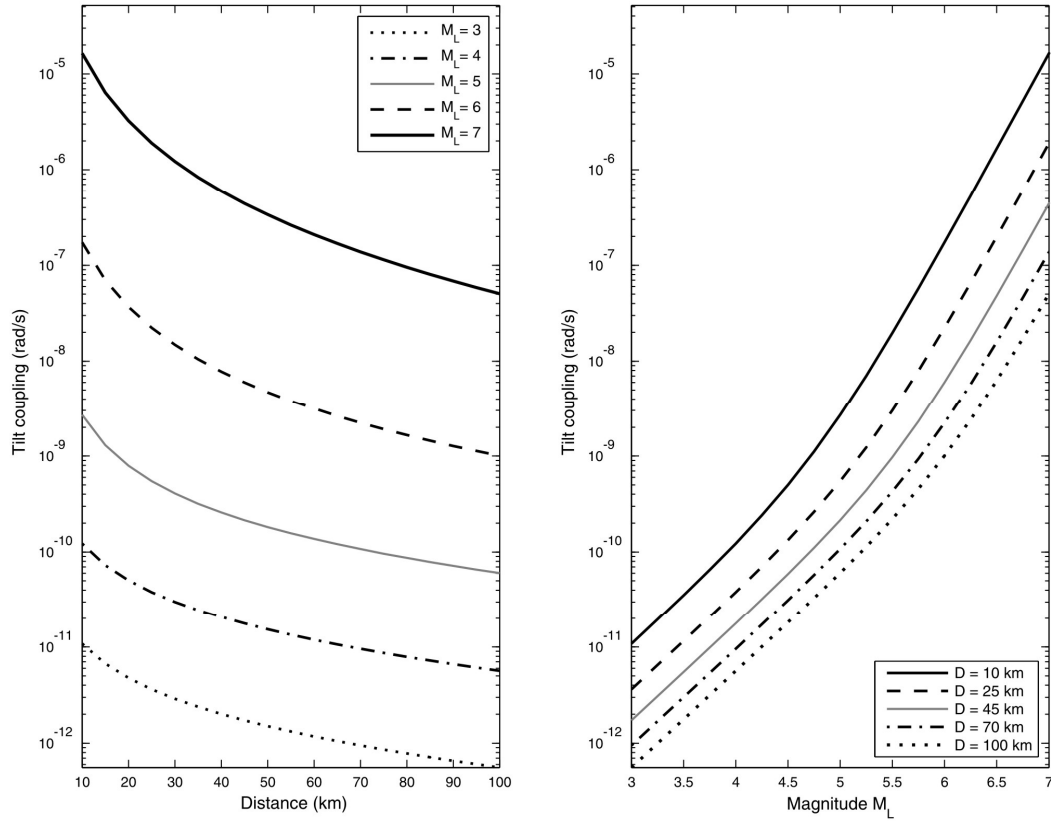


Figure 1.4. Maximum tilt-ring laser coupling is predicted for a dominant period $T = 0.8$ s on the soft sediment ($\beta = 500$ m/s) as a function of local magnitude and hypocentral distance.

According to Li et al. (2002), the co-seismic tilt induced by a Rayleigh wave in a homogeneous half space can be calculated from its vertical displacement D_Z by

$$\Omega_y^R = i \frac{\omega}{V_R} D_Z, \quad (1.27)$$

where $\omega = 2\pi/T$ and V_R are frequency and Rayleigh wave phase velocity, respectively.

Equation (1.27) indicates that with a certain value of the phase velocity at a given period, Ω_y^R reaches the peak value when D_Z reaches a peak displacement A_S ,

$$\Omega_{y-\max}^R = \frac{2\pi}{TV_R} A_S. \quad (1.28)$$

Combining (1.26) and (1.28), the maximum tilt (in radian) induced by an earthquake magnitude M_S , thus, is

$$\Omega_{y-\max}^R = \frac{2\pi}{V_R} 10^{(M_S - 1.66 \log D - 9.3)} \quad (1.29)$$

This $\Omega_{y-\max}^R$ will cause maximum tilt coupling $\dot{\Omega}_{Tilt-\max}^R$ (in rad/s) if it plays the role of Ω_E in equation (1.24) and $\left[-\cos\left(A - \frac{\Omega_E}{2} \right) \right]$ obtains its maximum value being 1,

$$\dot{\Omega}_{Tilt-\max}^R = \dot{\Omega}_P \frac{2\pi}{V_R} 10^{(M_S - 1.66 \log D - 9.3)}. \quad (1.30)$$

Equations (1.29) and (1.30) provide us with the maximum tilt and tilt coupling to be expected in the domain of applicable surface wave magnitude and distance range. Taking $V_R = 3100$ m/s for a dominant period of $T = 20$ s, such expected maximum values are calculated and presented in Figure 1.5. The figure shows the maximum values to be expected as a function of distance for different magnitudes (left-hand panel) and as a function of magnitude for different distances (right-hand panel). The left-hand axes denote the expected tilt in radian and right-hand axes denote the expected tilt coupling in rad/s. Compared to the corresponding predicted rotation rate shown in Igel et al. (2007) the expected tilt coupling is three orders of magnitude smaller and can be ignored.

1.3 Tilt - Ring Laser Coupling: Observations in the P Coda

As reported by Igel et al. (2007) and Pham et al. (2009b), there are significant high frequency motions of vertical component of rotations in the P coda of tele-seismic signals. This type of signals is either directly visible or can be inferred through the investigation of cross-correlation between transverse acceleration and vertical rotation rate. A typical example for this phenomenon is shown in Figure 1.6 for the Tokachi-oki event 25/9/2003 M8.1 (see Pham et al., 2009b for more details). Theoretically, in spherically symmetric isotropic media we should not observe a vertical component of rotation before the onset of SH waves. One of possible explanations for the observed P coda rotations is tilt-ring laser coupling. These observations were part of the motivation for the present study aiming at the

first quantitative estimates of tilt-ring laser coupling in connection with tele-seismic observations. In this section we focus on investigating the effects of tilt-ring laser coupling in the observed P coda. The aim is to give a quantitative answer to the question, whether tilt-ring laser coupling contributes to the rotational motions observed in the P coda. The magnitude-amplitude relations previously used in the general case do not apply in this case which is why we estimate the tilt-coupling effects directly from the data.

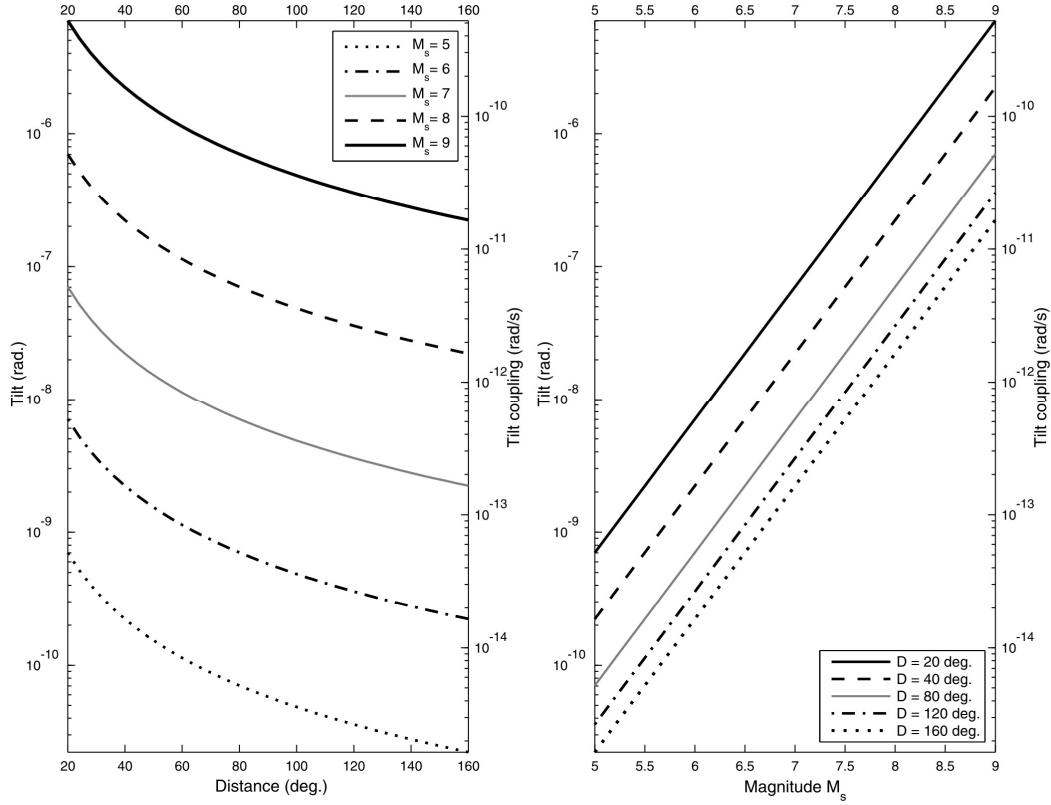


Figure 1.5. Expected maximum tilt (left axes) and tilt-ring laser coupling (right axes) induced by tele-seismic Rayleigh waves as a function of surface wave magnitude and distance. Phase velocity is assumed $V_R = 3100$ m/s.

As shown in the previous section, the calculation of tilt-ring laser coupling requires knowledge of the horizontal components of seismically induced rotations (or tilts). However, tiltmeters - sensors measuring horizontal components of rotational motions at the Earth's surface - are sensitive to translation motions, and therefore do not provide the correct tilt signals in the required frequency band (Suryanto, 2006). Here we investigate the effects of tilt-ring laser coupling in the observed P coda based on translation derived tilts (see Li et al., 2001).

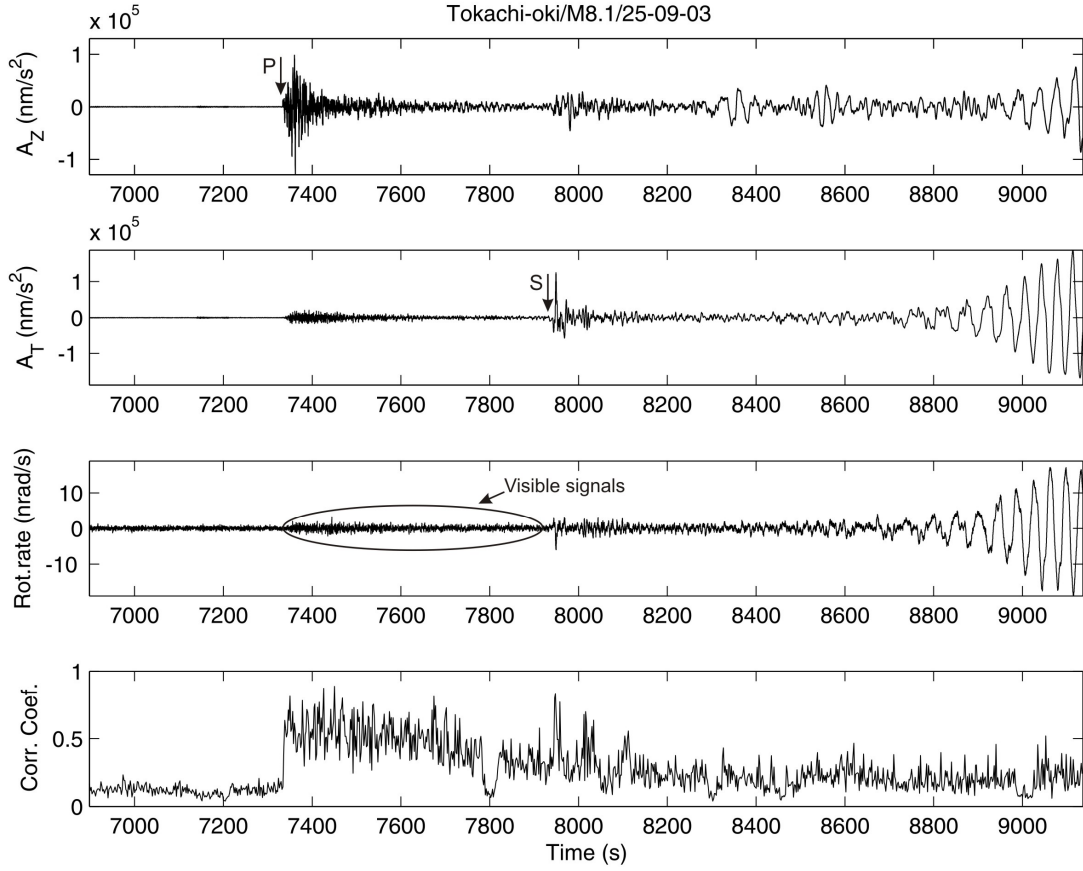


Figure 1.6. Observations of the Tokachi-oki event 25-09-2003, M8.1 at the Wettzell station. Top three traces: vertical acceleration, transverse acceleration and rotation rate, respectively. Bottom: zero lag normalized cross correlation coefficients between rotation rate and transverse acceleration after high-pass filtering with cut-off period 1s, calculated for 2s sliding time windows. The figure shows significant rotational motions in the P coda.

We apply equation (1.14) to derive maximum co-seismic tilt in the P coda from observed translations and use it to quantify the corresponding tilt-ring laser coupling. It should be noted that Li's equations are developed under the assumption of harmonic plane waves (Li et al., 2001) and a homogeneous half space. Thus, to derive tilt signal we first convert the time series of displacements to harmonic discrete frequencies by Fourier transformation. We use equation (1.14) to define the Fourier spectra of the transverse tilt at discrete frequencies as a function of the Fourier spectra of the displacement. The time history of the transverse tilt finally can be obtained by inverse Fourier transformation.

As mentioned by Trifunac et al. (2001), Graizer (2005, 2006) and Pillet et al. (2007) standard measurements of translations are contaminated by co-seismic

rotations. Fortunately, this type of contamination is negligible at high frequencies for far field observations. Thus, at high frequencies considered in this study the observed translations are applicable to derive tilt motions.

The observed seismograms of the Tokachi-oki 25-09-2003 M8.1 earthquake are used to investigate tilt-ring laser coupling in the P coda (see Data and Resources Section). The vertical component of the observed velocities of the event is high pass filtered with cut-off period 150s then integrated to obtain displacement. This signal is used to derive the corresponding maximum tilt motion. The translation derived tilt is then applied in the role of the Ω_E in equation (1.24) to estimate the corresponding tilt-ring laser coupling. The result is presented in Figure 1.7 (third trace from top). It is three orders of magnitude smaller than the corresponding rotation rate measured by the ring laser sensor; thus, the tilt coupling in the P coda of the event is insignificant. In addition, after subtracting this estimated tilt coupling, the P coda rotations are still visible (Figure 1.7, fourth trace from top). We calculate zero lag normalized cross correlation coefficients between the transversal acceleration and the corrected P coda rotations for a 2s sliding window after high-pass filtering both signals with cut off period 1s. The results show a pronounced increases right after the P-wave onset (Figure 1.7, bottom). All these results indicate that for the observations of the Tokachi-oki 25-09-2003 M8.1 event the tilt-ring laser coupling is insignificant and can be ignored.

We finally use the available database of events observed by both the broad-band-seismometer and the ring laser sensor at Wettzell station (see Data and Resources Section) to examine systematically maximum tilt-ring laser coupling in the P coda by comparing it with corresponding observed peak rotation rate. Events of Algeria 21-05-2003 M6.9, Tokachi-oki 25-09-2003 M8.1, Russia 27-09-2003 M7.5, and Sumatra 12-09-2007 M8.4 were chosen for this study because they are distributed in different ranges of magnitude, distance, and back azimuth and their P-coda rotations are clearly visible (see Pham et al., 2009b). Because the observed P-coda rotations are predominant around a period of 1s (Pham et al., 2009b), the vertical displacements and the observed rotation rates of these events are filtered in a narrow band with central period 0.5s, 1s, and 2s, then peak values were extracted. We use equation (1.15) to calculate maximum co-seismic tilt, and then use it as Ω_E in equation (1.24) to calculate the maximum tilt-ring laser coupling in the P coda. The results are presented in Table 1.1. We can recognize that for all considered events and periods the predicted tilt-ring laser coupling is four orders of magnitude smaller than observed peak rotation rate. We conclude that tilt-ring laser coupling in the P coda is negligible and the main causes for the observed P-coda rotations thus should come from 3D effects (e.g. P-SH scattering, as suggested by Pham et al., 2009b).

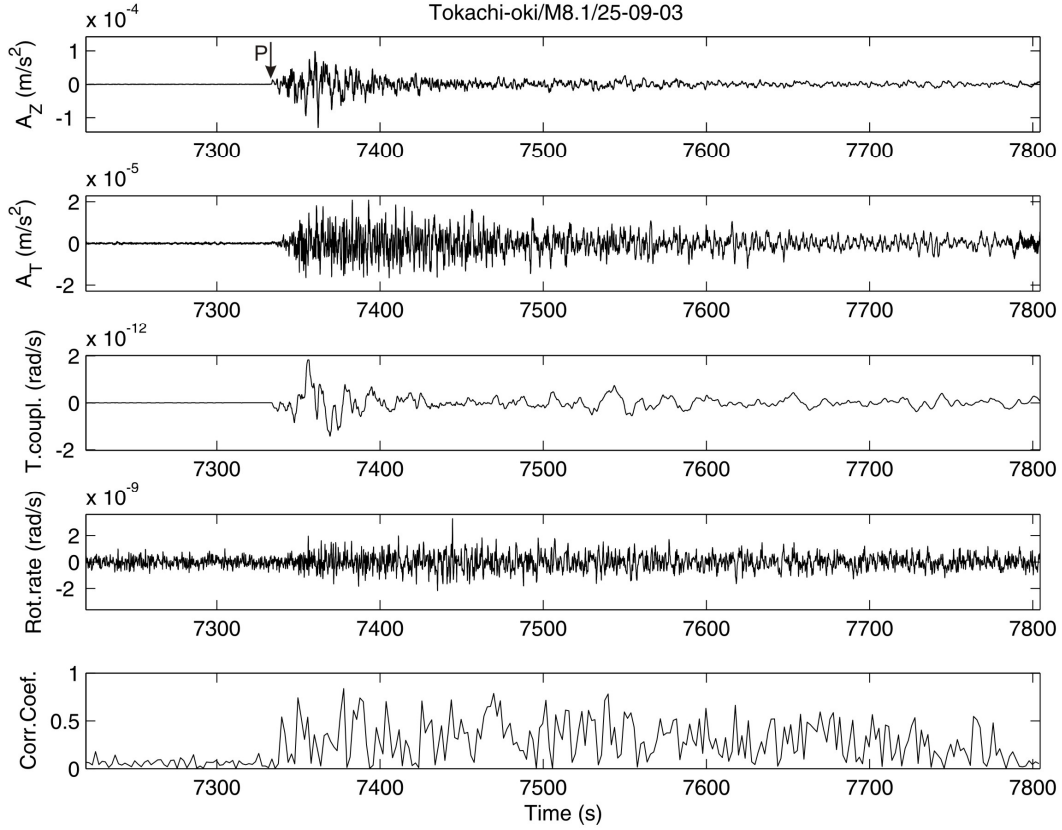


Figure 1.7. Seismic signals in the P coda of the Tokachi-oki event 25-09-2003, M8.1. Two top traces: vertical (A_Z) and transverse (A_T) components of accelerations; The third trace from top: the maximum tilt-ring laser coupling derived from translation; The fourth trace from top: observed rotation rate after subtracting the maximum tilt-ring laser coupling; Bottom: variations of the correlation coefficients between the corrected rotation rate and transverse acceleration.

1.4 Discussion and Conclusions

Previously, several authors reported about effects of co-seismic tilts on ring laser measurements (e.g. McLeod et al., 1998; Schreiber et al., 2005, 2006). However, these studies did not fully quantify the effects and discuss the relevance for broad band ring laser data processing. The main goal of this study is to fill this gap and investigate quantitatively the effects of co-seismic tilts on ring laser measurements.

In this chapter, we present equations of cross-axis sensitivity for ring laser sensors. To calculate tilt-ring laser coupling requires knowledge of horizontal components of seismically induced rotations (or tilts). Nevertheless, measurements of co-seismic tilt using tiltmeters provide incorrect signals in the

frequency band of interest because of the sensitivity of tiltmeters to horizontal accelerations (e.g., Suryanto 2006). We perform estimates of maximum tilt-ring laser coupling based on magnitude-amplitude relations to be expected for observations of local earthquakes and tele-seismic events. The results show negligible tilt coupling for all the applicable range of the surface wave magnitude and local magnitude scales.

Table 1.1

Observations and Maximum Tilt and Tilt Coupling at Different Dominant Periods in the P Coda of the Typical Events

Event	Observed Peak Dz (nm)			Observed Peak $\dot{\Omega}_Z$ (nrad/s)			Maximum Tilt (nrad)			Maximum Tilt Coupling (10^{-5} nrad/s)		
	0.5 (s)	1 (s)	2 (s)	0.5 (s)	1 (s)	2 (s)	0.5 (s)	1 (s)	2 (s)	0.5 (s)	1 (s)	2 (s)
Algeria 21 May 2003, M6.9	84.40	329.31	631.52	0.14	0.30	0.11	0.31	0.61	0.58	1.50	2.94	2.81
Tokachi- oki 25 Sep., 2003, M8.1	199.52	355.78	1235.37	0.52	0.63	0.44	0.73	0.66	1.14	3.56	3.17	5.51
Russia 27 Sep., 2003, M7.5	73.40	366.53	638.02	0.40	0.46	0.37	0.27	0.68	0.59	1.31	3.27	2.84
Sumatra 12 Sep., 2007, M8.4	75.74	309.34	1353.02	0.07	0.30	0.51	0.28	0.57	1.25	1.35	2.76	6.03

Because ring laser technology is unlikely to play a major role for near source observations and the appearance of the ring laser rotational signals in the P coda of the tele-seismic events (Igel et al., 2007, Pham et al., 2009b) needs to be explained, our investigations on data-based tilt-ring laser coupling focus on the P coda observations. Translation derived tilt (Li et al., 2001) is applied to observed translations to estimate the maximum tilt-ring laser coupling for P coda at high frequencies. The results obtained again show that the tilt-ring laser coupling can be neglected.

In summary, it can be concluded that tilt-ring laser coupling is negligible compared to the corresponding vertical rotation rate not only for observations of tele-seismic events but also for all the applicable range of the local magnitude scale.

Chapter 2

Observations and Modeling of Rotational Signals in the P Coda: Constraints on Crustal Scattering^{*}

Abstract

In addition to three classical components (vertical, north-south, and east-west) of ground translations recorded by broadband seismometer, a component of earthquake induced rotational ground motions around the vertical axis is consistently measured by a ring laser sensor located in Wettzell, southeast Germany. Significant rotations around the vertical axis in the P coda of tele-seismic signals are either directly visible or can be inferred through the investigation of cross-correlation between transverse component (the component that perpendicular to the great circle connecting the earthquake and seismometer) of translation acceleration and ring laser rotation rate. Theoretically, in spherically symmetric isotropic media we should not observe rotational signals around the vertical axis before the onset of SH waves. Possible causes for the observed rotations in the P coda are: (1) tilt – ring laser coupling; (2) anisotropy; (3) topographic scattering; and (4) P-SH scattering in the crust. Here we show that P-SH scattering in the 3D random crust can explain the observations and allow us to constrain crustal scattering properties.

^{*} Except the section *Topographic Scattering*, the other contents of this chapter have been published in Pham D.N., H. Igel, J. Wassermann, M. Käser, J. de la Puente, U. Schreiber, 2009b, Observations and Modelling of Rotational Signals in the P-Coda: Constraints on Crustal Scattering, *Bull. Seismol. Soc. Am.*, 99, no. 2B, 1315-1332, doi: 10.1785/0120080101.

2.1 Introduction

In seismology, observations are traditionally based on measurements of inertial seismometers that record three components (vertical, north-south, and east-west) of earthquake induced ground translations (displacement, velocity, or acceleration). There are theoretical studies suggesting that in addition to translations, rotational ground motions should be measured (e.g., Aki and Richards, 2002). This type of observation might be relevant for: (1) correcting translation signals recorded by classical seismometers for contamination by ground rotation (Graizer, 2005; Graizer, 2006; Pillet and Virieux, 2007); (2) extracting additional information on earthquake source properties (e.g., Takeo and Ito, 1997; Takeo, 1998), soil - structure – interactions (Trifunac and Todorovska, 2001), and properties of the subsurface (Igel et al., 2007; Fichtner and Igel, 2008); (3) providing additional ground motion information to earthquake engineers for seismic design (e.g., Li et al., 2001, 2002). However, the lack of instrumental resolution did not allow seismologists to record this kind of motions in a consistent way until recently (Pancha et al., 2000; Schreiber et al., 2005; Cochard et al., 2006; Igel et al., 2005, 2007).

Ring laser technology has provided the means to allow in principle observation of rotational motions in a wide frequency band and epicentral distance range (Schreiber et al., 2005; Igel et al., 2005, 2007). The remarkable consistency between rotational ground motions around the vertical axis recorded by a ring laser and transverse component (the component that perpendicular to the great circle connecting the earthquake and seismometer) of translation acceleration (called shortly transverse acceleration) for periods of 1s up to 150s and suitable values of the phase velocities estimated by taking the ratio of transverse acceleration and vertical rotation rate are not only proving the appropriateness of the ring laser sensor but also imply that the multi-component observations allow the estimation of wave field properties (e.g. phase velocities, propagation direction) that otherwise are only accessible with high accuracy through array measurements (Igel et al., 2007).

In a previous study (Igel et al., 2007), a significant rotational motion component around the vertical axis in the P coda of seismic signals had been recognized. At first, this is a surprising observation because, theoretically, in spherically symmetric isotropic media P and SV waves do not generate rotations around the vertical axis so we should not observe this kind of motions before the arrival times of SH waves. There are several possible explanations for the phenomenon of P coda rotations: (1) tilt – ring laser coupling: when P waves arrive they do generate tilts at the Earth's surface (i.e. rotational motions around horizontal axes). This

will contaminate the ring laser measurements through changes of the surface normal with respect to the Earth's rotation axis and may potentially contribute to the phenomenon of rotation in the P coda (Schreiber et al., 2005; Igel et al., 2007); (2) P-SH scattering in the crust; (3) topographic scattering; and (4) anisotropy. The tilt – ring laser coupling is demonstrated to be negligible in the far field case in previous chapter (also in Pham et al., 2009a). The contributions of anisotropy on the P coda rotations will be the subject of the next chapter. Here, we focus on investigating the effects of P-SH scattering in the crust as well as of topographic scattering on rotational ground motions around the vertical axis.

The main goals of this study are to present the observations of rotational motions around the vertical axis in the P coda, and to model these observations with three-dimensional-wave propagation under the assumption of scattering.

2.2 Observations

2.2.1 Database

The data used in this study includes collocated records of both the G - ring laser sensor and broadband seismometer (STS-2) at the Fundamental station, Wettzell, south-east Germany (see Data and Resources Section). The G - ring laser sensor is located in a purpose-built observatory and installed on an special material (to avoid effects of temperature, pressure or deformation) and records rotational ground motions around a vertical axis. About 300 m away from this instrument, a STS-2 broadband sensor (WET station, latitude 49.15° , longitude 12.88° , German Regional Seismic Network) records permanently three orthogonal components of ground velocity. Further details on the instruments and the measurement principle can be found in (Schreiber et al., 2006; Igel et al., 2007).

Observations of 36 earthquakes that occurred between May 2003 and February 2008 are used in this study. The epicentral distance and magnitude distributions of the observed events are shown in Figure 2.1 with event information summarized in Table 2.1. Each event in this database includes four components recorded by the aforementioned instruments: three traditional components of ground velocity and one vertical component of ground rotation rate. Transverse acceleration, another component usually used in this study, is inferred by rotating (in a local radial-transverse system) the time-differentiated components of the observed horizontal ground velocities.

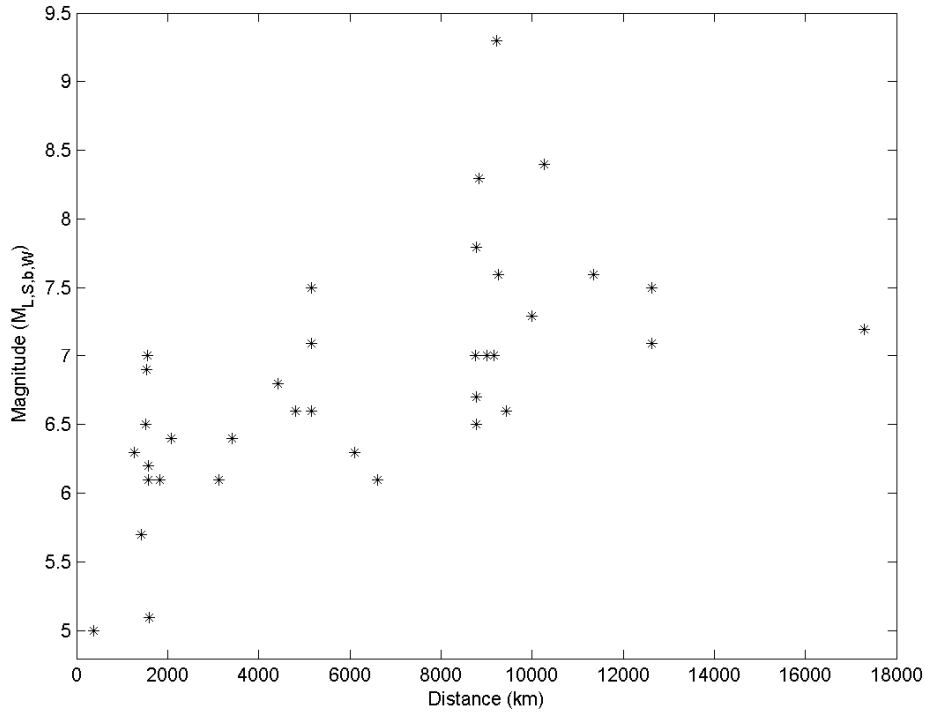


Figure 2.1. Magnitude distribution of the observed events as a function of epicenter distance.

In the following we investigate the observed P-coda rotations systematically by examining their energy variations as a function of frequency, incoming direction, and time. The frequency and directional dependence of the P-coda rotations is revealed using the zero-phase butterworth first-order filtering and cross-correlation techniques. Normalized envelopes are used to investigate time-dependent variations of energy in the P-coda rotations.

2.2.2 Frequency Dependence of Direct Observations

Analysis of the observed data showed that the rotational signals around the vertical axis are visible in the P-coda sections of strong (or near) earthquakes. A typical example for these direct observations is the case of the 12 September 2007 M8.4 Sumatra earthquake. To examine the frequency dependence of the P coda rotations, we low-pass filter the signals with different cutoff periods. Results are shown in Figure 2.2. We observe that with increasing cutoff period, the amplitude of the P-coda rotations is decreased. Amplitudes of the P-coda rotational signals decrease significantly for a cutoff period $T=5s$ and almost disappear when the cutoff period reaches a value of 10s. This implies that the energy of the observed

P-coda rotations is predominant at high frequencies. This phenomenon is observed for all events with visible P-coda rotations.

Table 2.1
Earthquakes Used in This Study

Date (yy, mm, dd)	Mag. (L,b,S, W)	Lat. (deg.)	Long. (deg.)	Depth (km)	Region	Distance (km)	Baz (deg.)	Note for rot. rate in the P coda
03/05/21	6.9	36.96	3.63	12	Algeria	1547.2	212.3	Visible
03/05/26	7.0	38.85	141.57	68	Honshu	9009.2	38.0	Visible
03/07/06	5.7	40.44	26.02	17	Turkey	1415.1	128.2	Invisible
03/08/14	6.3	39.16	20.60	10	Greece	1268.6	148.2	Visible
03/09/25	8.1	41.80	143.91	27	Tokachi-oki	8828.0	34.9	Visible
03/09/27	7.5	50.04	87.81	16	Russia	5164.8	58.8	Visible
03/09/27	6.6	50.09	87.76	10	Russia	5158.9	58.8	Invisible
03/10/01	7.1	50.21	87.72	10	Siberia	5149.9	58.7	Invisible
03/10/08	6.7	42.65	144.57	32	Hokkaido	8773.3	34.0	Invisible
03/10/31	7.0	37.81	142.62	10	Honshu	9155.4	37.8	Invisible
03/11/17	7.8	51.15	178.65	33	Rat Islands	8780.6	9.0	Invisible
03/12/26	6.8	29.00	58.31	10	Iran	4426.5	103.3	Invisible
04/02/05	7.1	-3.62	135.54	16	Irian-Jaya	12629.5	66.5	Invisible
04/02/07	7.5	-4.00	135.02	10	Irian-Jaya	12628.5	67.2	Invisible
04/02/24	6.3	35.20	-4.00	0	Al Hoceima	2074.0	227.9	Invisible
04/03/17	6.1	34.59	23.33	24	Greece	1831.7	148.2	Invisible
04/04/05	6.6	36.51	71.03	187	Afghanistan	4817.6	84.3	Invisible
04/05/28	6.4	36.29	51.61	17	Iran	3424.5	100.0	Invisible
04/05/29	6.6	34.25	141.41	16	Honshu	9440.2	40.5	Invisible
04/12/05	5.0	48.12	8.08	10	Germany	370.8	253.8	Visible
04/12/26	9.3	3.30	95.98	30	Sumatra	9228.4	93.1	Visible
07/09/12	8.4	-4.44	101.37	34	Sumatra	10271.0	94.0	Visible
07/10/31	6.5	51.37	-178.38	28	Mariana Isl.	8787.0	352.9	Visible
07/11/14	7.6	-22.23	-69.91	40	North Chile	11356.0	249.9	Visible
07/12/09	7.2	-26.06	-177.52	190	South Fiji	17296.0	336.9	Visible
07/12/19	7.0	51.50	-179.50	60	Alentia	8763.0	352.2	Invisible
08/01/06	6.5	37.40	22.70	70	South Greece	1526.0	145.2	Visible
08/01/09	6.3	32.70	85.20	50	Xizang	6098.6	78.7	Invisible
08/02/08	6.1	11.00	-42.70	10	Atlantic	6617.8	250.0	Visible
08/02/14	7.0	36.60	21.70	30	Greece	1566.7	149.6	Visible
08/02/14	6.1	36.50	21.90	33	Greece	1584.2	149.2	Visible

Table 2.1 (*continued*)
Earthquakes Used in This Study

Date (yy, mm, dd)	Mag. (L,b,S, W)	Lat. (deg.)	Long. (deg.)	Depth (km)	Region	Distance (km)	Baz (deg.)	Note for rot. rate in the P coda
08/02/19	5.1	36.40	21.80	40	Greece	1590.6	149.7	Invisible
08/02/20	7.6	2.90	96.00	33	Sumatra	9263.6	93.3	Invisible
08/02/20	6.2	36.50	21.70	25	Greece	1576.8	149.8	Visible
08/02/21	6.1	77.10	18.40	10	Svalbard	3117.7	2.6	Invisible
08/02/25	7.3	-2.50	99.90	33	Sumatra	10001.0	93.9	Invisible

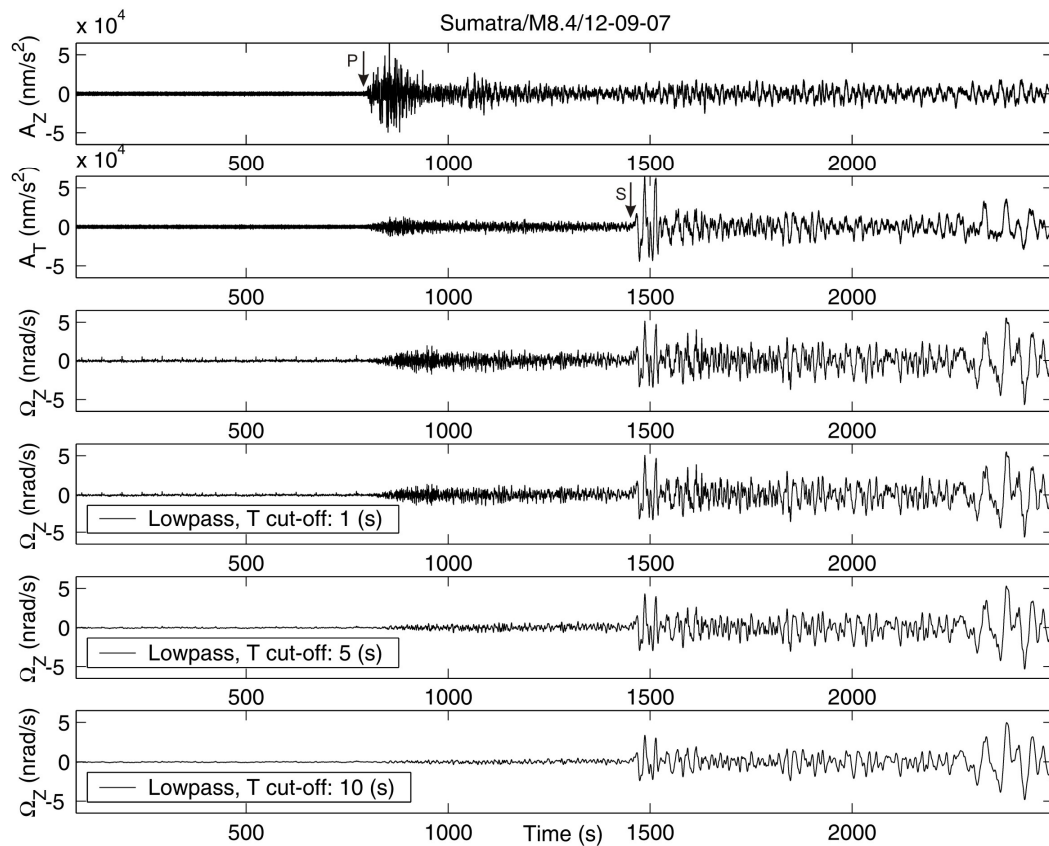


Figure 2.2. Observations of translation and rotational ground motions induced by the 12 September 2007 M8.4 Sumatra earthquake. Top three traces: Unfiltered vertical and transverse components of ground acceleration and rotation rate, respectively. Bottom three traces: low-pass filtered rotation rate with cutoff periods 1s, 5s, and 10s, respectively. Significant energy of rotational motions in the P coda is visible and predominant at high frequencies.

2.2.3 Increase in Correlation Right After the Onset of P Wave

As indicated in Table 2.1, in many cases rotational energy in the P coda is hidden in the noise. An example is shown in Figure 2.3. The 24 February 2004 M6.4 Al Hoceima event does not show visible P-coda rotations (Figure 2.3, the third trace from top). To investigate the variation of rotation rate in such events, we use the cross-correlation technique. Theoretically, assuming plane shear-wave propagation in horizontal direction with transverse polarization, vertical rotation rate and transverse acceleration should have the same waveform and their amplitudes should scale proportionally to two times the phase velocity (Igel et al., 2005 ; Cochard et al., 2006; Igel et al., 2007). In the P-coda time window, with clear visibility of transverse acceleration, an increase of correlation between rotation rate and transverse acceleration would therefore indicate the presence of (scattered) SH energy, because (as mentioned before) P and SV waves do not generate rotations around the vertical axis. The zero-lag normalized cross-correlation coefficient - defined between zero (no similarity) and one (perfect match) - between vertical rotation rate and transverse acceleration was calculated for a sliding time windows of appropriate length (twice the dominant period) along the time series. After high-pass filtering both signals (transverse acceleration and rotation rate) with cut-off period $T=1s$, using 2s sliding time window, the results reveal a clear increase of the coefficients right after the onset of P (Figure 2.3, bottom panel). The same processing for all events in the period 2003-2004 shows a clear increase of the correlation coefficients between high-pass filtered rotation rate and high-pass filtered transverse acceleration at (and following) the onset of P waves for all events (Figure 2.4). This result indicates the existence of high frequency P coda rotations for all events, sometimes hidden in the noise.

In order to quantify and document the observations systematically, we focus on four earthquakes with visible P-coda rotations (signal-to-noise ratio $[S/N] \geq 1.86$). Their magnitudes, epicenter distances, and back azimuths are given in Table 2.2.

2.2.4 Frequency Dependence of Correlation

One of the expectations of ring laser measurements is to help seismologists separating P and S waves in the wave field (e.g., Takeo, 1997). The appearance of P coda rotations seems to frustrate that hope. Since the dominant periods of directly arriving energy of P and S waves are different, we investigate the cross-correlation between high-pass filtered transverse acceleration and vertical rotation rate as a function of time and cutoff period. Sliding window lengths were taken twice as long as the cutoff periods. The cutoff period range was chosen large enough to cover at least the dominant periods of the directly arriving P energy

(around 1s) and S energy (around 5s). Typical results are shown in Figure 2.5a,b (see also Igel et al., 2007). At the bottom subplots, the zero-lag normalized cross-correlation coefficients as a function of time and cutoff period are presented in the same window as the seismograms. At high frequencies, we can see a sharp increase in correlation at and following the direct P wave (subplot four from top and the bottom panel). This correlation smears out and becomes less pronounced with increasing period, while the corresponding correlation of SH- and Love-wave type signals increases with period. It is interesting to note the distinct increase of correlation at specific arrival times. This may well indicate specific seismic phases (shear waves, P-S conversions).

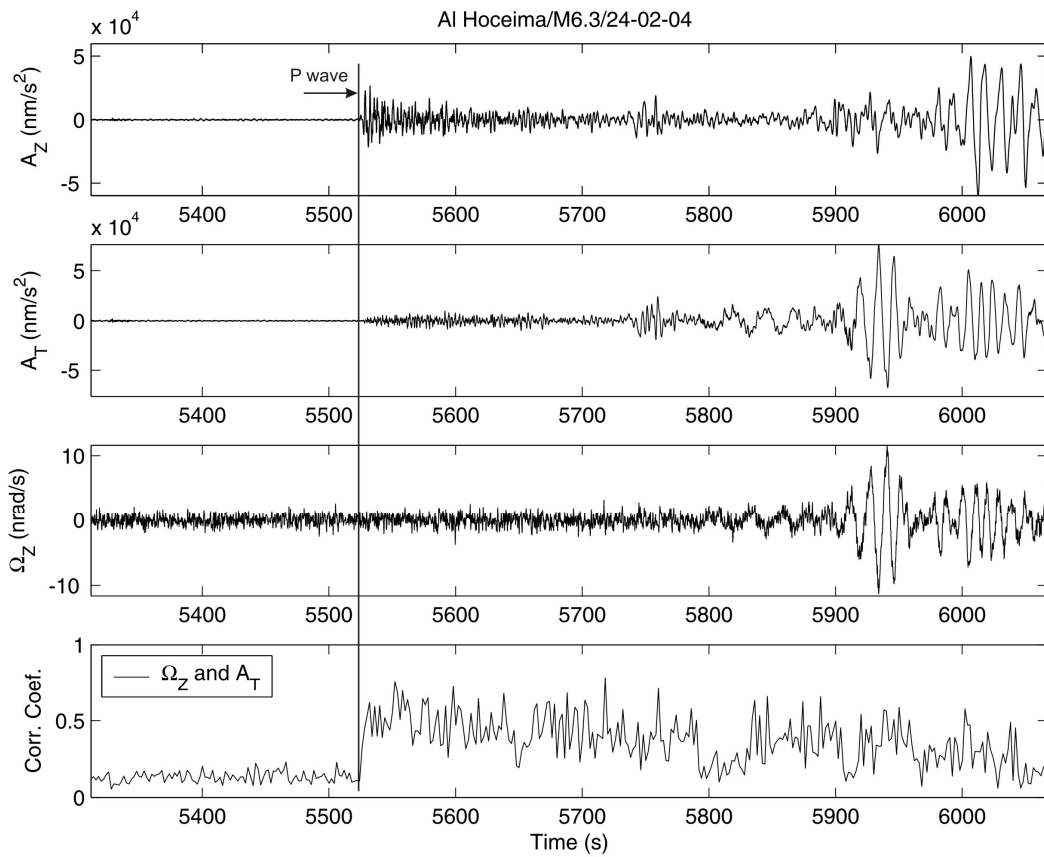


Figure 2.3. Top three traces: vertical, transverse accelerations and rotation rate, respectively, for the 24 February 2004 M6.4 Al Hoceima event. Bottom panel: zero-lag normalized cross-correlation coefficients between rotation rate and transverse acceleration calculated for 2s sliding time windows (after high-pass filtering with cutoff period of 1s).

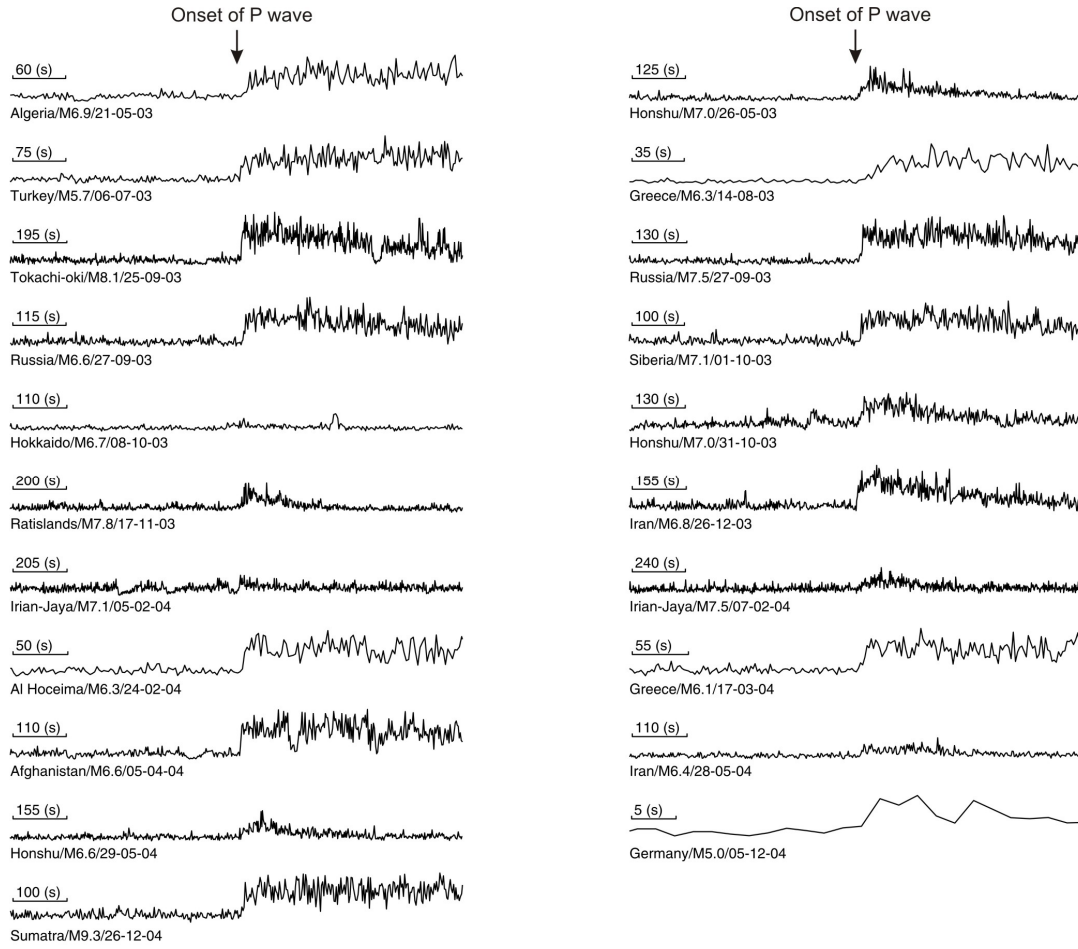


Figure 2.4. Zero-lag normalized cross-correlation coefficients between rotation rate and transverse acceleration in 2s sliding time windows (after high-pass filtering with cut-off period of 1s) calculated for 21 events observed in 2003-2004. The correlation coefficients increase at and following the onset of P waves in all these observed events.

2.2.5 Directional Dependence of Correlation

So far, the translation data were rotated into transverse and radial components according to the theoretical back-azimuth derived from known coordinates of earthquake epicenter and observation station. But – as shown in Igel et al. (2007) – the cross correlation is highly azimuth dependant. For S and Love waves it allows estimating back azimuth. In the P coda it may give hints as to where the SH energy comes from. To investigate this further the directional dependence of the correlation between horizontal acceleration and rotation rate is examined in detail.

Table 2.2
Earthquakes Studied in Detail

Date (yy, mm, dd)	Mag. (L,b,S, W)	Lat. (deg.)	Long. (deg.)	Depth (km)	Region	Distance (km)	Baz (deg.)	S/N (P coda)	
								Vz	Rz
03/05/21	6.9	36.96	3.63	12	Algeria	1547.2	212.3	158.18	2.53
03/09/25	8.1	41.80	143.91	27	Tokachi-oki	8828.0	34.9	359.82	2.75
03/09/27	7.5	50.04	87.81	16	Russia	5164.8	58.8	143.24	1.86
07/09/12	8.4	-4.44	101.37	34	Sumatra	10271.0	94.0	58.60	2.93

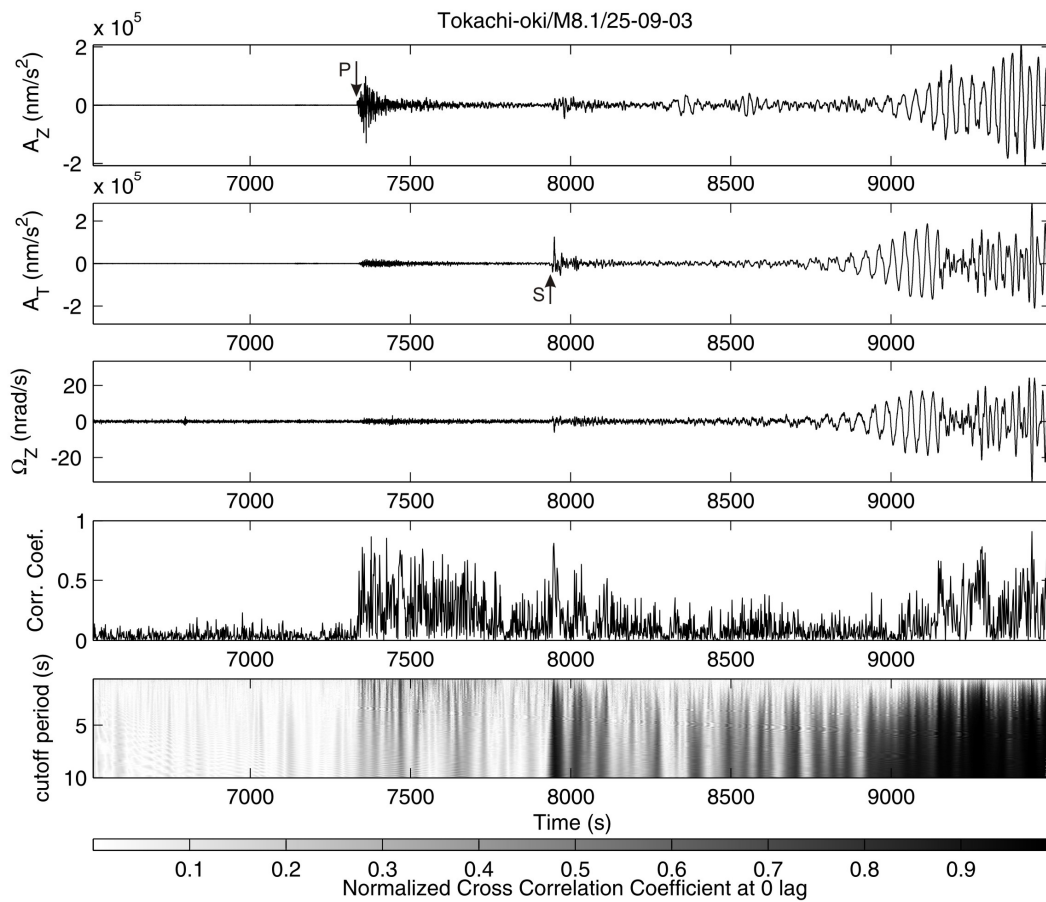


Figure 2.5. (a) Top three traces: vertical, transverse accelerations and rotation rate, respectively, for the 25 September 2003 M8.1 Tokachi-oki event. The fourth trace (from the top): the zero-lag normalized cross-correlation coefficients between rotation rate and transverse acceleration after high-pass filtering with cutoff period of 1s, calculated for 2s sliding time windows. Bottom panel: the correlation coefficients as a function of time and cut-off period (length of sliding time window is twice as long as the high pass cut off period).

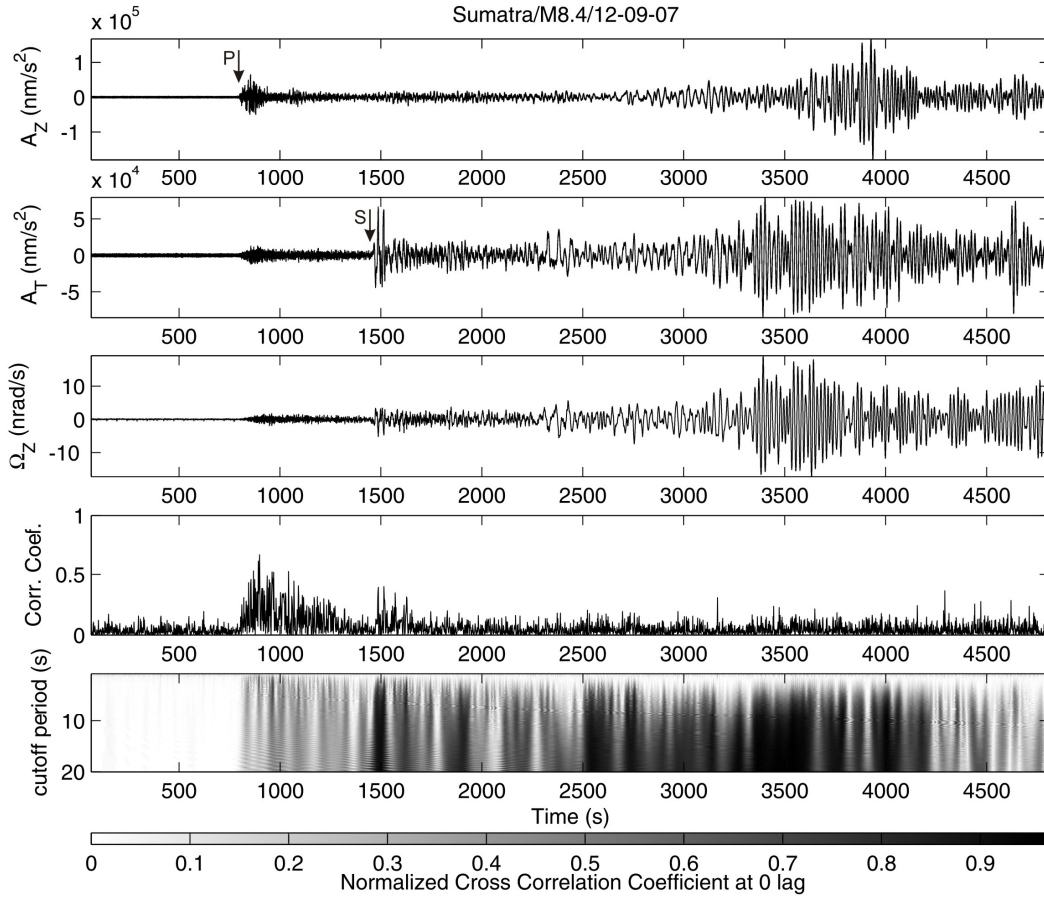


Figure 2.5. (b) Top three traces: vertical, transverse accelerations and rotation rate, respectively, for the 12 September 2007 M8.4 Sumatra event. The fourth trace (from the top): zero-lag normalized cross-correlation coefficients between rotation rate and transverse acceleration after high-pass filtering with cutoff period 1s, calculated for 2s sliding time windows. Bottom panel: the correlation coefficients as a function of time and cutoff period (length of sliding time window is twice as long as the high-pass cut off period).

We calculate horizontal acceleration with assumed back azimuths varying in the range of $0-360^\circ$ then examine the zero-lag normalized cross-correlation coefficients between horizontal acceleration and rotation rate in sliding time windows. High pass filters with appropriate cutoff periods were applied before correlating. Sliding window lengths were taken twice as long as the cutoff periods. Figure 2.6 shows typical results for the case of the Tokachi-oki event. In the fifth subplot (from top) and the bottom panel of this figure, the correlation coefficients as a function of time and assumed back azimuth are shown in the same time window. In the fourth and the fifth subplots cutoff period $T=5s$ and sliding window length 10s were used. High-correlation coefficients are distributed around the theoretical back azimuth (indicated by a horizontal black line) at the

onset times of SH and Love waves. When the cutoff period $T=1\text{s}$ and sliding window length 2s were used (bottom two subplots), we observe at the bottom of this figure that high correlation coefficients are more evenly distributed with angle in the P coda, suggesting rotational energy to come from all directions.

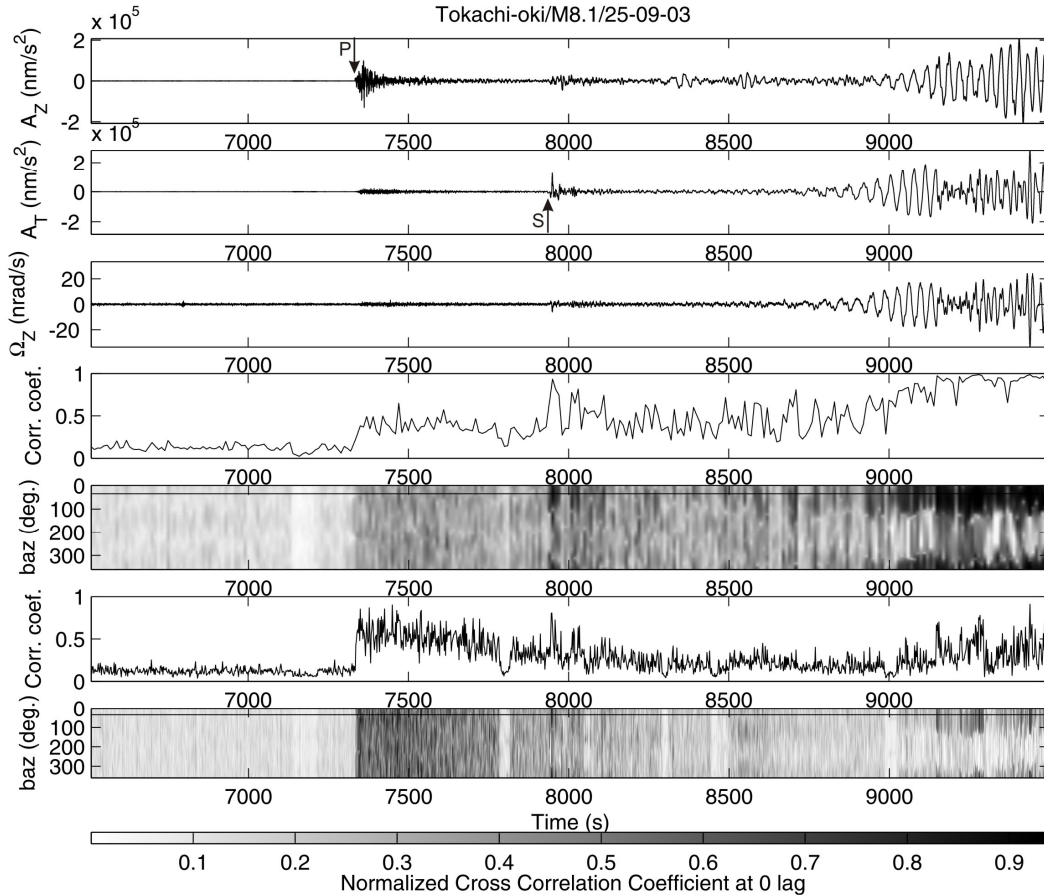


Figure 2.6. Top three traces: vertical, transverse accelerations and rotation rate, respectively, for the 25 September 2003 M8.1 Tokachi-oki event. The fourth and sixth traces (from the top): zero-lag normalized cross-correlation coefficients between rotation rate and transverse acceleration after high-pass filtering with cut-off periods 5s and 1s, calculated for 10s and 2s sliding time windows, respectively. The fifth and bottom panels: the correlation coefficients as a function of time and assumed back azimuth (high-pass filter with cut off period 5s and 1s, sliding time windows of 10s and 2s were applied, respectively). The theoretical back-azimuth is indicated by a horizontal line.

To estimate the back azimuth at longer periods, we sum up over time the correlation coefficients that were calculated with cutoff periods $T \geq 5\text{s}$ (dominant period of directly arriving S wave) over a window containing SH and Love waves. The estimated back azimuth is associated with the maximum of the sum. In Figure

2.7 the distribution of the normalized sums as a function of assumed back azimuth are shown for four typical events (Algeria 21 May 2003 M6.9; Russia 27 September 2003 M7.5; Tokachi-oki 25 September 2003 M8.1; Sumatra 12 September 2007 M8.4). For all these events, there exist clear maxima. The theoretical back azimuths indicated by horizontal black lines correspond almost exactly to the peaks of the normalized sums. The estimated and theoretical back azimuths, respectively, are 223° and 212° (Algeria event), 63° and 59° (Russia event), 38° and 35° (Tokachi-oki event), and 86° and 94° (Sumatra event). The difference can be explained by the influence of 3D structure on the propagation direction or the non-planarity of the wave fronts. This processing can be used to estimate the direction of the incoming seismic transversely polarized wave field.

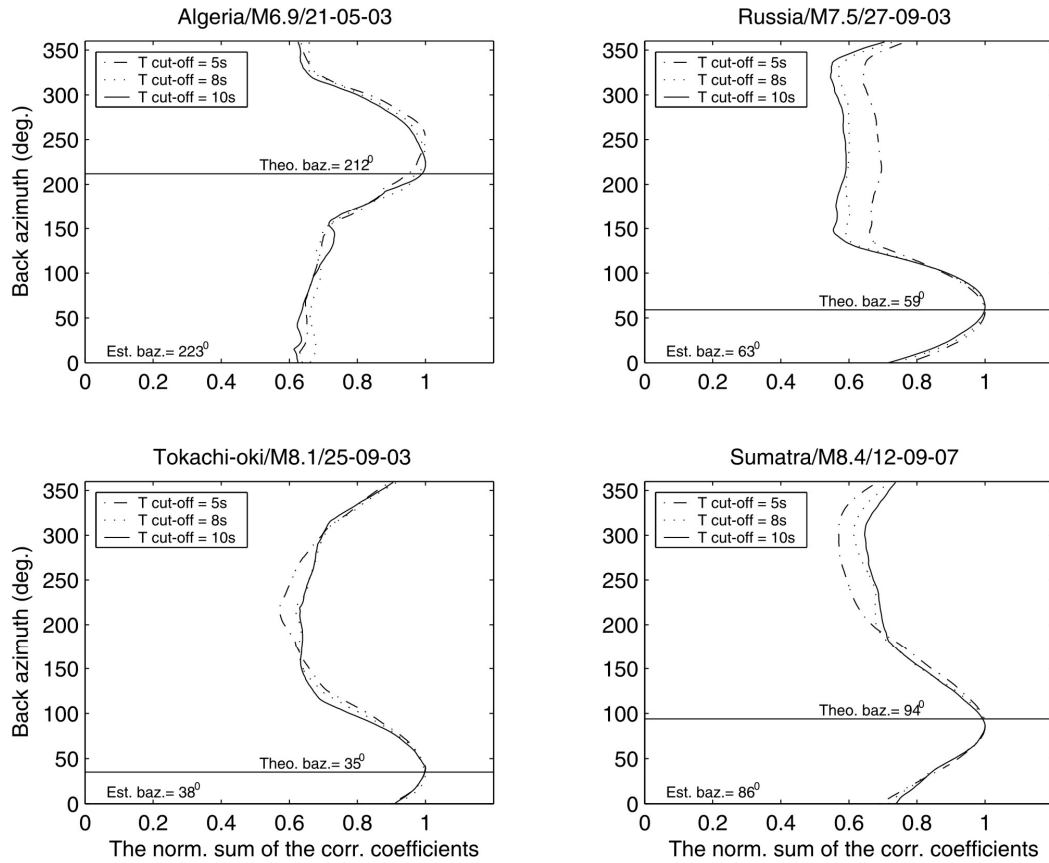


Figure 2.7. Distribution of the (normalized) sum of the correlation coefficients (between rotation rate and transverse acceleration after high-pass filtering with cut-off period 5s, 8s and 10s, length of sliding time window are twice as long as the cut off period applied before correlating) in the window containing direct SH and Love waves of several observed events as a function of assumed back azimuth.

To investigate the direction of the incoming energy of P-coda rotations, we examine the distribution of the same normalized sums over the window of the P coda for cases with cutoff periods $T \leq 2$ s (around dominant period of directly arriving P wave). The results are shown in Figure 2.8. The normalized sums in the P coda have almost even distributions with angle for all four events. This result implies that energies of high frequency rotational motions about a vertical axis in the P coda come from many different directions, indicative of a strongly scattered wave field.

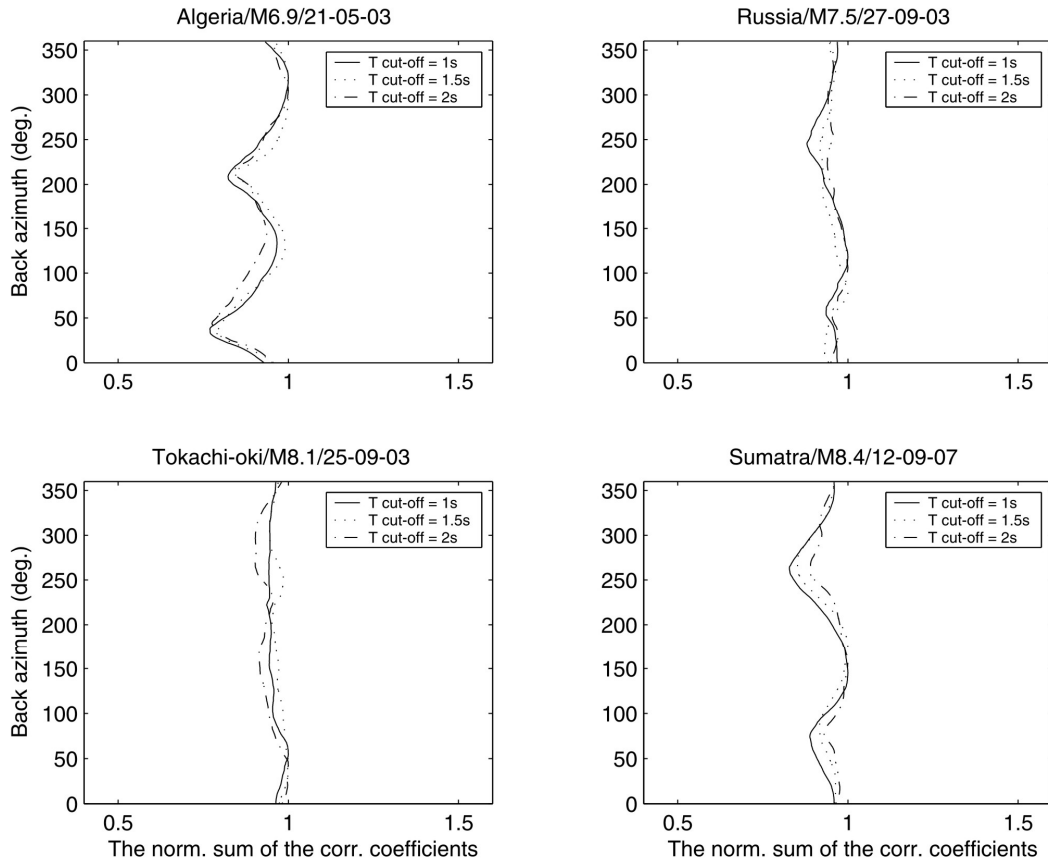


Figure 2.8. Distribution of the (normalized) sum of the correlation coefficients (between rotation rate and transverse acceleration after high-pass filtering with cut-off period 1s, 1.5s and 2s, length of sliding time window are twice as long as the cut off period applied before correlating) in the P-coda window of several observed events as a function of back azimuth. The almost even distribution implies that high-frequency rotational energy in the P coda comes from all azimuthal directions.

2.2.6 Envelopes

As mentioned previously, tilt-ring laser coupling or scattering may contribute to the P-coda rotations. If tilt-ring laser coupling strongly contributes to the observations, energies of the P-coda rotations should appear right after the onset of P waves. Therefore, we investigate in the following the time-dependent variation of energies of observed translation and rotational seismograms in the P coda.

In seismology, the envelope of a time series is an unsigned low pass of the original signal. It shows the time-dependent variation of amplitudes (or energies) of the time series. The normalization erases any influence of polarities in order to ease recognition of similarities or differences in the waveforms. However relative amplitudes within the trace are preserved.

The normalized envelope Y of a seismogram X is defined as:

$$Y(t) = \frac{abs(X(t)) + j * H(X(t))}{\max(abs(X(t)) + j * H(X(t)))}. \quad (2.1)$$

In this definition j is the imaginary unit, and H represents the Hilbert transform of time series X .

The normalized envelopes of rotation rate and the vertical and transverse components of ground velocities are calculated. The results for four earthquakes are shown in Figure 2.9. In each subplot (from top, respectively) individually normalized envelopes of vertical, transverse velocities, rotation rate, superposition of the envelopes of vertical and transverse velocities, and superposition of the envelopes of vertical velocity and rotation rate of each event are shown. We can recognize that the amplitude of vertical velocity (the top trace) increases very fast right after the P-wave onset. Whereas, after the arrival time of the direct P wave the amplitude increase of transverse velocity and rotation rate is delayed (the second and third traces from top and the two bottom traces). However, the increases of transverse velocity and rotation rate amplitudes remain even though the amplitude of vertical velocity passes its maximum value and decreases.

2.2.7 Energy Equipartitioning

Previously, to distinguish between the different scattering regimes in the lithosphere Shapiro et al. (2000) and Hennino et al. (2001) proposed using the ratio of energies of curl and divergence of ground motions. Using the curl of the

wave field derived from array-translation measurements, the authors showed that there is an equipartition, indicated by the stabilization of the energy ratio. Since the aforementioned observations imply scattering, we pose the question: can we observe any type of energy equipartitioning from the ring laser measurements?

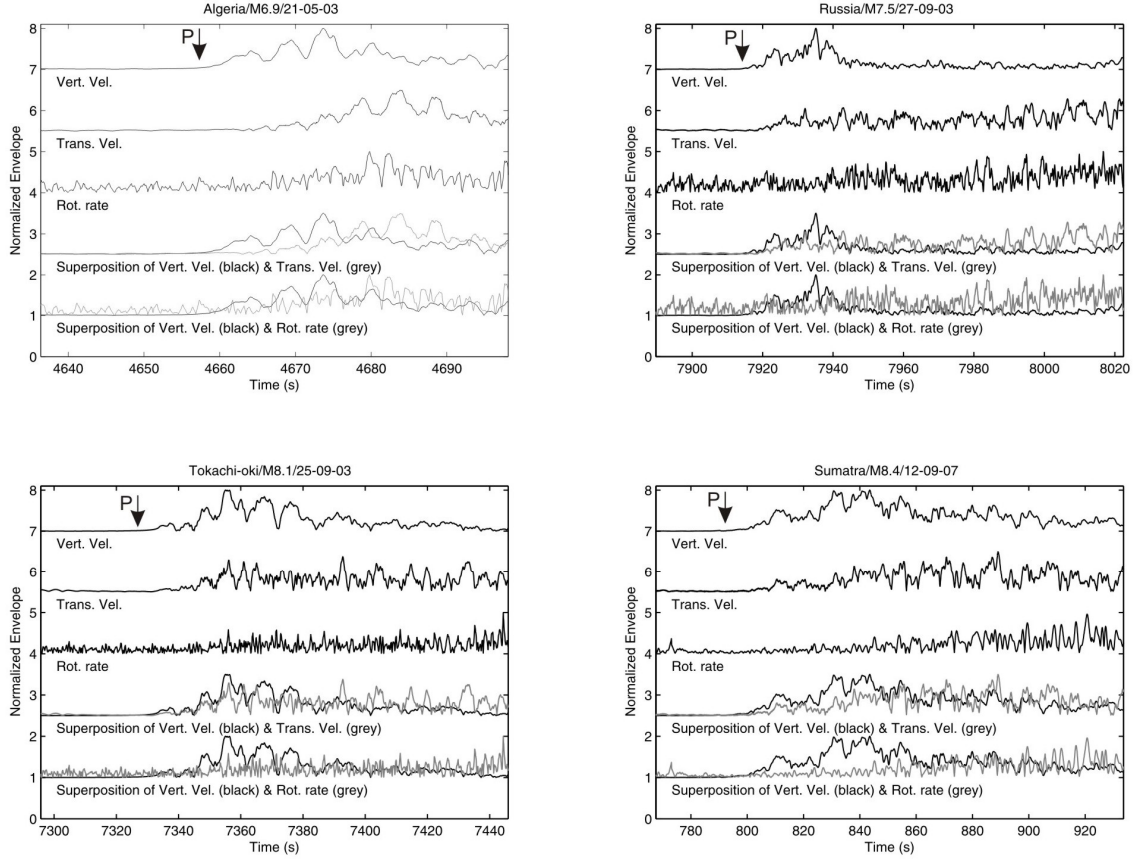


Figure 2.9. Normalized envelopes of individual seismograms and their superposition. For each subplot (from the top, respectively): normalized envelopes of vertical and transverse components of ground velocity, vertical component of rotation rate, and the superposition of the envelopes of vertical and transverse velocities, and the superposition of the envelopes of vertical velocity and rotation rate.

We note that the energy representative, defined as the sum over the squared amplitude, will be referred to as simply as “energy” in the following. More information on the concept of elastic wave energy density can be found in Hennino et al. (2001).

We investigate the ratio of energies of observed rotation rate (Ω_z) and vertical velocity (V_z) in sliding time windows from the onset of P waves along the P coda. The length of the sliding time windows was varied from 5s to 20s. Figure 2.10a

shows a typical result for the case of the 12 September 2007 M8.4 Sumatra earthquake. We observe that after the P arrival, the ratio is reduced (the third trace from top, before 810s). After a short time of decrease, the energy ratio is quite stable until the energy of V_z reaches the maximum value (section between 810s and 860s). Then the energy ratio starts increasing because the amplitude of V_z is decreased while that of Ω_z is still increasing (section between 860s and 965s). The ratio reaches the peak value when the energy of Ω_z in the sliding time window reaches the maximum value. Zooming in the ratio in the section between 800s and 875s (bottom panel) we can see that for cases of window lengths 15s and 20s the ratios have a stable value of about 1×10^{-8} . For smaller window lengths (5s and 10s) the ratios vary around this value. For the case of the 25 September 2003 M8.1 Tokachi-oki earthquake we obtain the same result with the stable value of the energy ratio being about 1.8×10^{-8} (Figure 2.10b, bottom panel, section between about 7340s and 7365s).

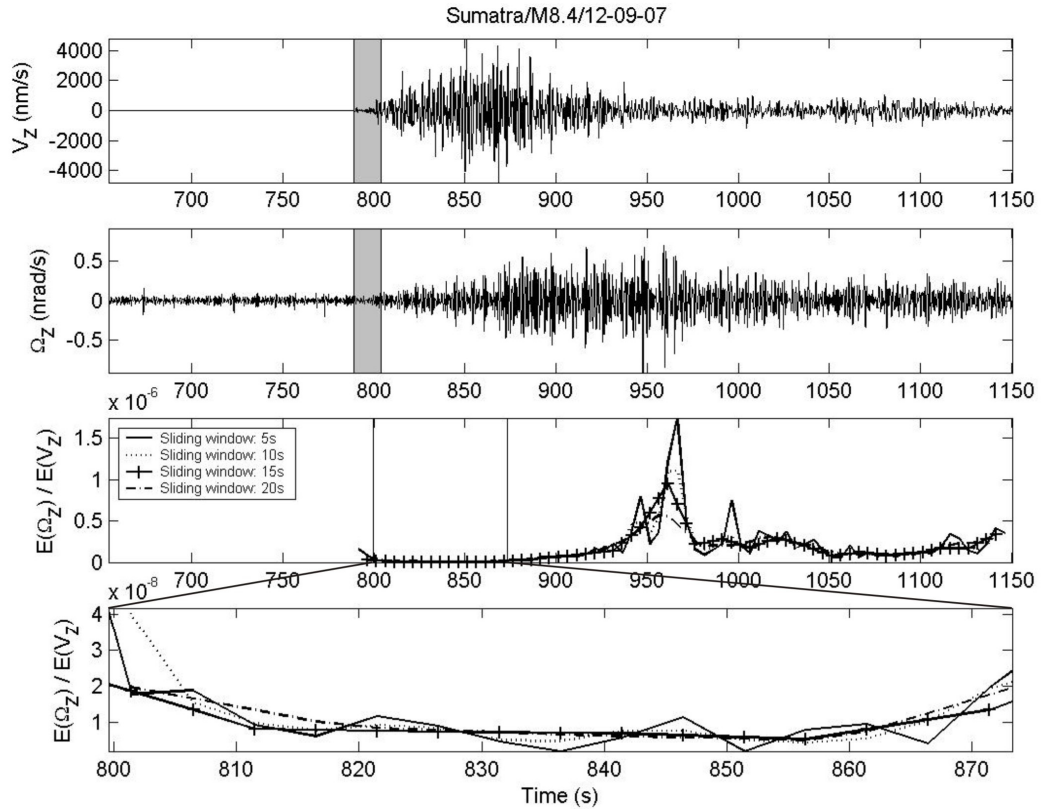


Figure 2.10. (a) Two top traces: vertical components of velocity and rotation rate, respectively, in the P coda of the 12 September 2007 M8.4 Sumatra event after band-pass filtering between 0.5s and 1.5s. Two bottom traces: ratio between energy of rotation rate and energy of vertical velocity calculated for time windows (illustrated by the vertical gray bands in the top traces) of different lengths, starting from the onset of P and sliding along the time series up to the end of the P coda.

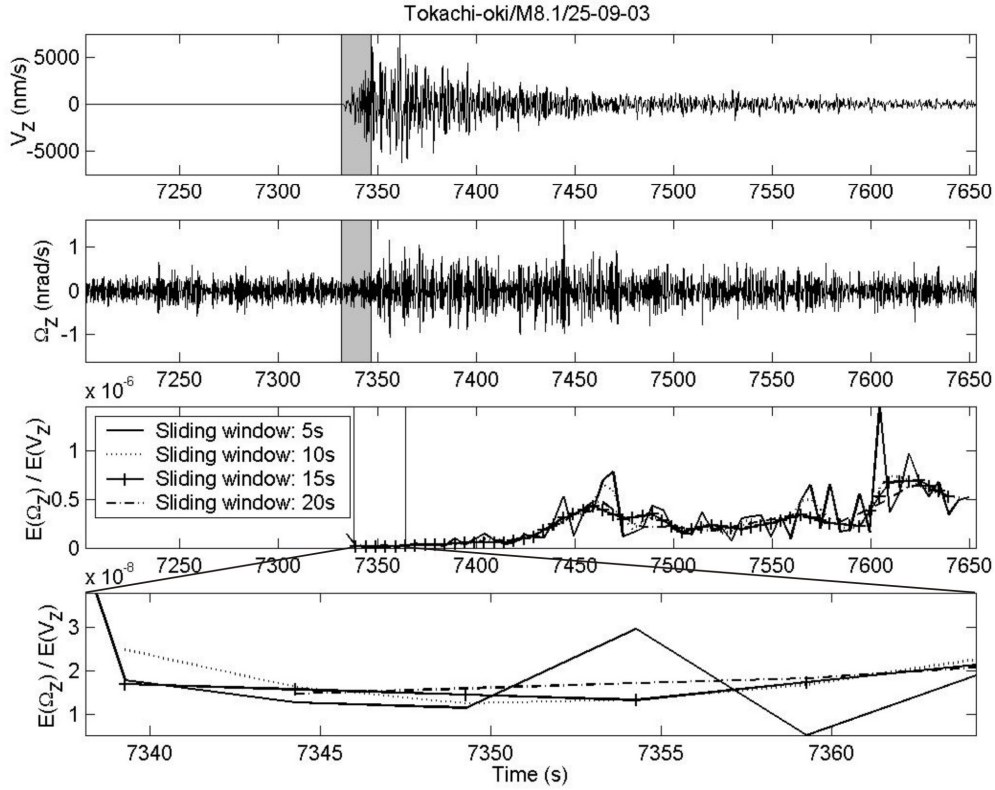


Figure 2.10. (b) Two top traces: vertical components of velocity and rotation rate, respectively, in the P coda of the 25 September 2003 M8.1 Tokachi-oki event after band-pass filtering between 0.5s and 1.5s. Two bottom traces: ratio between energy of rotation rate and energy of vertical velocity calculated for time windows (illustrated by the vertical gray bands in the top two traces) of different lengths, starting from the onset of P and sliding along the time series up to the end of the P coda.

These ratios are calculated for windows of varying duration beginning at the onset of P wave. The results for four typical events are shown in Figure 2.11 with the lengths of the windows given by the horizontal axis. The figure shows that after the window length reaches 15s the energy ratios for different events attain a quite stable value of about $1.1\text{--}2.6 \times 10^{-8}$, almost the same value that we obtained with sliding windows before. This stable value remains in a range of window length from 15s to 35s for all four events (bottom panel). The observations clearly provide further evidence for the partitioning of P and S energies.

Before proceeding to model aspects of these observations, we summarize that the energies of the observed P coda rotations are predominant at high frequencies, come from many different directions, increase with time slower than that of the

direct P waves, and are characterized by the energy equipartitioning. These results suggest that P-SH scattering is the dominant cause for the observations. We proceed to quantify these observations by modeling complete six-component seismograms in 3D media.

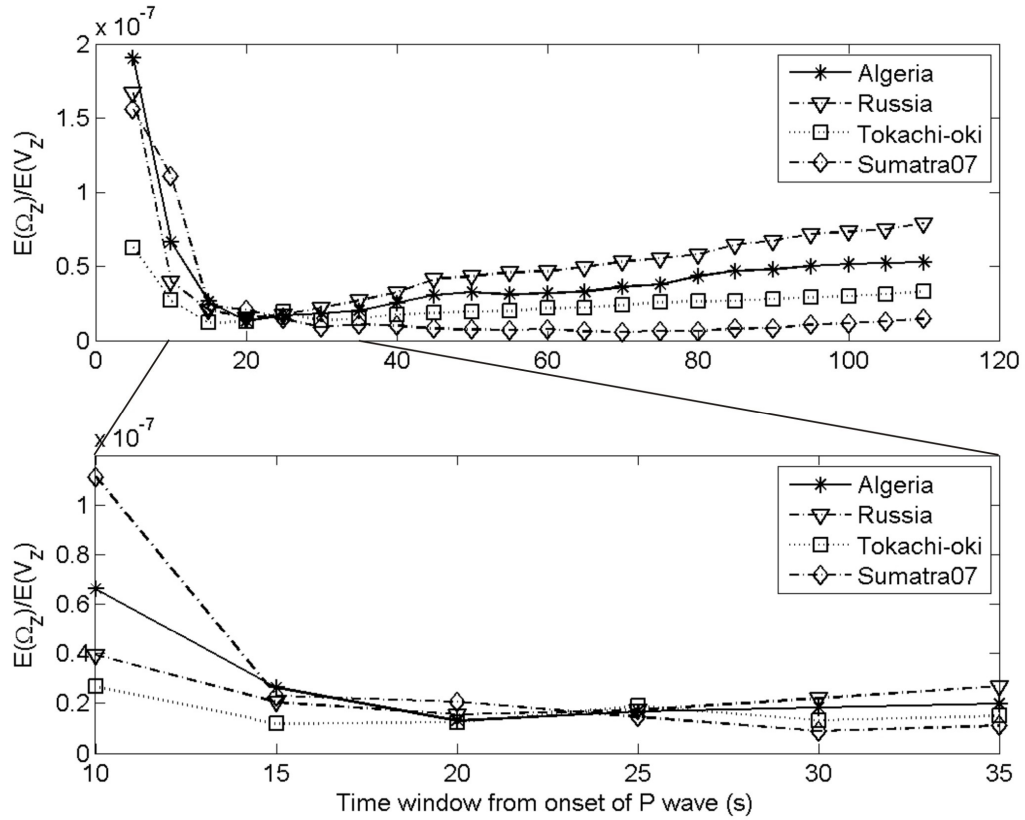


Figure 2.11. Ratios between energy of rotation rate and energy of vertical velocity in typical events calculated for different time windows. All the time windows start at the onset of direct P waves and their lengths are given by the horizontal axis.

2.3 Modeling

To further understand the presented observations, in the following we examine the ability to reproduce the observed P coda rotations under the assumption of scattering through forward modeling. Scattering under the effects of 3D random crust and topography is considered separately. For each study case, except the original assumption (i.e., 3D random scattering or topographic scattering), any other contribution to P coda rotations will be avoided.

2.3.1 P-SH Scattering in the 3D Random Crust

Scattering in heterogeneous media is a phenomenon generated by the interaction between primary waves and inhomogeneities. In this process the amplitudes of the primary seismic waves are reduced as they propagate, but the energy of the propagating wave field is conserved. As mentioned by Stein and Wysession (2003), this process can be described by elastic wave theory in which the governing parameters are: (1) the wavelength of the wave field (or the wave number); (2) the distance that the wave travels through the heterogeneous region; (3) the heterogeneity size; and (4) the velocity perturbation. When the size of the velocity heterogeneities is close to the wavelength of the wave field and the travel distance is large enough compared to the wavelength, scattered energy is predominant (Aki and Richards, 2002; Stein and Wysession, 2003).

The purpose of the forward modeling in this section is to study the generation of P-coda rotations under the assumption of P-SH scattering in the crust. Thus, any other contribution to the P-coda rotations except P-SH scattering needs to be avoided. To satisfy this, we model complete theoretical seismograms created by a plane P wave of dominant period 1s (the same as the predominant period of the observed P waves), propagating upward in vertical direction from the bottom of a random medium.

Random media, in theory, can be generated for desired correlation lengths and velocity perturbations (e.g., Klimeš, 2002). A random medium can be described through a spatial distribution $u(x)$ of material parameters u . This distribution can be expressed as (Klimeš, 2002)

$$u(x) = u_0(x) + U(x), \quad (2.2)$$

where $u_0(x)$ is the mean value of $u(x)$ and $U(x)$ is a realization of the random quantity. In our study, to simplify the modeling, we perform simulations with random media in which the wave velocities are randomly perturbed in space, but the mass density ρ , the ratio between P- and S-wave velocities V_p/V_s , and the mean values of the velocities are kept constant. The realization of the random velocities is calculated in terms of white noise filtered by a spectral filter (see Klimeš, 2002). Since we just consider high frequencies (i.e., small heterogeneities), we choose the spectral filter corresponding to the Zero Von Kármán correlation function mentioned in Klimeš (2002):

$$\hat{f}(k) = \kappa(a^{-2} + k^2)^{-d/4}, \quad (2.3)$$

where a is the Von Kármán correlation length, d is the Euclidean dimension of the space, and κ is a constant corresponding to the given value of perturbation.

To be as realistic as possible, the used model setup is based on the crust model of Bassin et al. (2000) at the Wettzell area. The model is 60800m long, 60800m wide and 40850m deep. The mass density is taken $\rho=2.9 \text{ g/cm}^3$, and the mean values of P- and S-wave velocities (respectively) are $V_p=6600\text{m/s}$, $V_s=3700\text{m/s}$. In order to produce significant scattering energy, we use correlation lengths between 1000m and 15000m (see Aki and Richards, 2002; Stein and Wysession, 2003). Furthermore, the root mean square perturbation of wave velocities is taken in the range from 0% (homogeneity) up to about 11%.

Seismograms are calculated using the ADER-DG method (the combination of a Discontinuous Galerkin finite element method and an Arbitrary high-order DERivative time integration approach developed by Dumbser and Käser, 2006) that was extended to allow outputting the three components of rotation rate, in addition to the three components of translational velocity. The modeling parameters are detailed in Table 2.3.

Table 2.3

The Modeling Parameters Used in This Study

Mesh type	Hexahedral
Element edge length	950m
Total number of elements	176128
Polynomial order inside elements	4
Number of processors	64
Length of seismograms	60s
Boundary conditions	Free surface (top), inflow (bottom), periodic (sides)
Average time step	$8.13008 \times 10^{-3}\text{s}$
Run time per simulation	~ 2 hours

Figure 2.12 illustrates schematically a three-dimensional Von Kármán random medium used in this study with correlation length $a = 2000\text{m}$, root mean square perturbation of 6.51%. In addition, synthetic seismograms obtained at three receivers located at different sites on the surface of the model are shown. For each set of translational velocities (V_x , V_y , V_z) or rotation rates (Ω_x , Ω_y , Ω_z) the amplitudes are scaled. The figure shows that, as waves travel through the random medium, both rotational and horizontal translation components are generated by scattering. The delayed arrival of the vertical rotation compared to the onset of the

vertical velocity that we noticed in the observations can also be clearly seen in our synthetics. Moreover, the simulated seismograms differ at each station because the random field is completely three-dimensional. This allows us to stack aspects of the data from different receivers rather than multiple simulations.

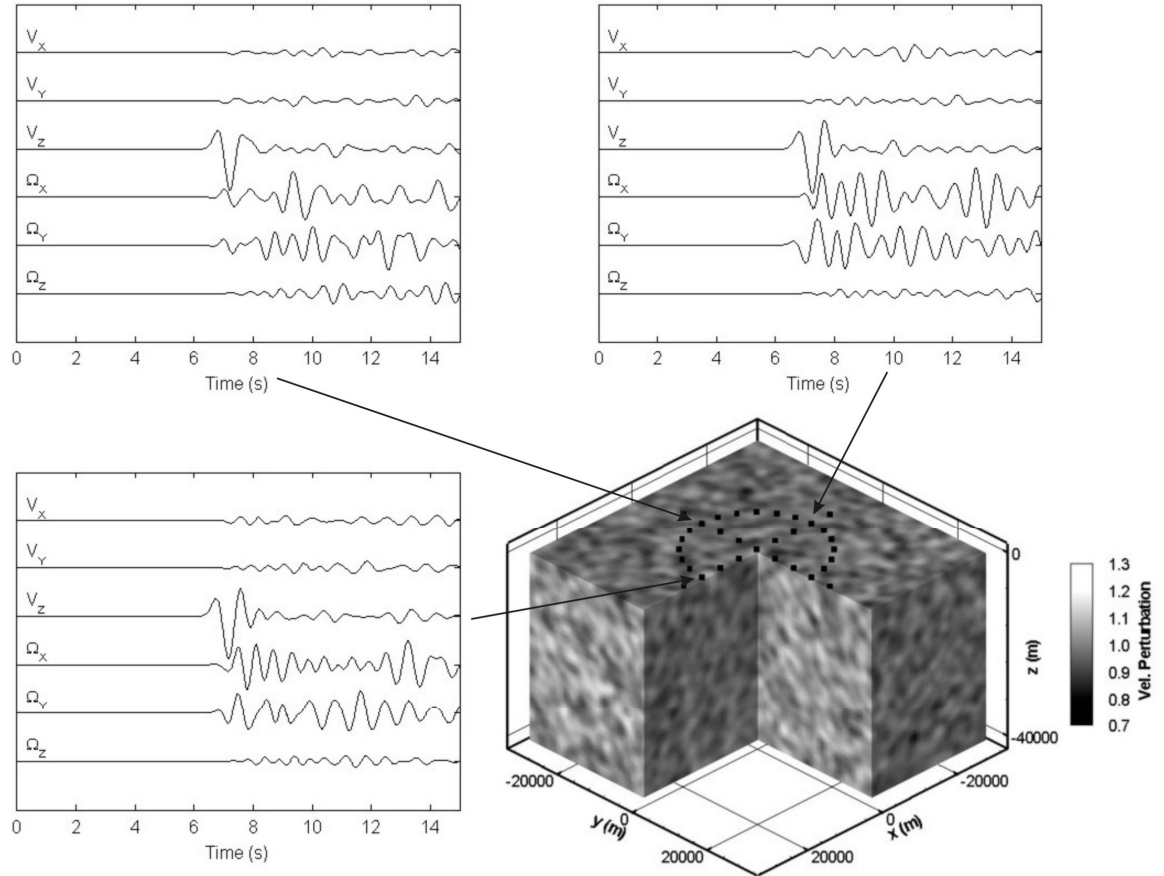


Figure 2.12. Schematic illustration of a 3D Von Kármán random medium used in this study (correlation length $a = 2000\text{m}$, root mean square perturbation of V_S is 6.51%) and six-component seismograms obtained at three different receivers for a plane P wave propagating upward (in a vertical direction) from the bottom of the model. For each set of translational velocities (V_x , V_y , V_z) or rotation rates (Ω_x , Ω_y , Ω_z) amplitudes are scaled.

To investigate systematically the effects of the perturbation on P-coda rotations, we first fix the correlation length to 2000m then calculate seismograms with different velocity perturbation amplitudes. Figure 2.13 shows the simulated seismograms obtained at the receiver located at the center of the model surface as a function of time and velocity perturbation. We can see that for a homogeneous medium (i.e., zero perturbation) no rotations or horizontal translations are generated. Energy in these components appears only in the case of random media.

We can also observe that, as the velocity perturbation increases, the peak amplitudes of these signals increase, while the vertical velocity decreases.

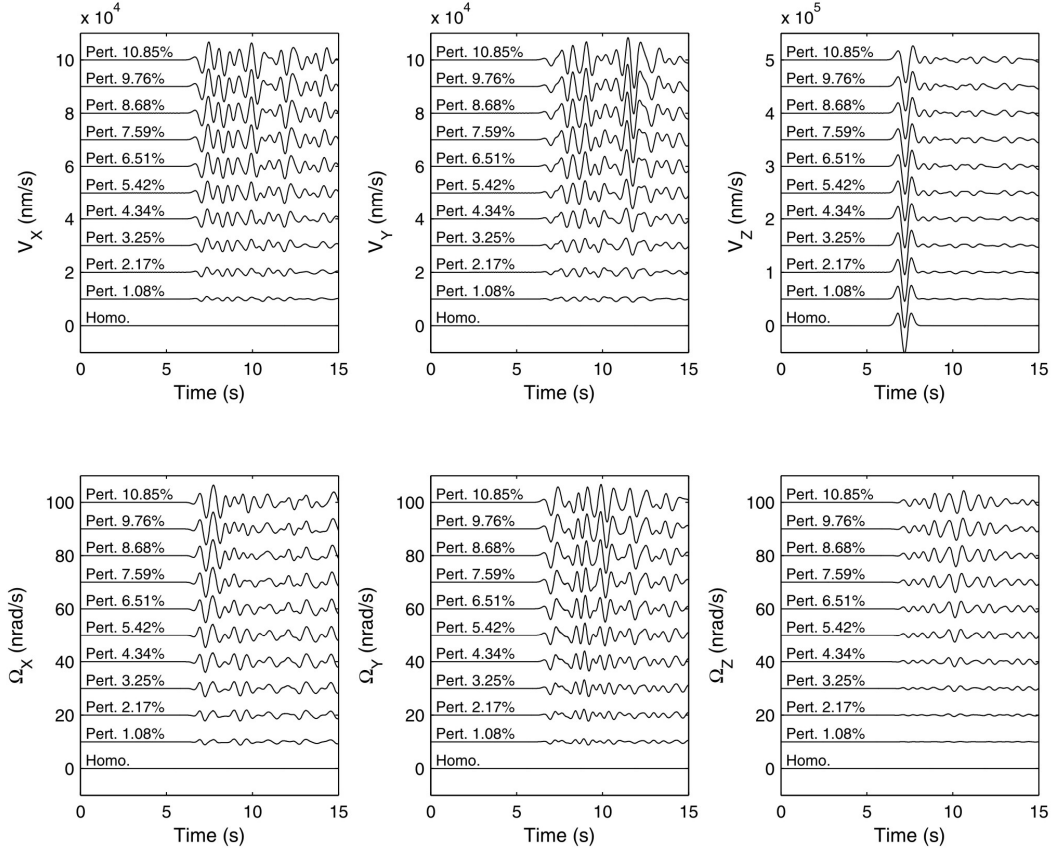


Figure 2.13. Variations of six-component seismograms obtained at one receiver as a function of velocity perturbation of the random medium (correlation length is fixed at 2000m) when a plane P wave propagates upward (in vertical direction) from the bottom of the model.

The effects of the scattering can be quantified by considering both the peak amplitudes and energy of all six components of motion at the surface. Furthermore, since the media are random in all three dimensions, we perform an average of the peak amplitudes and energies computed at 24 receivers located around a circle of a radius 15000m on the surface of the model (see Figure 2.12), taking the first 21s of each trace. In total we investigate 10 different random models characterized by varying velocity perturbations. The results shown in Figure 2.14 imply that part of the energy in the vertical component is scattered into energy of rotational and horizontal motions. This figure suggests that the ratio of energies of rotation rate and vertical velocity can be used to characterize and eventually constrain scattering. Another result illustrated in Figure 2.14 is that the

horizontal components of rotation rate (i.e. tilt) have generally higher amplitudes than the vertical ones.

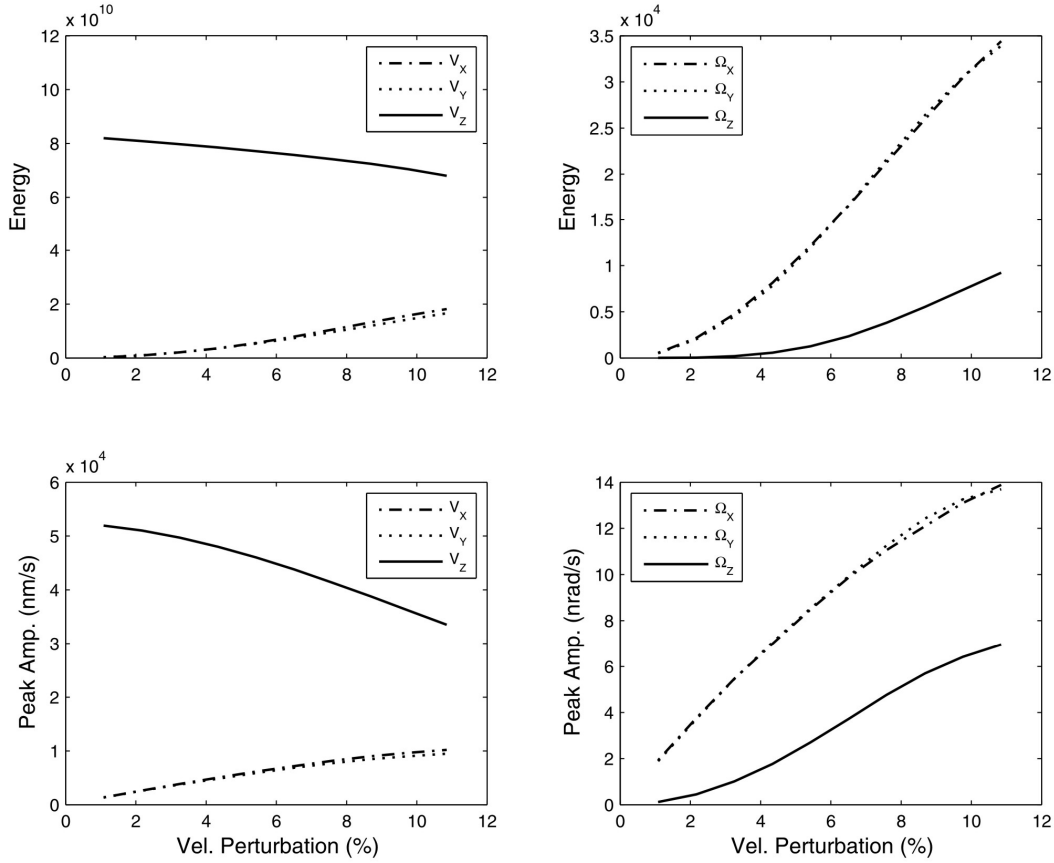


Figure 2.14. Variations of (the average values of) energy and peak amplitude of each translation and rotation component (calculated from 21s seismograms of 24 receivers distributed regularly around a circle of radius 15 km from the center point at the surface of the model – Figure 2.12) as a function of velocity perturbation of the random medium (correlation length is fixed to 2000 m) when a plane P wave propagates upward (in vertical direction) from the bottom of the model.

To compare the simulated P coda rotation with the observed ones the observed stabilization of the ratio of energies of observed rotation rate and vertical velocity is used. We investigate which scattering parameters are compatible with the observed energy ratio. We use a window of 15s length beginning at the onset of the P wave synthetics. For each pair of scattering parameters (a velocity perturbation and a correlation length), we obtain a value of the energy ratio, averaged through all 24 receivers in circular configuration (Figure 2.12). Initially, we take a fixed correlation length of 2000m and calculate the average energy ratios as a function of velocity perturbation. The results are shown as a black

curve in Figure 2.15. As expected, the energy ratio increases as we increase the perturbation. The curve shows a non-linear behavior, with the slope decreasing as the perturbation increases. Similarly, we can calculate the average energy ratio as a function of correlation length at some fixed values of velocity perturbation. We cover a range of correlation lengths from 1000m up to 15,000m and fixed perturbation values of 4.8%, 6.1% and 8%. The results are plotted as squares in Figure 2.15 and strongly suggest that for our model geometry the energy ratio is much more sensitive to the velocity perturbation than to the correlation length.

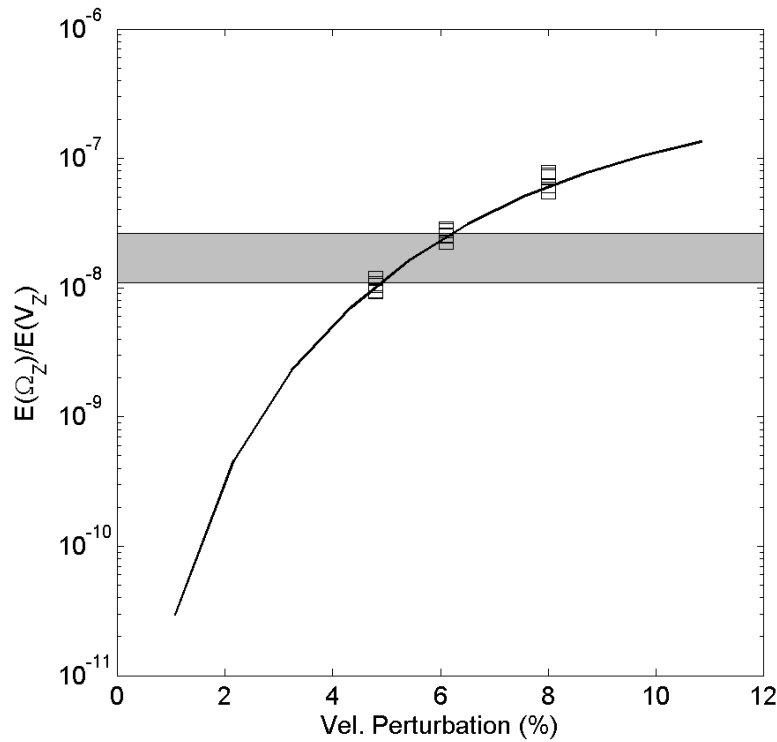


Figure 2.15. Comparison of observed and simulated energy ratios. Black curve: the (average) energy ratio as a function of velocity perturbation calculated from simulated seismograms (correlation length fixed at 2000m); squares, the (average) energy ratio as a function of correlation length (from 1000m up to 15,000m) obtained from simulations; horizontal gray band, range of the energy ratios obtained from observations.

We can finally try to explain the origin of the $1.1\text{--}2.6 \times 10^8$ value for the energy ratio consistently observed at Wettzell. Although the value of the correlation length, that is, the size of the scatterers, cannot be constrained, our simulations show that the observed range of energy ratios (as can be seen in the grey area of Figure 2.15) are compatible with crust models containing velocity perturbation values ranging from 4.8% to 6.5%.

2.3.2 Topographic Scattering

In addition to P-SH scattering in the 3D random crust, topographic scattering may potentially contribute to the observed P coda rotations. To understand this effect in detail, in this section we investigate the generation of P coda rotations under the assumption of topographic scattering only.

We model complete theoretical seismograms created by a plane P wave of dominant period 1s, propagating upward from the bottom of homogeneous media characterized by the top free surfaces with different contrasts in topography. The model size is about 61,000m for each side. The mass density is taken $\rho = 2.9 \text{ g/cm}^3$, and the values of P- and S-wave velocities, respectively, are $V_p = 6600 \text{ m/s}$, $V_s = 3700 \text{ m/s}$. The topographic models that we use here are inferred from the topography of the Wettzell area by the following equation

$$Z_{M(m,n)} = Z_{R(m,n)} + \text{tpf} * [Z_{R(m,n)} - Z_{R(0,0)}], \quad (2.4)$$

where $Z_{R(m,n)}$ is the real altitude of the node (m,n) at the Wettzell area, $Z_{R(0,0)}$ is the real altitude of the Wettzell station, and $Z_{M(m,n)}$ is the modified altitude of the node (m,n) at the Wettzell area with respect to a topographic factor tpf.

The equation (2.4) indicates that: (1) if $\text{tpf} = -1$, the free surface will be flat with altitudes of all the nodes is $Z_{R(0,0)}$, (2) if $\text{tpf} = 0$, the free surface corresponds to real topography of the Wettzell area, (3) the topographic contrast of the model compared to the real Wettzell condition is increased if $\text{tpf} > 0$ and decreased if $-1 < \text{tpf} < 0$, and (4) the altitude of the Wettzell station is always kept constant: $Z_{M(0,0)} = Z_{R(0,0)}$ with any value of tpf.

Seismograms are calculated using the ADER-DG method. To describe realistically the topography, the tetrahedral mesh type is applied. The modeling parameters are detailed in Table 2.4.

Figure 2.16 illustrates schematically the topography at the Wettzell area and six-component seismograms obtained at three different receivers (the Wettzell station is located at the centre) for a plane P wave propagating upward from the bottom of the homogeneous model whose $\text{tpf} = 0$ (which corresponds to the real topography of the Wettzell area). The figure shows that, under the effects of the topography of the free surface, both rotational and horizontal translation components are generated by scattering. The arrival of the vertical rotation is also delayed compared to the onset of the vertical velocity, the same as we recognized from observations data as well as 3D random synthetics. Furthermore, the

simulated seismograms differ at different stations because of the differences of altitudes as well as of the topographic contrasts of the surrounded areas at the stations.

Table 2.4

The Modeling Parameters Used in This Study

Mesh type	Tetrahedral
Start element size	450 m
Growth rate of the element size	1.2
Limit of the element size	3000 m
Total number of elements	~ 700,000 – 950,000
Polynomial order inside elements	4
Number of processors	256
Length of seismograms	~ 22 s
Boundary conditions	Free surface (top), inflow (bottom), periodic (sides)
Average time step	$\sim 2.3319 \times 10^{-4} - 7.9309 \times 10^{-4}$ s
Run time per simulation	36-54 hours

To investigate systematically the effects of the topography on the P coda rotations measured at the Wettzell station, we calculate seismograms for six different topographic models characterized by $tpf = -1, -0.5, 0, 0.5, 1$, and 1.5 . Figure 2.17 shows the simulated seismograms obtained at the Wettzell station as a function of topographic factor tpf . We can see that for the case of a flat free surface (i.e., $tpf = -1$) no rotations or horizontal translations are generated. Energy in these components appears only when there are variations on topography. We can also observe that, as the topographic contrast increases, the peak amplitudes of these signals increase.

The key question is: can topographic scattering be responsibility for the observed P coda rotations? To answer this question, the stabilization of the ratio of energies of observed rotation rate and vertical velocity is used again. We investigate which topographic factor is compatible with the observed energy ratio. We use a window of 15s length beginning at the onset of the P wave synthetics. For each value of the topographic factor, we obtain a value of the energy ratio for the Wettzell station. The results obtained for six investigated models ($tpf = -1, -0.5, 0, 0.5, 1$, and 1.5) are shown as a black curve in Figure 2.18. As expected, the energy ratio increases as we increase the topographic factor. However, all the simulation results are lower and incompatible with the observed range of the energy ratios (as can be seen in the grey area of Figure 2.18).

We summarize that, although P coda rotations can be generated by topographic scattering, such rotational signals at the Wettzell station are insignificant and can not explain the observations.

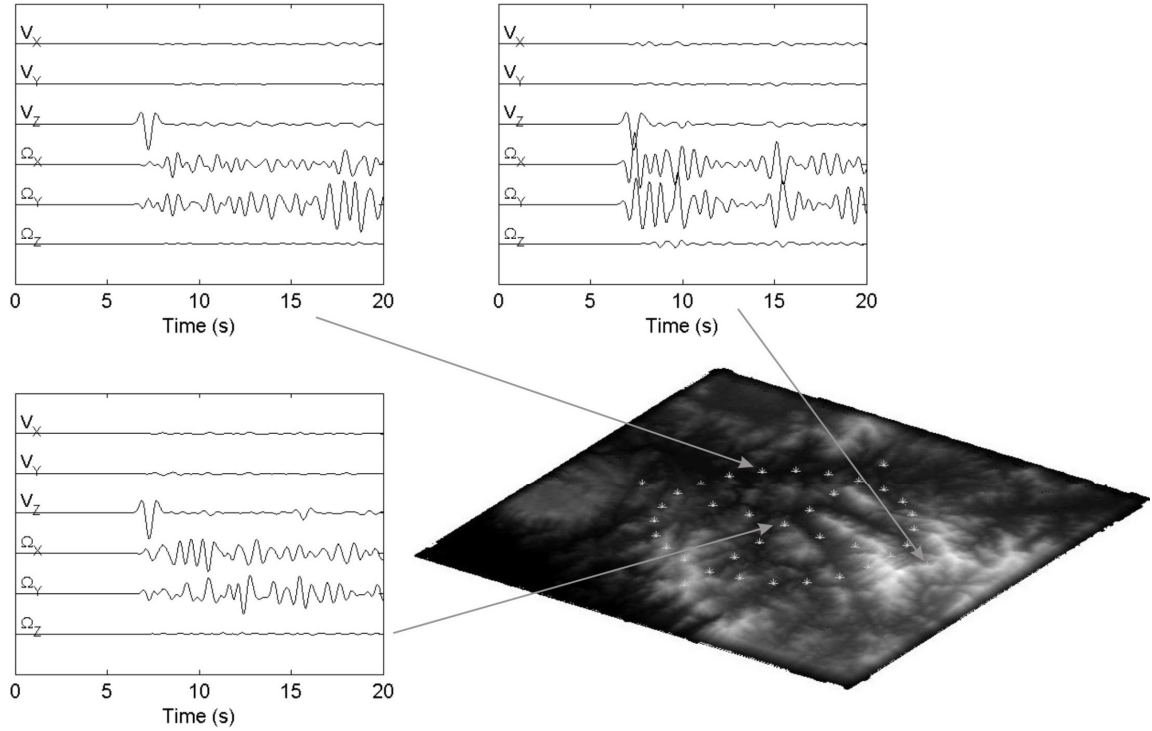


Figure 2.16. Schematic illustration of the topography at the Wettzell area (black: low altitude, white: high altitude) and six-component seismograms obtained at three different receivers (the Wettzell station is located at the centre) for a plane P wave propagating upward (in a vertical direction) from the bottom of the homogeneous model. For each set of translational velocities (V_x , V_y , V_z) or rotation rates (Ω_x , Ω_y , Ω_z) amplitudes are scaled.

2.4 Discussion and Conclusions

The first observations of the ring laser rotational signals in the P coda of tele-seismic events were reported by Igel et al. (2007). However, the origin of the P-coda rotations was unclear. The main goals of this study are (1) to characterize the observations of P-coda rotations in detail, and (2) to model the observations in terms of P-SH scattering.

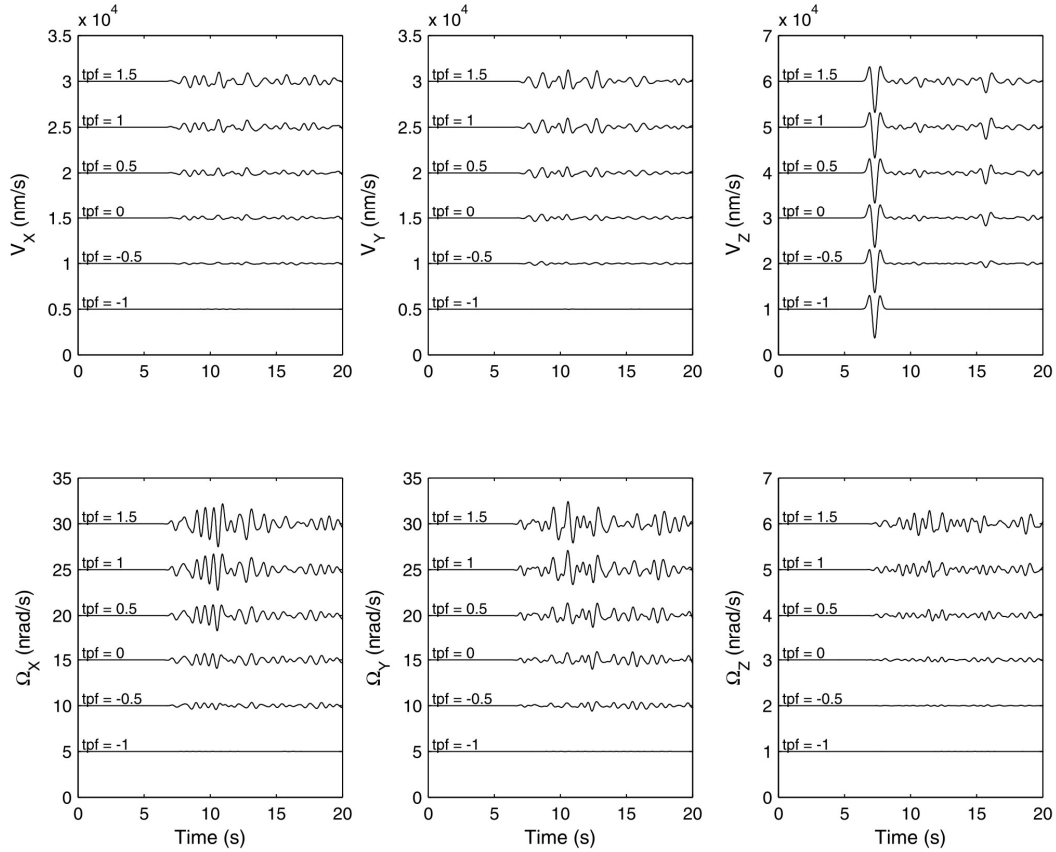


Figure 2.17. Variations of six-component seismograms obtained at the Wettzell station as a function of the topographic factor when a plane P wave propagates upward (in a vertical direction) from the bottom of the homogeneous models.

The observations presented in this study indicate that the energies of the P-coda rotations are predominant at high frequencies, come from many different directions, increase in time slower than that of the energy in the vertical component of translation, and are characterized by the energy equipartitioning. The distribution of cross-correlation coefficients between rotation rate and transverse acceleration as a function of time and cutoff period demonstrates an effective tool to separate direct S waves from the scattering field. The explanation for the P-coda rotations by P-SH scattering is affirmed by the simulation results shown in this study. Under the assumption of a random crustal medium, rotational signals in the P coda can be generated efficiently.

The phenomenon of energy equipartitioning into P and S waves studied by Shapiro et al. (2000) and Hennino et al. (2001) is considered as the principle of multiple scattering. Our study provides further evidence of energy equipartitioning, indicated by the stabilization of the ratio of energies of vertical

rotation rate and vertical translation velocity after the onset of P wave. This stable energy ratio allows us to constrain the velocity perturbation of the random crustal model. Under the assumption of a Von Kármán random medium, we obtain velocity perturbation values ranging from 4.8% to 6.5% for the Wettzell area.

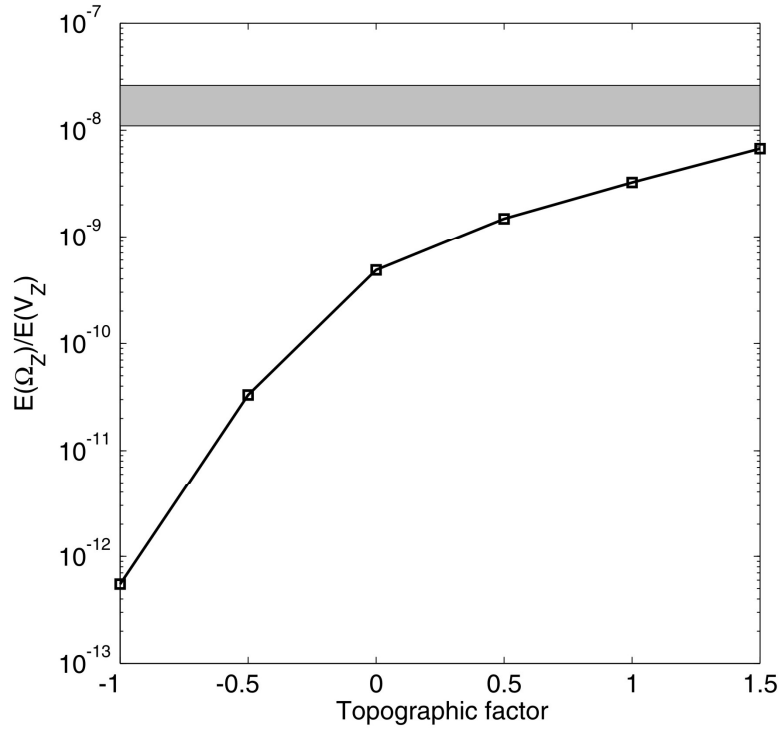


Figure 2.18. Comparison of observed and simulated energy ratios. Black curve: the energy ratio as a function of the topographic factor calculated from simulated seismograms obtained at the Wettzell station; Horizontal gray band: range of the energy ratios obtained from observations. The real topography at the Wettzell area corresponds to the topographic factor zero.

In summary, it can be concluded that P-SH scattering in the random crust can explain the P-coda observations and rotation sensors offer a direct measurement of SH energy and thus may help understanding the partitioning of P and S energy. The P-coda rotations generated by topographic scattering at Wettzell area are insignificant and can not explain the observations. The contributions of anisotropy to the observed P-coda rotations remain an open issue and will be addressed in the next chapter.

Chapter 3

Rotational Motions in Homogeneous Anisotropic Elastic Media*

Abstract

We study rotational motions in homogeneous anisotropic elastic media under the assumption of plane elastic wave propagation. The main goal is to investigate the possible use of collocated measurements of rotational and translational motions for extracting anisotropic properties. The focus is on P-waves that – theoretically – do not have a rotational component of motion in isotropic media. We develop relations for rotational motions of body waves as a function of propagation direction and elastic parameters using the Kelvin-Christoffel equation and the Thomson parameters, descriptive of the degree of anisotropy. We quantify amplitudes of rotation rates and radiation patterns and conclude that 1) amplitudes of quasi P rotation rates in transverse isotropic media depend on two Thomsen parameters ε and δ^* ; 2) for strong local earthquakes and typical reservoir situations quasi P rotation rates induced by anisotropic effects are significant, recordable, and can be used for inverse problems; 3) collocated point measurements of both translational and rotational motions of quasi P waves in transversely isotropic media allow, theoretically, the extraction of anisotropic parameters; and 4) for tele-seismic wave fields anisotropic effects are unlikely to be responsible for the observed rotational energy in the P-coda.

*The contents of this chapter are presented in Pham D.N., H. Igel, J. de la Puente, M. Käser, and M. A. Schoenberg, 2009c, Rotational Motions in Homogeneous Anisotropic Elastic Media that has been submitted to *Geophysics*.

3.1 Introduction

Following advances in developing instruments that record rotational motions around one or all three orthogonal axes, consistent observations of rotational ground motions are becoming possible (McLeod et al., 1998; Pancha et al., 2000; Schreiber et al., 2006, 2009; Wassermann et al., 2009). As a consequence, studies based on collocated measurements of both translational and rotational ground motions that try to exploit the new type of information grow rapidly (e.g., Igel et al., 2005, 2007; Cochard et al., 2006; Suryanto, 2006; Pham et al., 2009a, 2009b; Ferreira and Igel, 2009; Fichtner and Igel, 2009; Bernauer et al., 2009). Results of those studies are reviewed by Lee et al. (2009a, b) indicating the emergence of a new branch in observational seismology and earthquake engineering.

One of the key questions is what additional information – compared to standard translational observations – can be extracted and how. Early studies (Takeo and Ito, 1997) indicated that earthquake rupture histories can be better constrained with measurements of rotational motions. Furthermore, the multi-component point measurements of both rotational and translational motions allow the estimation of wave field properties (e.g. phase velocities, propagation direction, Igel et al., 2007, Cochard et al., 2006), and allow the recovery of shear wave structure without travel time information (Fichtner and Igel, 2009 and Bernauer et al., 2009), as well as constraining the scattering properties of the near-receiver crustal structure (Pham et al., 2009b).

An aspect that has been missing so far in the theoretical developments of inverse methods and processing tools was the inclusion of anisotropic elasticity. It is well known that anisotropy is an important feature in the Earth's crust and upper mantle. The influence of anisotropic effects on seismic processing and interpretation is reported by many authors (e.g., Crampin, 1981, 1984; Crampin et al., 1982, 1984; Sams et al., 1993; Larner, 1993). Tsvankin (1996) emphasized that progress in seismic inversion and processing in anisotropic media depends on our ability to relate different seismic signatures to the anisotropic parameters. In reservoir and drilling engineering, elastic and anisotropic parameters would help in predicting flow paths in improved oil recovery, designing hydraulic fracturing scheme, determining mud weight and selecting drill bit, and preventing hole's collapse during and after drilling (Wang, 2002). Today, to determine anisotropic parameters laboratory measurements or field records of (at least) linear three-component geophones are required.

At the onset of this study there are several open questions: 1) How does anisotropy affect rotational ground motions? 2) Can rotational motions help

constraining anisotropic properties? 3) What instrument configurations are necessary to extract the relevant information?

The main goal of this study is to predict expected amplitudes of rotational motions in various situations and their dependence on propagation direction. In addition, we pose the question whether an inverse problem can be set up that allows the recovery of anisotropic parameters from a point measurement only. We approach the problem in an analytical way focusing on the solution of the wave question for plane waves in linear elastic anisotropic media. Moreover, we provide a linearized approximation that allows quick estimates of the amplitudes to be expected as a function of the degree of anisotropy. This study is also relevant to understand the origin of the P coda rotational motions around a vertical axis observed on a ring laser at the Fundamental station Wettzell, Germany, reported by Igel et al. (2007) and Pham et al. (2009b).

3.2 Fundamental Theory

In the framework of classical elasticity, a general plane-harmonic-wave solution for the displacement vector of body waves is

$$\mathbf{u} = A \mathbf{n} \exp[i(\omega t - \boldsymbol{\kappa} \cdot \mathbf{x})], \quad (3.1)$$

where A is the displacement's peak amplitude; $\mathbf{n} = n_1 \mathbf{e}_1 + n_2 \mathbf{e}_2 + n_3 \mathbf{e}_3$ is the unit vector denoting the direction of the particle displacement, i.e. the wave field's polarization; \mathbf{e}_i ($i = 1, 2, 3$) are the unit vectors along the coordinate axes;

$n_i = \frac{u_i}{\sqrt{u_1^2 + u_2^2 + u_3^2}} = \frac{u_i}{A}$ are the direction cosines of \mathbf{n} ; i is the imaginary unit;

$\boldsymbol{\kappa} = \frac{\omega}{v} (l_1 \mathbf{e}_1 + l_2 \mathbf{e}_2 + l_3 \mathbf{e}_3) = \frac{\omega}{v} \mathbf{l}$ is the wavenumber vector; ω , v and $\mathbf{l} = l_1 \mathbf{e}_1 + l_2 \mathbf{e}_2 + l_3 \mathbf{e}_3$ respectively are the angular frequency, the phase velocity and the unit vector denoting the propagation direction of the plane wave; l_i are the direction cosines of \mathbf{l} .

The rotational motions $\boldsymbol{\Omega}$ generated by the plane wave (3.1) can be calculated by taking half of the curl of the displacement field (Igel et al., 2005, Cochard et al., 2006)

$$\begin{aligned}
\mathbf{\Omega} &= \frac{1}{2}(\nabla \times \mathbf{u}) \\
&= \frac{A}{2} i \mathbf{\kappa} \times \mathbf{n} \exp[i(\omega t - \mathbf{\kappa} \cdot \mathbf{x})] \\
&= \frac{A}{2} \frac{i \omega}{v} \begin{pmatrix} l_2 n_3 - l_3 n_2 \\ l_3 n_1 - l_1 n_3 \\ l_1 n_2 - l_2 n_1 \end{pmatrix} \exp \left[i \omega \left(t - \frac{1}{v} \mathbf{l} \cdot \mathbf{x} \right) \right].
\end{aligned} \tag{3.2}$$

The corresponding rotation rates $\dot{\mathbf{\Omega}}$ can be extracted as

$$\begin{aligned}
\dot{\mathbf{\Omega}} &= \partial_t \mathbf{\Omega} \\
&= -\frac{A}{2} \frac{\omega^2}{v} \begin{pmatrix} l_2 n_3 - l_3 n_2 \\ l_3 n_1 - l_1 n_3 \\ l_1 n_2 - l_2 n_1 \end{pmatrix} \exp \left[i \omega \left(t - \frac{1}{v} \mathbf{l} \cdot \mathbf{x} \right) \right].
\end{aligned} \tag{3.3}$$

In anisotropic elastic media, the phase velocity v and the direction cosines n_i depend on the wave propagation direction l_i . Thus, in order to know the rotation rate we evaluate v and n_i by using the Kelvin – Christoffel equation (see Carcione, 2001, p. 11)

$$(\mathbf{\Gamma} - \rho v^2 \mathbf{I}_3) \cdot \mathbf{u} = 0 \tag{3.4}$$

where ρ is the material density - a constant isotropic parameter, \mathbf{I}_3 is the 3x3 identity matrix, $\mathbf{\Gamma}$ is the symmetric Kelvin – Christoffel matrix

$$\mathbf{\Gamma} = \mathbf{L} \cdot \mathbf{C} \cdot \mathbf{L}^T, \tag{3.5}$$

$$\mathbf{L} = \begin{pmatrix} l_1 & 0 & 0 & 0 & l_3 & l_2 \\ 0 & l_2 & 0 & l_3 & 0 & l_1 \\ 0 & 0 & l_3 & l_2 & l_1 & 0 \end{pmatrix}, \tag{3.6}$$

and \mathbf{C} is the elasticity matrix and given by

$$\mathbf{C} = \begin{pmatrix} c_{11} & c_{12} & c_{13} & c_{14} & c_{15} & c_{16} \\ c_{12} & c_{22} & c_{23} & c_{24} & c_{25} & c_{26} \\ c_{13} & c_{23} & c_{33} & c_{34} & c_{35} & c_{36} \\ c_{14} & c_{24} & c_{34} & c_{44} & c_{45} & c_{46} \\ c_{15} & c_{25} & c_{35} & c_{45} & c_{55} & c_{56} \\ c_{16} & c_{26} & c_{36} & c_{46} & c_{56} & c_{66} \end{pmatrix}. \quad (3.7)$$

Whenever a material possesses more than two independent parameters defining the entries of \mathbf{C} , the material's properties as well as the seismic wave velocities depend on the direction of propagation and the material is called *anisotropic* (see Stein and Wysession, 2003, p. 177). Considering all 21 independent coefficients in \mathbf{C} , a triclinic material can be modeled. This is the most general case of anisotropy and includes as special cases all the other crystalline symmetry classes, i.e. monoclinic, trigonal, tetragonal, orthorhombic, hexagonal, cubic and isotropic. One of the most important anisotropic symmetry classes for seismological purposes is transverse isotropy, whose elasticity matrix is (see Carcione, 2001, p. 6)

$$\mathbf{C}(\text{transversely isotropic}) = \begin{pmatrix} c_{11} & c_{12} & c_{13} & 0 & 0 & 0 \\ c_{12} & c_{11} & c_{13} & 0 & 0 & 0 \\ c_{13} & c_{13} & c_{33} & 0 & 0 & 0 \\ 0 & 0 & 0 & c_{55} & 0 & 0 \\ 0 & 0 & 0 & 0 & c_{55} & 0 \\ 0 & 0 & 0 & 0 & 0 & c_{66} \end{pmatrix}, \quad 2c_{66} = c_{11} - c_{12}. \quad (3.8)$$

The isotropic case can be considered as the special case of anisotropy where $c_{11} = c_{22} = c_{33} = \lambda + 2\mu$, $c_{12} = c_{13} = c_{23} = \lambda$, $c_{44} = c_{55} = c_{66} = \mu$ and all the other coefficients are equal to zero. Here λ and μ are the Lamé constants of the material.

Explicitly, the components of the Kelvin – Christoffel matrix are

$$\begin{aligned}
\Gamma_{11} &= c_{11}l_1^2 + c_{66}l_2^2 + c_{55}l_3^2 + 2c_{56}l_2l_3 + 2c_{15}l_3l_1 + 2c_{16}l_1l_2 \\
\Gamma_{22} &= c_{66}l_1^2 + c_{22}l_2^2 + c_{44}l_3^2 + 2c_{24}l_2l_3 + 2c_{46}l_3l_1 + 2c_{26}l_1l_2 \\
\Gamma_{33} &= c_{55}l_1^2 + c_{44}l_2^2 + c_{33}l_3^2 + 2c_{34}l_2l_3 + 2c_{35}l_3l_1 + 2c_{45}l_1l_2 \\
\Gamma_{12} &= c_{16}l_1^2 + c_{26}l_2^2 + c_{45}l_3^2 + (c_{46} + c_{25})l_2l_3 + (c_{14} + c_{56})l_3l_1 + (c_{12} + c_{66})l_1l_2 \\
\Gamma_{13} &= c_{15}l_1^2 + c_{46}l_2^2 + c_{35}l_3^2 + (c_{45} + c_{36})l_2l_3 + (c_{13} + c_{55})l_3l_1 + (c_{14} + c_{56})l_1l_2 \\
\Gamma_{23} &= c_{56}l_1^2 + c_{24}l_2^2 + c_{34}l_3^2 + (c_{44} + c_{23})l_2l_3 + (c_{36} + c_{45})l_3l_1 + (c_{25} + c_{46})l_1l_2
\end{aligned} \tag{3.9}$$

It is clear that (3.4) is an eigenequation for the eigenvalues $(\rho v^2)_m$ and eigenvectors $(\mathbf{u})_m$, $m = 1, 2, 3$. The dispersion relation is expressed by

$$\det(\mathbf{\Gamma} - \rho v^2 \mathbf{I}_3) = 0 \tag{3.10}$$

from which we can obtain the three velocities v_m ($m = 1, 2, 3$) as a function of the direction cosines l_i and the elastic parameters \mathbf{C} . These velocities correspond to the three body wave modes propagating in an unbounded homogeneous medium: the highest value of v_m corresponds to a quasi-P wave (qP); the other two correspond to quasi-S waves (qS1 and qS2). For each solution v we obtain from (3.4) an associated eigenvector \mathbf{u} , hence the polarizations n_i are fully determined. Substituting the estimated v and n_i into (3.3) and assigning an amplitude to the wave's peak displacement A , one can obtain the rotation rates induced by plane waves propagating in homogeneous anisotropic elastic media.

We apply the aforementioned analytical solution in an effort to visualize anisotropic behavior in the rotational wavefield. Similar to the way used by de la Puente (2008) to illustrate the translational wavefield, we present in Figure 3.1 examples of the surfaces of phase velocity and peak rotation rates around two perpendicular components $\boldsymbol{\theta}$ and $\boldsymbol{\phi}$ calculated for qP, qS1, and qS2 waves as a function of the wave propagation direction. Here, $\boldsymbol{\theta}$, $\boldsymbol{\phi}$ and the propagation direction \mathbf{l} create an orthogonal axis system (see the Appendix D for details). The rotation rates around these axes are obtained by rotating the three components of the rotation rates calculated by equation (3.3) in the appropriate direction. We assume a plane harmonic wave of peak displacement $A=10^{-5}$ m and period $T = 1$ s propagating in a TI material (Mesaverde clay-shale). The elastic parameters of the material are taken from Thomsen (1986) and presented in Table 3.1. All plots show the highest values for each propagation direction. We note that, for all three wave types (i.e. qP, qS1, and qS2), no rotational motion around the wave-propagation direction \mathbf{l} is generated. The same result (i.e., no rotational motion around the wave-propagation direction \mathbf{l}) is also obtained for the monoclinic,

orthorhombic, and triclinic materials whose elastic properties were mentioned in de la Puente (2008).

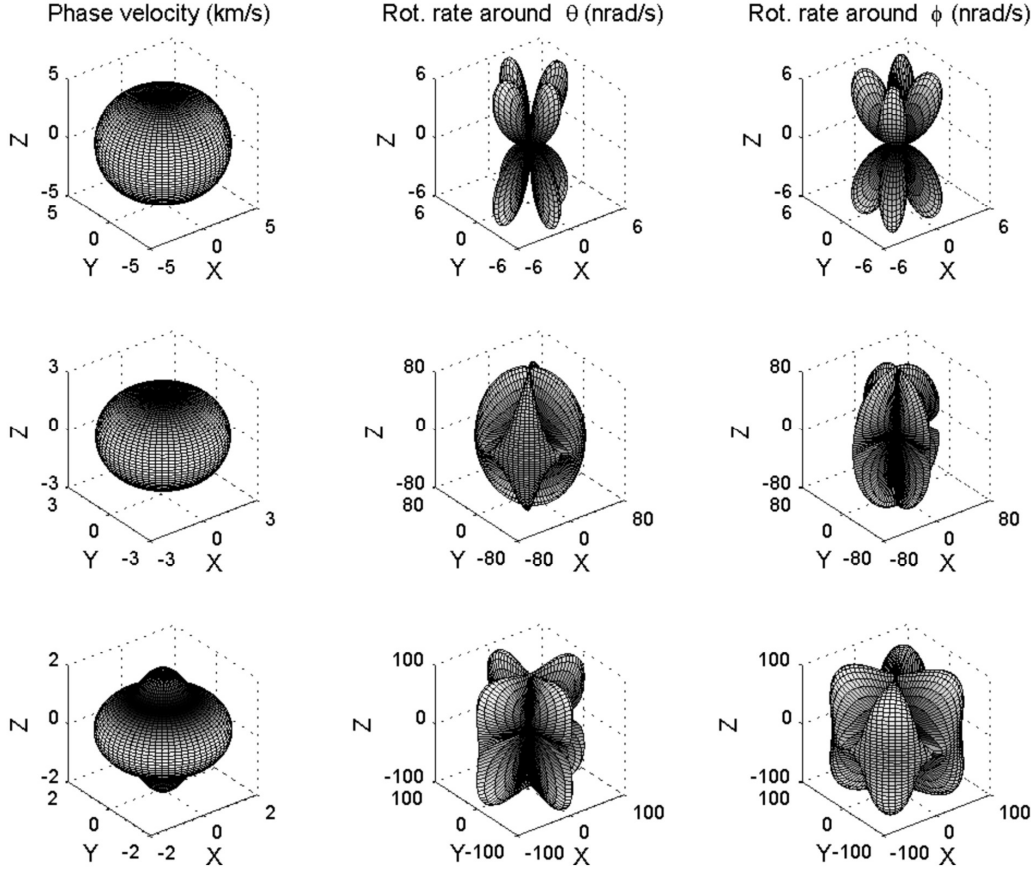


Figure 3.1. Examples of the surfaces of phase velocity (left column) and peak rotation rates around two perpendicular components θ and ϕ (middle and right columns) calculated for qP (top row), qS1 (middle row), and qS2 (bottom row) waves as a function of the wave-propagation direction. Here θ , and ϕ axes in combination with the propagation direction \mathbf{l} create an orthogonal axis system. A plane harmonic wave of peak displacement 10^{-5} m, period $T = 1$ s propagating in a TI material (Mesaverde clay-shale) was assumed. All plots show the highest values at each propagation direction. For all three wave types no rotational motion around the propagation direction \mathbf{l} is generated.

Table 3.1

Elastic parameters for the TI material (Mesaverde clay-shale) given in $[10^9 \text{ N.m}^{-2}]$. The material density ρ is given in $[\text{kg.m}^{-3}]$. All the others parameters are zero.

ρ	c_{11}	c_{12}	c_{13}	c_{22}	c_{23}	c_{33}	c_{44}	c_{55}	c_{66}
2590	66.6	19.7	39.4	66.6	39.4	39.9	10.9	10.9	23.45

The anisotropic effects can be recognized from the surfaces presented in Figure 3.1. They show that phase velocity and rotation rates of a plane wave in anisotropic materials strongly depend on the considered propagation direction. The anisotropic behavior is clearly revealed by the appearance of rotational motions caused by qP waves which should be zero for all directions in homogeneous isotropic materials. This suggests that qP rotational motions can be used to extract anisotropic properties of the medium.

Although there are several symmetry classes in anisotropy, the elastic anisotropy of rocks is usually moderate and, in most cases, a TI symmetry is sufficient to describe its effects in the wavefield (Guéguen and Sarout, 2009). Moreover, transverse isotropy was also reported as the anisotropic case of broadest geophysical applicability (Thomsen, 1986). Thus, hereafter in this study our investigations focus only on rotational motions caused by qP waves in the particular case of TI symmetry class.

Before going further, we try to verify the analytical equations developed in this chapter. In the following we detail the explicit analytical expression of the rotation rates generated by a plane wave propagating in a plane containing the symmetry axis of a TI medium. We will compare the peak rotation rates of qP waves obtained using this analytical solution with the results obtained from numerical simulations using the ADER-DG method extended to anisotropic materials by de la Puente et al., 2007.

3.3 Rotation Rates of qP Waves in TI Media: Analytical Expression and Numerical Simulations

When considering plane P waves propagating in the $(\mathbf{e}_1, \mathbf{e}_3)$ plane ($l_2 = 0, n_2 = 0$) of a transversely isotropic media whose symmetry axis is \mathbf{e}_3 , equation (3.3) can be re-written as

$$\dot{\mathbf{\Omega}} = -\frac{A}{2} \frac{\omega^2}{v} \begin{pmatrix} 0 \\ l_3 n_1 - l_1 n_3 \\ 0 \end{pmatrix} \exp \left[i\omega \left(t - \frac{1}{v} \mathbf{L} \cdot \mathbf{x} \right) \right] \quad (3.11)$$

and the Kelvin-Christoffel equation (3.4) can be simplified as

$$\begin{pmatrix} c_{11}l_1^2 + c_{55}l_3^2 - \rho v^2 & 0 & (c_{13} + c_{55})l_1l_3 \\ 0 & c_{66}l_1^2 + c_{55}l_3^2 - \rho v^2 & 0 \\ (c_{13} + c_{55})l_1l_3 & 0 & c_{55}l_1^2 + c_{33}l_3^2 - \rho v^2 \end{pmatrix} \begin{pmatrix} u_1 \\ u_2 \\ u_3 \end{pmatrix} = 0. \quad (3.12)$$

Equation (3.12) shows two fully uncoupled dispersion relations

$$\begin{aligned} c_{66}l_1^2 + c_{55}l_3^2 - \rho v^2 &= 0 \\ (c_{11}l_1^2 + c_{55}l_3^2 - \rho v^2)(c_{55}l_1^2 + c_{33}l_3^2 - \rho v^2) - (c_{13} + c_{55})^2 l_1^2 l_3^2 &= 0 \end{aligned} \quad (3.13)$$

the phase velocities v of which are (see Carcione, 2001, p. 12)

$$\begin{aligned} v_1 &= \sqrt{(\rho)^{-1}(c_{66}l_1^2 + c_{55}l_3^2)} \\ v_2 &= (2\rho)^{-1/2} \sqrt{c_{11}l_1^2 + c_{33}l_3^2 + c_{55} - D} \\ v_3 &= (2\rho)^{-1/2} \sqrt{c_{11}l_1^2 + c_{33}l_3^2 + c_{55} + D} \\ D &= \sqrt{[(c_{11} - c_{55})l_1^2 + (c_{55} - c_{33})l_3^2]^2 + 4[(c_{13} + c_{55})l_1l_3]^2}. \end{aligned} \quad (3.14)$$

which correspond to three wave types: SH, qSV, and qP, respectively. The uncoupled wave displays particle motion only perpendicular to the $(\mathbf{e}_1, \mathbf{e}_3)$ plane, hence it is a pure shear wave. The coupled waves are two quasi waves (qSV and qP) whose polarizations can be inferred from equations (3.12) and (3.13)₂

$$\frac{n_1}{n_3} = \frac{u_1}{u_3} = s \sqrt{\frac{c_{55}l_1^2 + c_{33}l_3^2 - \rho v^2}{c_{11}l_1^2 + c_{55}l_3^2 - \rho v^2}} \quad (3.15)$$

where $s = -1$ if $l_1l_3(c_{11}l_1^2 + c_{55}l_3^2 - \rho v^2) \geq 0$; $s = 1$ if $l_1l_3(c_{11}l_1^2 + c_{55}l_3^2 - \rho v^2) < 0$.

In the $(\mathbf{e}_1, \mathbf{e}_3)$ plane $u_2 = 0$, using $n_1^2 + n_3^2 = 1$ and equation (3.15) we obtain

$$n_1 = s \sqrt{\frac{c_{55}l_1^2 + c_{33}l_3^2 - \rho v^2}{c_{11}l_1^2 + c_{33}l_3^2 + c_{55} - 2\rho v^2}} \quad (3.16)$$

$$n_3 = \sqrt{\frac{c_{11}l_1^2 + c_{55}l_3^2 - \rho v^2}{c_{11}l_1^2 + c_{33}l_3^2 + c_{55} - 2\rho v^2}}. \quad (3.17)$$

Substituting (3.14)₃, (3.16), and (3.17) into (3.11) the rotation rates induced by qP waves propagating in the $(\mathbf{e}_1, \mathbf{e}_3)$ plane of a TI material can be expressed as a function of the propagation direction as

$$\begin{aligned}
 \dot{\boldsymbol{\Omega}} &= -A\omega^2 \sqrt{\frac{\rho}{2(c_{11}l_1^2 + c_{33}l_3^2 + c_{55} + D)}} \begin{pmatrix} 0 \\ l_3n_1 - l_1n_3 \\ 0 \end{pmatrix} \exp\left[i\omega\left(t - \frac{1}{v}\mathbf{l}\cdot\mathbf{x}\right)\right] \\
 n_1 &= s\sqrt{\frac{D - (c_{55} - c_{11})l_1^2 - (c_{33} - c_{55})l_3^2}{2D}} \\
 n_3 &= \sqrt{\frac{D + (c_{55} - c_{11})l_1^2 + (c_{33} - c_{55})l_3^2}{2D}} \\
 s &= -1 \quad \text{if} \quad l_1l_3 \left[(c_{11} - c_{55})l_1^2 + (c_{55} - c_{33})l_3^2 - D \right] \geq 0 \\
 s &= 1 \quad \text{if} \quad l_1l_3 \left[(c_{11} - c_{55})l_1^2 + (c_{55} - c_{33})l_3^2 - D \right] < 0
 \end{aligned} \tag{3.18}$$

Assuming that ψ is the angle between the wave propagation direction \mathbf{l} and the symmetry axis \mathbf{e}_3 of the TI medium we have

$$\begin{aligned}
 l_1 &= \sin \psi \\
 l_3 &= \cos \psi
 \end{aligned} \tag{3.19}$$

This substitution allows us to calculate the rotation rates induced by qP waves propagating in the $(\mathbf{e}_1, \mathbf{e}_3)$ plane of a certain TI material as a function of ψ .

In order to evaluate the correctness of the analytical solution we model the synthetic seismograms created by a plane qP wave of dominant period 1s propagating upward through a TI medium. A model of 30000m length, 30000m width and 20000m depth is used. The material chosen is Mesaverde clay-shale (Table 3.1). In order to check the effect of different incidence angles, we rotate the material around its symmetry axis in small angle increments. In particular, our material is rotated a full circle inside the $(\mathbf{e}_1, \mathbf{e}_3)$ plane with steps of 5 degrees. Such rotation of the material, having fixed the propagation direction of the plane wave, is equivalent to a test in which the material is fixed and the wave propagation direction is rotated inside the $(\mathbf{e}_1, \mathbf{e}_3)$ plane, instead. In total we investigate 72 different TI models characterized by the angle between the material's symmetry axis and the vertical axis, ranging from 0 to 360 degrees.

Six-component seismograms (three components of rotation rates and three components of translational velocities) are calculated using the ADER-DG method. The modeling parameters are detailed in Table 3.2.

Table 3.2

The Modeling Parameters Used in This Study

Mesh type	Hexahedral
Element edge length	1000m
Total number of elements	18,000
Polynomial order inside elements	4
Number of processors	64
Length of seismograms	5s
Boundary conditions	Absorbing (top), inflow (bottom), periodic (sides)
Average time step	1.4085×10^{-2} s
Run time per simulation	~ 50 s

The simulation results show that there is only rotational signal around the \mathbf{e}_2 axis, as we expected from theory (see equation (3.18)). We superimpose the normalized peak rotation rates around the \mathbf{e}_2 axis obtained from the simulations and analytic approach, as a function of the angle ψ between the wave propagation direction and the symmetry axis of the material in a polar coordinate system. The excellent fit between both results presented in Figure 3.2 indicates the consistency of the analytical and numerical solutions.

We summarize that, for homogeneous anisotropic elastic media, we can estimate the rotational motions caused by a certain plane wave as a function of propagation direction and elastic parameters. The anisotropic behavior is clearly revealed by the appearance of qP rotational motions. In the following we extend the analytical equations to be able to infer the magnitude of the rotation rates associated to qP, depending on the amount of anisotropy that the material displays.

3.4 Quantification of Peak Rotation Rates of qP Waves in Terms of Thomsen Parameters

As reported by Thomsen (1986), for the case of transverse isotropy an alternative and more descriptive set of parameters can be used to fully describe the medium's properties, instead of the five elastic coefficients parameters presented in (3.8).

These parameters are the two elastic equivalent moduli α_0 and β_0 and three coefficients γ , ε , and δ^* (usually called Thomsen parameters) expressed as follows

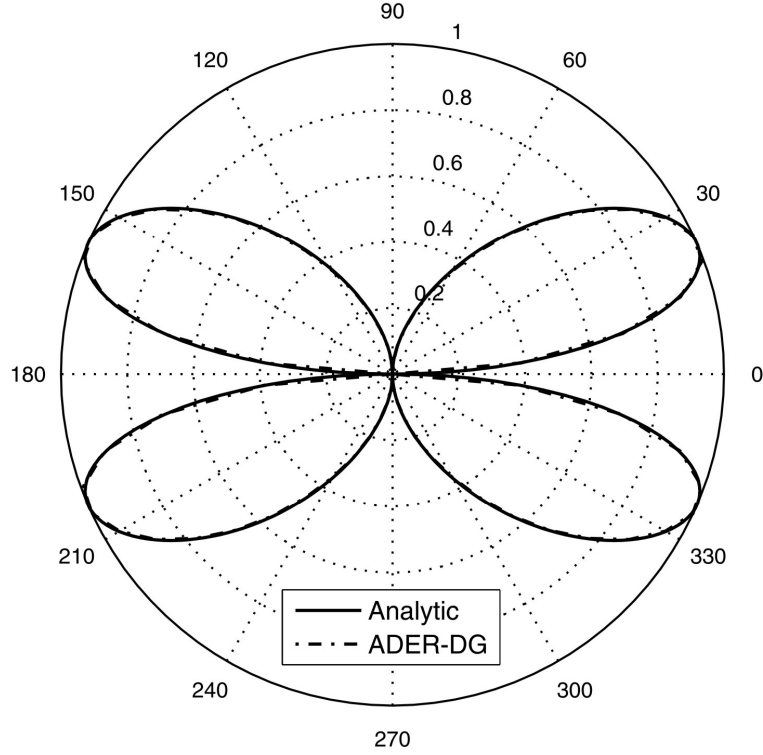


Figure 3.2. Variations of normalized peak rotation rate induced by a qP wave period $T=1s$ propagating in a vertical plane of a TI medium (Mesaverde clay shale) as a function of angle ψ between wave propagation direction and the symmetry axis of the medium. Results are presented in a polar coordinate system. Solid line: analytic result; dash-dot line: numerical simulation result using ADER-DG method.

$$\alpha_0 = \sqrt{\frac{c_{33}}{\rho}} \quad (3.20)$$

$$\beta_0 = \sqrt{\frac{c_{55}}{\rho}} \quad (3.21)$$

$$\varepsilon = \frac{c_{11} - c_{33}}{2c_{33}} \quad (3.22)$$

$$\gamma = \frac{c_{66} - c_{55}}{2c_{55}} \quad (3.23)$$

$$\delta^* = \frac{1}{2c_{33}^2} \left[2(c_{13} + c_{55})^2 - (c_{33} - c_{55})(c_{11} + c_{33} - 2c_{55}) \right]. \quad (3.24)$$

Thomsen (1986) stated that the observed values of vertical P- and S-wave velocities correspond to the α_0 and β_0 values, respectively. The remaining parameters γ , ε , and δ^* are interpreted as three measures of anisotropy. In this section we investigate the dependence of the peak rotation rate values of qP waves on these Thomsen parameters.

Looking at equation (3.18) it is clear that the rotation rates induced by qP waves propagating in the $(\mathbf{e}_1, \mathbf{e}_3)$ plane are independent of c_{66} . This means that, in a certain TI medium with a constant value of β_0 (or equivalently c_{55}), the qP rotation rates are independent of γ (see equations (3.21) and (3.23)). We go further to test whether qP rotation rates depend on γ or not for the general case, when every propagation direction in the full space is considered. We define a set of elasticity matrices \mathbf{C} by assuming fixed values of α_0 , β_0 , ε , δ^* , ρ while letting γ take different values. With each elasticity matrix \mathbf{C} and for each propagation direction we extract the phase velocity and the polarization of the considered qP wave by solving equation (3.10). The corresponding rotation rates are calculated based upon equation (3.3). We further infer the corresponding peak rotation rate by taking the module of the rotation rate vector. In this way we obtain the peak qP rotation rate that can be generated by a certain plane wave in the considered materials, each characterized by its γ value, in all propagation directions \mathbf{l} . The obtained results show a constant value of peak qP rotation rates for all values of γ when certain values of α_0 , β_0 , ε , δ^* , and ρ were assumed. Hence, we conclude that the peak rotation rates induced by qP waves in TI materials are completely independent of the parameter γ and we will consequently skip its consideration in the following.

We can now quantify peak rotation rates of qP waves generated in TI materials with different levels of anisotropy only as a function of the two parameters ε and δ^* . In the following, we consider the values of ε ranging from 0 to 0.35 and those of δ^* from -0.3 to 1. These values cover most TI cases observed (Thomsen, 1986). Four case studies are investigated: 1) A plane wave of peak ground displacement (PGD) 355.78 nm, period $T = 1$ s (caused by a distant earthquake) propagating through bedrock; 2) A plane wave of PGD = 48×10^{-4} m, period $T = 0.8$ s (can be caused by a local earthquake M7.0, epicenter distance 100 km) propagating

through bedrock; 3) A plane wave of $PGD = 10^{-6}$ m, frequency $f = 150$ Hz (can be originated from a micro-seismic event of $M_w = 0$ at hypocenter distance about 1 km) propagating through reservoir rock; 4) A plane wave of $PGD = 180.35 \times 10^{-6}$ m, $f = 5$ Hz (can be caused by an air-gun experiment) propagating through reservoir rock (see Chen et al., 2008). For each case study reasonable values of α_0 , β_0 , and mass density ρ are used, which are detailed in Table 3.3. Because of the independence of the qP rotation rates on γ any arbitrary value of this Thomsen parameter can be taken. Here we note that the first case study is based upon measurements of the 25 September 2003 M8.1 Tokachi-oki earthquake at the Wettzell station, southeast Germany (see Pham et al., 2009a), except for the anisotropy which has been solely added for the purpose of the present research. Therefore, such setting can help us to quantify any possible contributions of anisotropy to the observed P coda rotations reported by Igel et al. (2007) and Pham et al. (2009b).

Table 3.3

Parameters Used in Quantification of Peak Rotation Rates of qP Waves in Terms of Thomsen Parameters for Case Studies.

Case study	Peak ground displacement (m)	Considered period (s)	α_0 (m/s)	β_0 (m/s)	ρ (kg/m ³)
1) Bedrock/ distant earthquake	355.78×10^{-9}	1	6600	3700	2900
2) Bedrock/ local earthquake	48×10^{-4}	0.8	6600	3700	2900
3) Reservoir/ micro-seismic event	10^{-6}	1/150	3928	2055	2590
4) Reservoir/ air-gun experiment	180.35×10^{-6}	0.2	3928	2055	2590

Using the four distinct cases just introduced, we compute for each study case the peak rotation rates of qP waves generated in different TI materials, which are defined by different sets of ε and δ^* values. The results given in Figures 3.3 - 3.6 show the same tendency: that peak qP rotation rates are higher with increasing values of ε and δ^* . When the magnitude of these parameters increases, higher amplitudes of qP rotation rates are generated. Looking at the results obtained for the case of the distant earthquake (Figure 3.3), we conclude that weakly anisotropic bedrock, as that under Wettzell (Lee et al., 2009b), should cause qP rotation rate with values smaller than 5×10^{-11} rad/s. This level is much smaller than the corresponding amplitude (6.3×10^{-10} rad/s) of the observed P coda rotations reported by Pham et al. (2009a). However, for the other study cases

significant amplitudes of qP rotation rates are expected (Figures 3.4-3.6). With peak qP rotation rates in the order of $\mu\text{rad/s}$, even through weakly anisotropic materials, the rotational signals can be recorded by the currently only available commercial rotation sensor R1 (see www.eentec.com, Nigbor et al., 2009; Wassermann et al., 2009). These results raise the motivation for us 1) to develop approximate equations that allow estimating the peak qP rotation rate values to be expected in weakly anisotropic media; and 2) to find out the way to extract material properties from qP rotational motions. We will proceed to these issues in the following sections.

Before ending this section we summarize that the peak qP rotation rate generated by a plane wave in TI media is constrained by just two Thomsen parameters ε and δ^* . Peak rotation rate values induced by the distant earthquakes are expected to be weak, whereas for local earthquakes and active seismics the signals are significant, recordable, and can be used for exploration purposes.

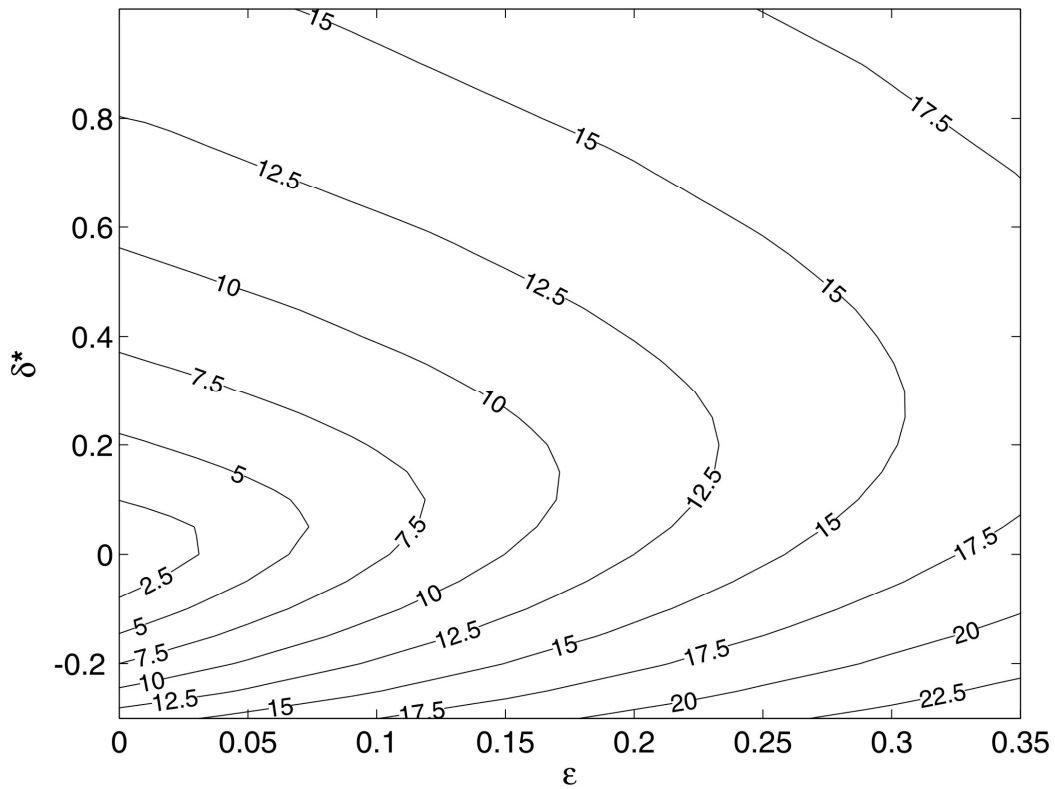


Figure 3.3. Peak rotation rates (in $[10^{-11} \text{ rad/s}]$) caused by plane P waves in a full space TI medium as a function of Thomsen parameters ε and δ^* , expected for a distant earthquake with peak ground displacement 355.78 nm, period $T=1\text{s}$. Vertical P velocity $\alpha_0 = 6600 \text{ m/s}$, vertical S velocity $\beta_0 = 3700 \text{ m/s}$, and $\rho = 2900 \text{ kg/m}^3$ were assumed.

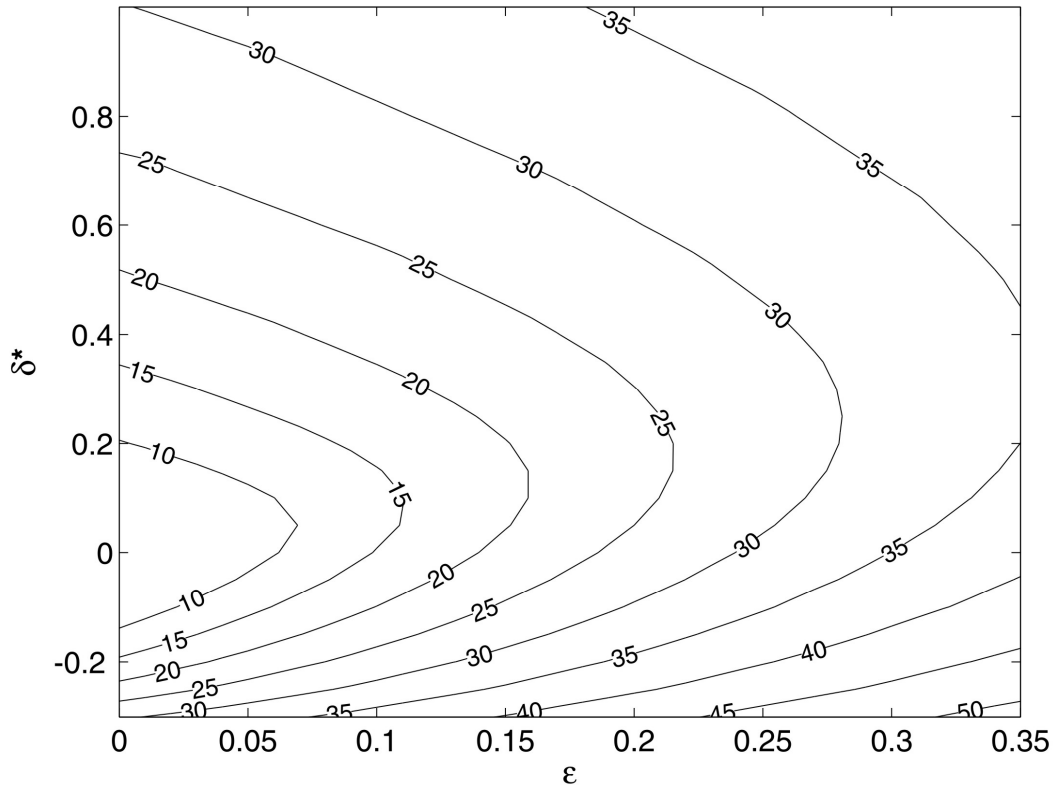


Figure 3.4. Peak rotation rates (in $[10^{-7} \text{ rad/s}]$) caused by qP waves in a full space TI medium as a function of Thomsen parameters ε and δ^* , expected for a local earthquake with peak ground displacement $48 \times 10^{-4} \text{ m}$, period $T=0.8\text{s}$. Vertical P velocity $\alpha_0 = 6600 \text{ m/s}$, vertical S velocity $\beta_0 = 3700 \text{ m/s}$, and $\rho = 2900 \text{ kg/m}^3$ were assumed.

3.5 Estimation of Peak qP Rotation Rate Values for Weakly Anisotropic Media

The computations presented in the last chapter produced the exact peak rotation rate for a series of anisotropic materials and experimental configurations. However, the expression of a closed equation that obtains such values is complicated. As an alternative, one can aim at estimating the peak rotation rate values for certain simpler anisotropy models. Thus, to simplify the complexity of the physical phenomenon described here, we develop an equation that allows us to estimate the peak qP rotation rate in a completely analytical fashion. We will assume $\varepsilon = 0$, thus having $c_{11} = c_{33}$, indicating identical qP wave velocities along the \mathbf{e}_1 and \mathbf{e}_3 axes. Then all anisotropy contributions to the rotation rate come

from the parameter δ^* . We aim at building a first order expansion of the rotation rate around $\delta^*=0$, which has the form

$$\dot{\Omega} = \dot{\Omega}(\delta^* = 0) + \left. \frac{\partial \dot{\Omega}}{\partial \delta^*} \right|_{\delta^*=0} \delta^* + O(2). \quad (3.25)$$

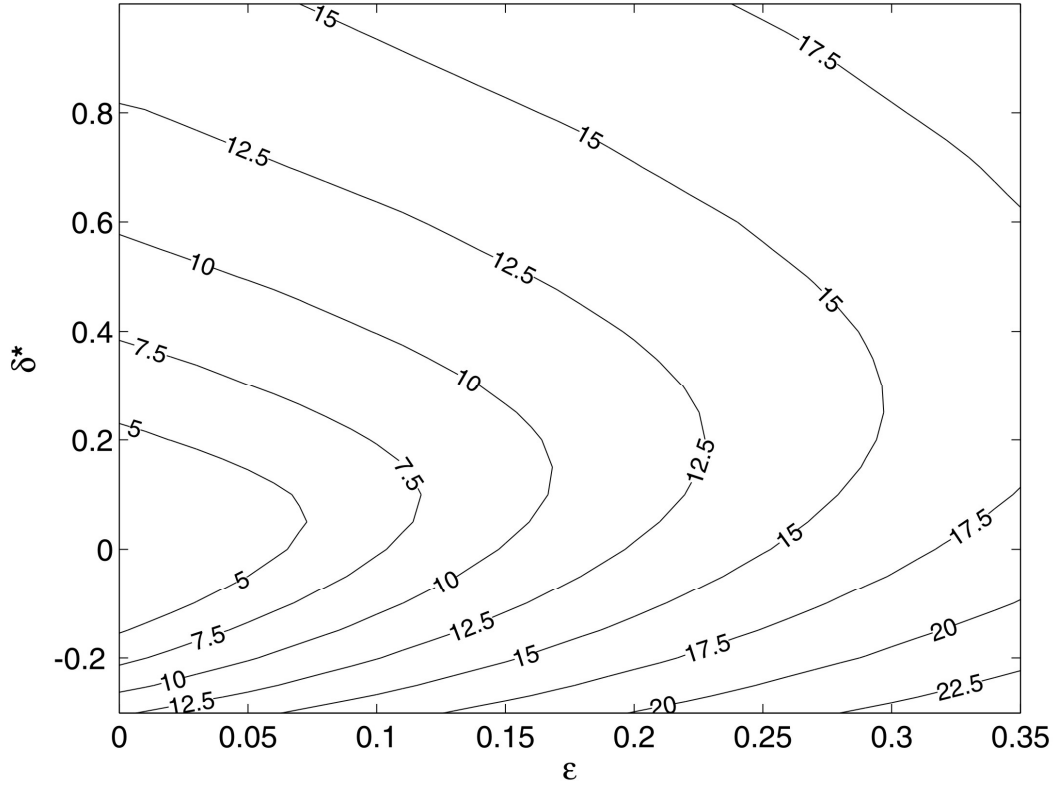


Figure 3.5. Peak rotation rates (in $[10^{-6} \text{ rad/s}]$) caused by qP waves in a full space TI medium as a function of Thomsen parameters ε and δ^* , expected for a reservoir micro-seismic event with peak ground displacement 10^{-6} m , frequency $f = 150 \text{ Hz}$. Vertical P velocity $\alpha_0 = 3928 \text{ m/s}$, vertical S velocity $\beta_0 = 2055 \text{ m/s}$, and $\rho = 2590 \text{ kg/m}^3$ were assumed.

In the following we assume that the phase velocity v is independent of δ^* , an assumption we will revisit later. By construction we know that $\dot{\Omega}(\delta^* = 0) = 0$, which corresponds to the isotropic case, so that we can simplify our approximation as

$$\dot{\Omega} \approx \left. \frac{\partial \dot{\Omega}}{\partial \delta^*} \right|_{\delta^*=0} \delta^*. \quad (3.26)$$

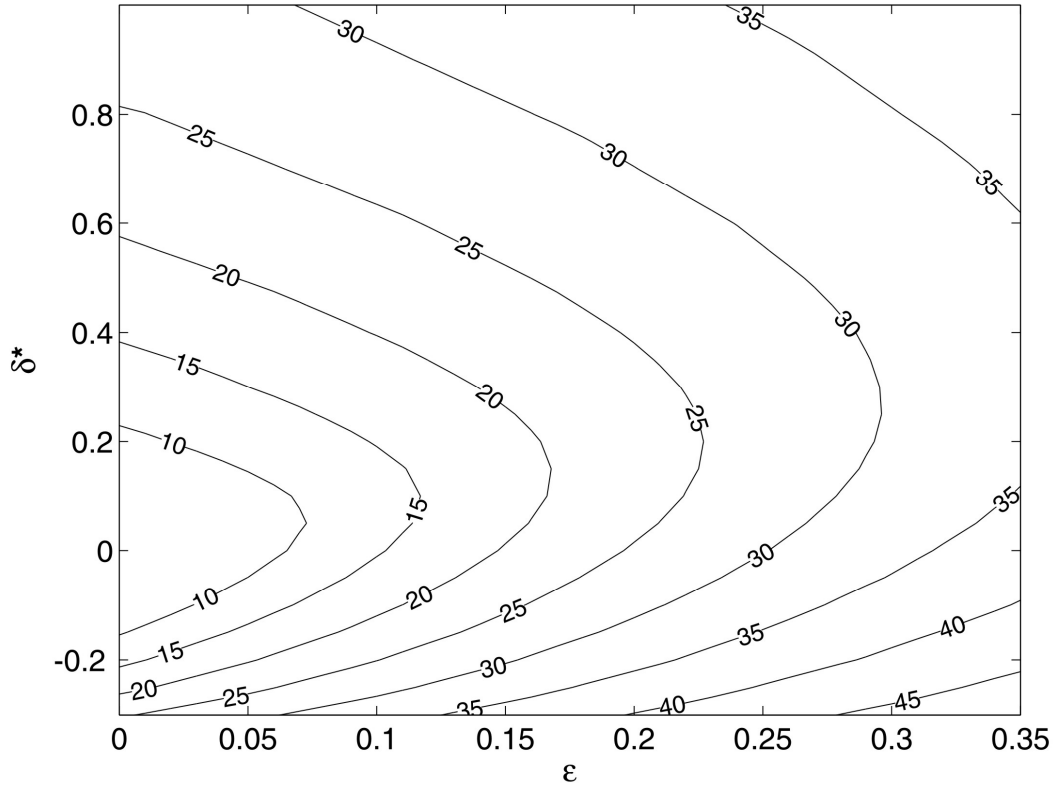


Figure 3.6. Peak rotation rates (in $[10^{-7} \text{ rad/s}]$) caused by qP waves in a full space TI medium as a function of Thomsen parameters ε and δ^* , expected for an air-gun experiment in a reservoir area with peak ground displacement $180.35 \times 10^{-6} \text{ m}$, frequency $f = 5 \text{ Hz}$. Vertical P velocity $\alpha_0 = 3928 \text{ m/s}$, vertical S velocity $\beta_0 = 2055 \text{ m/s}$, and $\rho = 2590 \text{ kg/m}^3$ were assumed.

Now, using the expression (3.11), we can find the peak amplitude of the qP rotation rate as

$$\dot{\Omega} = -\frac{A\omega^2}{2\nu} \frac{\partial(l_3 n_1 - l_1 n_3)}{\partial \delta^*} \bigg|_{\delta^*=0} \delta^*. \quad (3.27)$$

And as l_1 and l_3 are independent on δ^* , in order to know the rotation rate we must evaluate the derivatives of the polarization vectors with respect to δ^* . From equation (3.18)_{2,3} the polarizations can be rewritten as follows

$$n_1 = s \sqrt{\frac{D+a}{2D}}, \quad (3.28)$$

$$n_3 = \sqrt{\frac{D-a}{2D}}. \quad (3.29)$$

Where

$$a = (c_{33} - c_{55})(l_1^2 - l_3^2), \quad (3.30)$$

and D can be simplified from equation (3.14)₄ as

$$D = \sqrt{(c_{33} - c_{55})^2 + 4\delta^* c_{33}^2 l_1^2 l_3^2}. \quad (3.31)$$

The derivatives can be expanded as

$$\frac{\partial n_1}{\partial \delta^*} = \frac{\partial n_1}{\partial D} \frac{\partial D}{\partial \delta^*} = \frac{s}{2\sqrt{2}} \frac{a}{D^2 \sqrt{1+a/D}} \frac{\partial D}{\partial \delta^*}, \quad (3.32)$$

$$\frac{\partial n_3}{\partial \delta^*} = \frac{\partial n_3}{\partial D} \frac{\partial D}{\partial \delta^*} = \frac{1}{2\sqrt{2}} \frac{a}{D^2 \sqrt{1-a/D}} \frac{\partial D}{\partial \delta^*}, \quad (3.33)$$

which using $\delta^* \rightarrow 0$ becomes

$$\frac{\partial n_1}{\partial \delta^*} = \frac{s(l_1^2 - l_3^2)}{4|l_1|(c_{33} - c_{55})} \frac{\partial D}{\partial \delta^*}, \quad (3.34)$$

$$\frac{\partial n_3}{\partial \delta^*} = \frac{(l_1^2 - l_3^2)}{4|l_3|(c_{33} - c_{55})} \frac{\partial D}{\partial \delta^*}. \quad (3.35)$$

The last derivative term in the last expression can be solved to obtain

$$\frac{\partial D}{\partial \delta^*} = \frac{2c_{33}^2 l_1^2 l_3^2}{(c_{33} - c_{55})}. \quad (3.36)$$

Now we have all terms involved in the rotation rate expansion whose peak amplitude takes the explicit form

$$\dot{\Omega} \approx \frac{A\omega^2}{4\nu} \frac{c_{33}^2 l_1^2 l_3^2 (l_1^2 - l_3^2)}{(c_{33} - c_{55})^2} \left(\frac{s l_3}{|l_1|} - \frac{l_1}{|l_3|} \right) \delta^*, \quad (3.37)$$

which can be expressed in terms of frequency f and simplified to obtain

$$\dot{\Omega} \approx \frac{-A\pi^2 f^2}{v} \frac{c_{33}^2}{(c_{33} - c_{55})^2} |l_1 l_3| (l_1^2 - l_3^2) (l_1^2 - s l_3^2) \delta^*. \quad (3.38)$$

Now all the angular dependency in $l_1 = \sin(\psi)$ and $l_3 = \cos(\psi)$ can be joined using the angle ψ between the wave propagation direction and the symmetry axis. To further simplify the expression above, we can limit our search to the first quadrant (ψ from 0 to 90 degrees), where s can be shown to have value +1 for small δ^* values and $2c_{55} \leq c_{33}$, and l_1 and l_3 have both positive values. Taking this into account, we can introduce the angular function $F(\psi)$ defined as

$$F(\psi) = \frac{1}{2} \sin(2\psi) \cos^2(2\psi), \quad (3.39)$$

so that our final form of the peak amplitude of the qP rotation rate is

$$\dot{\Omega} \approx \frac{-A\pi^2 f^2}{v} \frac{c_{33}^2}{(c_{33} - c_{55})^2} F(\psi) \delta^*. \quad (3.40)$$

The function $F(\psi)$ has maximum value $F(\psi)_{\max} \approx 0.1924$. If we additionally take $v = \alpha_0$ as an approximated velocity, the maxima can be estimated out of known values as

$$\dot{\Omega}_{\max} \approx 0.1924 \frac{A\pi^2 f^2 \alpha_0^3}{(\alpha_0^2 - \beta_0^2)^2} \delta^*. \quad (3.41)$$

Using the values of Table 3.3 we obtain, for $\delta^* = 0.1$, peak values of $\dot{\Omega}_{\max}^1 \approx 2.2 \times 10^{-11}$, $\dot{\Omega}_{\max}^2 \approx 4.6 \times 10^{-7}$, $\dot{\Omega}_{\max}^3 \approx 2.1 \times 10^{-6}$, and $\dot{\Omega}_{\max}^4 \approx 4.1 \times 10^{-7}$ all in rad/s. These values are in good agreement with the ones shown in Figures 3.3-3.6 when $\varepsilon = 0$, thus validating our approximation.

For weak anisotropy, instead of δ^* , Thomsen (1986) defined a simpler anisotropy parameter δ , which relates to ε and δ^* as

$$\delta = \frac{1}{2} \left[\varepsilon + \frac{\delta^*}{(1 - \beta_0^2 / \alpha_0^2)} \right]. \quad (3.42)$$

Using our assumption of $\varepsilon=0$, the peak value of qP rotation rate now can be estimated as

$$\dot{\Omega}_{\max} \approx 0.3848 \frac{A\pi^2 f^2 \alpha_0}{(\alpha_0^2 - \beta_0^2)} \delta. \quad (3.43)$$

The formula (3.43) can then be used to estimate the maximum peak qP rotation rate values to be expected in zones displaying weak anisotropy.

In order to obtain our expression, we have assumed that when $\varepsilon=0$ the velocity depends weakly on δ^* . To make an estimate of its influence, we will further use for simplicity the common relation $c_{33} = 3c_{55}$. Then the expression of D collapses to

$$D = 2c_{55} \sqrt{1 + \delta^* l_1^2 l_3^2}. \quad (3.44)$$

In this expression, a variation from $\delta^*=0$ to $\delta^*=1$ produces a 12% increase in the D value. The qP wave velocity is in this case

$$v = \sqrt{\frac{4c_{55} + D}{2\rho}}, \quad (3.45)$$

which will change by less than 2% when using $\delta^*=1$ with respect to the velocity obtained with $\delta^*=0$. Hence we consider the approximation correct. The non-linearity observed in the Figures 3.3 to 3.6 must then come from the second- and higher-order terms that we have ignored in our expansion.

3.6 Extracting Anisotropic Parameters from Point Measurements of Translational and Rotational Motions of qP Waves

Since the amplitudes of the qP rotational motions generated in anisotropic materials are big enough to be observed and recorded, one of the key questions is: can we extract additional information about material properties by using qP rotations? In this section we show theoretical equations that allow estimating two Thomsen parameters, ε and δ^* , from point measurements of both translational and

rotational motions of qP waves. Here we assume that the propagation direction \mathbf{l} of the considered plane wave is known. The density ρ , vertical P- and S-wave velocities α_0 and β_0 are considered to be available, coming from previous studies of the region.

From equation (3.1), translational accelerations of body waves can be inferred by taking the time derivative of the displacement twice

$$\ddot{\mathbf{u}} = -A\mathbf{n}\omega^2 \exp\left[i\omega\left(t - \frac{1}{v}\mathbf{l}\cdot\mathbf{x}\right)\right]. \quad (3.46)$$

Combining equations (3.3) and (3.46) we obtain

$$\frac{\ddot{\mathbf{u}}}{\dot{\Omega}} = 2v \begin{pmatrix} n_1 / (l_2 n_3 - l_3 n_2) \\ n_2 / (l_3 n_1 - l_1 n_3) \\ n_3 / (l_1 n_2 - l_2 n_1) \end{pmatrix}. \quad (3.47)$$

The polarization components n_i ($i = 1, 2, 3$) can be determined from translational measurements using

$$n_i = \frac{\ddot{u}_i}{\sqrt{\ddot{u}_1^2 + \ddot{u}_2^2 + \ddot{u}_3^2}}. \quad (3.48)$$

Equations (3.47) and (3.48) indicate that, knowing the propagation direction \mathbf{l} , the phase velocity v of a certain plane wave can be calculated from joint measurements of its translational and rotational motions recorded at a single location.

From (3.20) and (3.21) we can further infer

$$c_{33} = \rho\alpha_0^2, \quad (3.49)$$

$$c_{55} = \rho\beta_0^2. \quad (3.50)$$

Without loss of generality, we can simplify our study by considering wave propagation in a $(\mathbf{e}_1, \mathbf{e}_3)$ plane which contains the propagation azimuth. The polarization form expressed by equation (3.15) now can be rewritten by

$$\frac{\ddot{u}_1}{\ddot{u}_3} = s \sqrt{\frac{c_{55}l_1^2 + c_{33}l_3^2 - \rho v^2}{c_{11}l_1^2 + c_{55}l_3^2 - \rho v^2}}. \quad (3.51)$$

As all other parameters involved in (3.51) are known, c_{11} is fully determined as

$$\begin{aligned} c_{11} &= \frac{(c_{55}l_1^2 + c_{33}l_3^2 - \rho v^2)\ddot{u}_3^2 - (c_{55}l_3^2 - \rho v^2)\ddot{u}_1^2}{l_1^2 \ddot{u}_1^2} \\ &= \frac{(\beta_0^2 l_1^2 + \alpha_0^2 l_3^2 - v^2)\rho \ddot{u}_3^2 - (\beta_0^2 l_3^2 - v^2)\rho \ddot{u}_1^2}{l_1^2 \ddot{u}_1^2}. \end{aligned} \quad (3.52)$$

Using equations (3.14)₃ and (3.14)₄ that define phase velocity of qP waves one can obtain

$$\begin{aligned} (c_{13} + c_{55})^2 &= \frac{(2\rho v^2 - c_{11}l_1^2 - c_{33}l_3^2 - c_{55})^2 - [(c_{11} - c_{55})l_1^2 + (c_{55} - c_{33})l_3^2]^2}{4l_1^2 l_3^2} \\ &= \frac{(\rho v^2 - c_{11}l_1^2 - c_{55}l_3^2)(\rho v^2 - c_{55}l_1^2 - c_{33}l_3^2)}{l_1^2 l_3^2} \\ &= \frac{\rho^2}{l_1^2 l_3^2} \frac{\ddot{u}_3^2}{\ddot{u}_1^2} (\beta_0^2 l_1^2 + \alpha_0^2 l_3^2 - v^2)^2. \end{aligned} \quad (3.53)$$

Substituting the determined parameters c_{11} , c_{33} , c_{55} and $(c_{13} + c_{55})^2$ into (3.22) and (3.24) two measures of anisotropy ε and δ^* are extracted as follows

$$\varepsilon = \frac{(\beta_0^2 l_1^2 + \alpha_0^2 l_3^2 - v^2)\ddot{u}_3^2 - (\beta_0^2 l_3^2 + \alpha_0^2 l_1^2 - v^2)\ddot{u}_1^2}{2\alpha_0^2 l_1^2 \ddot{u}_1^2}, \quad (3.54)$$

$$\delta^* = \frac{1}{\alpha_0^4 l_1^2 \ddot{u}_1^2} \left[\frac{\ddot{u}_3^2}{l_3^2} (\beta_0^2 l_1^2 + \alpha_0^2 l_3^2 - v^2)^2 - (\alpha_0^2 - \beta_0^2) E \right], \quad (3.55)$$

$$\text{with } E = \frac{1}{2} \{ (\beta_0^2 l_1^2 + \alpha_0^2 l_3^2 - v^2)\ddot{u}_3^2 - [\beta_0^2 - v^2 - (\alpha_0^2 - \beta_0^2)l_1^2] \ddot{u}_1^2 \}.$$

Equations (3.47), (3.54), and (3.55) clearly demonstrate that, in theory, two Thomsen parameters ε and δ^* can be constrained from point measurements of translational and rotational motions of qP waves propagating in any TI medium.

3.7 Discussion and Conclusions

The results obtained in this chapter under the assumption of plane wave propagation show that 1) anisotropic behavior can be recognized by the variations of the rotational wavefield, especially by the appearance of qP rotations; 2) for all body waves in homogeneous anisotropic media, no rotational motion around the wave-propagation direction is generated; 3) amplitudes of qP rotation rates in TI media are constrained by two Thomsen parameters ε and δ^* ; 4) for strong local earthquakes and typical reservoir situations qP rotation signals are significant, recordable, and can be used for inverse problems; 5) two Thomsen parameters ε and δ^* can be extracted, theoretically, from collocated point measurements of translational and rotational motions of qP waves in TI media.

It should be noted that our original motivation to study the relation between anisotropy and rotational motions comes from efforts to explain the observed P coda rotations reported by Igel et al. (2007) and Pham et al. (2009b). At the beginning of this study, it was unclear whether rotational motions induced by qP waves in anisotropic media contribute to the observed rotational signals in the P coda. Related to this several results obtained in the present study need to be mentioned: 1) Although anisotropy does generate qP rotations, for tele-seismic wave fields the rotational energy induced by anisotropic effects is smaller than the observed one in the P-coda; 2) Equations (3.3) and (3.46) in the present study indicate that anisotropic qP rotations have the same wave forms as translational motions. The amplitudes of translational and rotational motions of qP waves are scaled by a certain factor defined by equation (3.47). This implies that qP rotations induced by anisotropic effects must appear at the onset of the P wave like for translational motions. However, as reported by Pham et al. (2009b), the P coda rotations observed at the Wettzell station come later than the appearance of direct P waves. These results demonstrate that anisotropic qP rotational signals can not be the main cause of the observed P coda rotations. The difference of arrival time of anisotropic qP rotational motions and scattering P coda rotations can be used to separate these two motion types for specific purposes when a heterogeneous medium is present.

In summary, we conclude that rotational motions contain additional information about anisotropy and that joint measurements of translational and rotational motions of qP waves at only one point in anisotropic media allow (in theory, at least) constraining anisotropic parameters independently of travel time information, thus might further allow one to recover time dependent changes in anisotropy which may be a matter of interest for volcanos, earthquake forecasting, or reservoir problems. The mentioned results not only demonstrate the potential

benefit of measurements of rotational ground motions but also pose several issues that need to be addressed in the future:

- 1) In the present study we only focus on qP waves whose rotational motions are completely independent of the Thomsen parameter γ . Thus, the determination of this measure of S anisotropy (i.e., γ) is out of the framework of this chapter. Theoretically, qS motions also contain additional information. Can we constrain the Thomsen parameter γ by using measurements of rotational motions of qS waves? What additional information can be extracted if these motions are used?
- 2) With body waves propagating in homogeneous (isotropic or anisotropic) media, as indicated in the present study, no rotational motion around the propagation direction is generated. This opens an opportunity to investigate scattering properties of heterogeneous media based on variations of rotational motions around the wave propagation direction.

Finally, the applicability of the presented theory to real data will rest on the ability to develop reliable sensor (borehole and surface) for rotational motions with broad enough frequency band width and dynamic range.

Outlook

The results obtained in this dissertation show that the contributions of tilt-ring laser coupling, topographic scattering, and anisotropic effects to the observed P coda rotations at Wettzell are very small and can be neglected. P-SH scattering in the random crust can explain the observations. Under the assumption of this scattering type, the numerical simulations based on the ADER-DG method are successful in reproducing the observations (i.e., P coda rotations). Furthermore, rotational motions contain additional information. The partitioning of P and S energy indicated by the stabilization of the ratio of energies of vertical rotation rate and vertical translation velocity after the onset of P wave is an important constraint on scattering properties of a random medium. By analyzing the observed and modeling rotational and translational signals of wave propagation through random media, velocity perturbation value about 5% for the Wettzell area is obtained. The correlation length of scatterers is not well-constrained in this approach. From another aspect, anisotropic behavior can be recognized by the variations of the rotational wavefield, especially by the appearance of qP rotations which should be zero in homogeneous isotropic media. Although for tele-seismic wave fields the energy of qP rotations induced by anisotropic effects is insignificant, for strong local earthquakes and typical reservoir situations qP rotation signals are significant, recordable, and can be used for inverse problems. Joint measurements of translational and rotational motions of qP waves at only one point in anisotropic media allow (in theory, at least) constraining anisotropic parameters independently of travel time information, thus might further allow one to recover time dependent changes in anisotropy.

In practice, when a heterogeneous anisotropic medium is present, both scattering P coda rotations and qP anisotropic rotations may be involved. At this point, it is worth to remind the characters of each motion type. Scattering P coda rotations usually come from every direction, and later than the appearance of the direct P wave. Energy of this motion type depends on its wave length, thus also depends on the frequency. However, qP anisotropic rotations arrival at the same time with translational motions of direct P wave, strongly depend on the wave propagation

direction. Amplitudes of qP rotation rates and corresponding translational accelerations are scaled by a factor which is independent of frequency. Thus, to separate these two motion types for specific purposes, investigations of the energy variations of the motions as a function of time, direction, and frequency are necessary.

The presented results lead to general conclusions that 1) P-SH scattering in the random crust is the main cause of the P-coda observations; and 2) rotational motions contain additional information – compared to standard translational observations – and that joint measurements of translational and rotational motions at only one point allow extracting the information. The results clearly demonstrate the potential benefit of measurements of co-seismic rotational ground motions. They also emphasize the importance of the amplitude content of seismic signals in recovering more information that may not be provided by common phase investigations.

Finally, several open questions and issues need to be addressed in future studies:

- 1) As noted in the first chapter of this study, for strong motions at near source co-seismic tilt motions may be significant. In theory, tilt signals caused by body waves contain information of physical (P and S) velocities. How can we constrain these parameters from tilt measurements?
- 2) Rotation sensors clearly offer a direct measurement of S energy. The distribution of cross-correlation coefficients between rotation rate and transverse acceleration as a function of time and cut-off period is shown as an effective tool to separate direct S waves from the scattering field. Can this tool help in picking other specific seismic phases to further recover the subsurface structure?
- 3) Can we constrain Thomsen parameter γ (the measure of S anisotropy) by using measurements of rotational motions of qS waves? What additional information can be extracted if these motions are used?
- 4) Theoretically, rotational motions of S waves contain information about the seismic source. Do additional rotational observations allow tighter constraints on source parameters?
- 5) Since body waves propagating in homogeneous (isotropic or anisotropic) media generate no rotational motion around the propagation direction, one now can investigate scattering properties of heterogeneous media based on variations of rotational motions around the wave propagation direction.

To go further with the presented questions and issues, reliable sensors (borehole and surface) for rotational motions with broad enough frequency bandwidth and dynamic range and more real data are necessary.

Data and Resources

The observed seismograms of period 2003-2004 and the topographical data of the Wetzell area used in this study were provided by the Geophysics Section, Ludwig Maximilians University Munich. The seismograms of the events occurred after September of 2007 can be obtained from the WebDC - Integrated Seismological Data Portal at <http://www.webdc.eu/arclink/query?sesskey=0841ed49> (last accessed March 2008).

Appendix A

Variations of the Normal Unit Vector of a Ring Laser

Under the effects of seismic waves, a ring laser may be both tilted and shifted. As a consequence, its normal unit vector \mathbf{n}_R is varied. Here we quantify this variation through cosines of angles between \mathbf{n}_R and the unit basis vectors \mathbf{n}_p , \mathbf{n}_Z , \mathbf{n}_N , \mathbf{n}_E of the rotation axis of the Earth, vertical, north-south, and east-west axes at the ring laser location, respectively. To do that we locate all the mentioned vectors in the Cartesian coordinate system Oxyz at the original location O of the ring laser, in which Ox, Oy and Oz are respectively corresponding with the local EW, NS, and vertical axes (Figure A1).

\mathbf{n}_Z , \mathbf{n}_N , and \mathbf{n}_E are defined in Oxyz system by

$$\mathbf{n}_Z \text{ (Oxyz)} = \{0, 0, 1\}, \quad (\text{A1})$$

$$\mathbf{n}_N \text{ (Oxyz)} = \{0, 1, 0\}, \quad (\text{A2})$$

$$\mathbf{n}_E \text{ (Oxyz)} = \{1, 0, 0\}. \quad (\text{A3})$$

The unit basis vector \mathbf{n}_p of the rotation axis of the Earth at first is considered in another Cartesian coordinate system O'X'Y'Z' (root point O' and O'Z', respectively, are the core point and the rotation axis of the Earth – see Figure A1). In this system, \mathbf{n}_p is determined by

$$\mathbf{n}_p \text{ (O'X'Y'Z')} = \{0, 0, 1\}. \quad (\text{A4})$$

On the other hand, let θ and λ , respectively, denote colatitude and latitude of the original location of the ring laser (Figure A1), we have

$$\cos(\text{Ox}, \text{O'Z'}) = 0, \quad (\text{A5a})$$

$$\cos(\text{Oy}, \text{O'Z'}) = \cos\left(\frac{\pi}{2} - \theta\right) = \cos(\lambda), \quad (\text{A5b})$$

$$\cos(\text{Oz}, \text{O'Z'}) = \cos(\theta) = \sin(\lambda). \quad (\text{A5c})$$

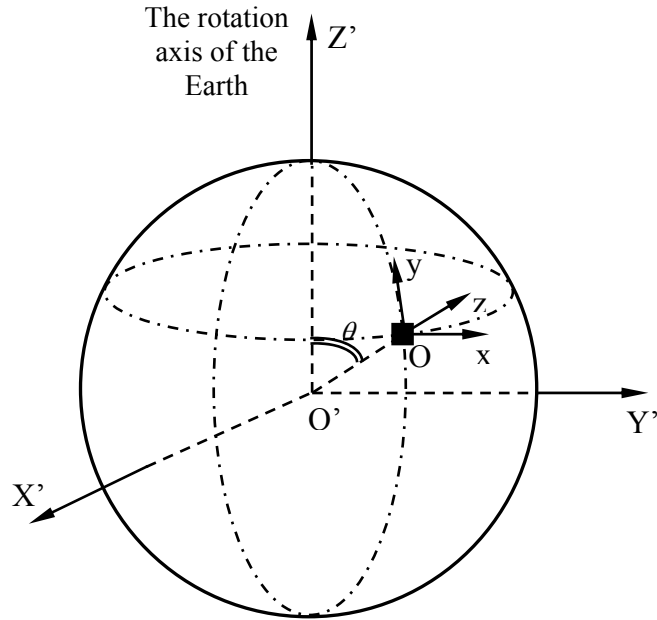


Figure A1. Illustration of ring laser location on the Earth's surface

Applying coordinate transformations and using (A4), (A5) one can infer the \mathbf{n}_p in the Oxyz system:

$$\mathbf{n}_p \text{ (Oxyz)} = \{0, \cos(\lambda), \sin(\lambda)\}. \quad (\text{A6})$$

For the normal unit vector \mathbf{n}_R of the ring laser, we locate it from the equation of the ring-laser plane in the Oxyz system which can be determined through three

non-linear points on the plane (see Appendix C). Assuming that when seismic waves arrive the ring laser is moved to a new certain location $R \{\Delta x, \Delta y, \Delta z\}$ in the Oxyz system (Figure A2). The seismically induced tilts of the ring laser sensor about x and y axes themselves are the horizontal components of rotations Ω_E, Ω_N , respectively (Cochard et al., 2006). Together with R, we choose R_1 in the line of intersection between the ring laser plane and xOz plane with distance $RR_1 = 1$, R_2 in the line of intersection between the ring laser plane and yOz plane with distance $RR_2 = 1$ to determine the equation of the ring laser plane. The coordinates of R_1 and R_2 in the Oxyz system can be easily determined as $R_1\{\cos(\Omega_N)+\Delta x, \Delta y, \sin(\Omega_N)+\Delta z\}$ and $R_2\{\Delta x, \cos(\Omega_E)+\Delta y, \sin(\Omega_E)+\Delta z\}$ (see Figure A2). Hence, the equation of the ring laser plane can be written as follows (Appendix C):

$$\begin{vmatrix} x - \Delta x & y - \Delta y & z - \Delta z \\ \cos(\Omega_N) & 0 & \sin(\Omega_N) \\ 0 & \cos(\Omega_E) & \sin(\Omega_E) \end{vmatrix} = 0$$

Or:

$$\begin{aligned} & -\cos(\Omega_E)\sin(\Omega_N)x - \sin(\Omega_E)\cos(\Omega_N)y + \cos(\Omega_E)\cos(\Omega_N)z \\ & + [\cos(\Omega_E)\sin(\Omega_N)\Delta x + \sin(\Omega_E)\cos(\Omega_N)\Delta y - \cos(\Omega_E)\cos(\Omega_N)\Delta z] = 0. \end{aligned} \quad (A7)$$

Equation (A7) implies that changes of location $R \{\Delta x, \Delta y, \Delta z\}$ affect the equation of the ring laser plane, but have no effect on the normal unit vector \mathbf{n}_R that can be inferred as follows (see Appendix C):

$$\mathbf{n}_R \text{ (Oxyz)} = \{n_1, n_2, n_3\}, \quad (A8a)$$

$$n_1 = \frac{-\cos(\Omega_E)\sin(\Omega_N)}{\sqrt{1 - \sin^2(\Omega_E)\sin^2(\Omega_N)}}, \quad (A8b)$$

$$n_2 = \frac{-\sin(\Omega_E)\cos(\Omega_N)}{\sqrt{1 - \sin^2(\Omega_E)\sin^2(\Omega_N)}}, \quad (A8c)$$

$$n_3 = \frac{\cos(\Omega_E)\cos(\Omega_N)}{\sqrt{1 - \sin^2(\Omega_E)\sin^2(\Omega_N)}}. \quad (A8d)$$

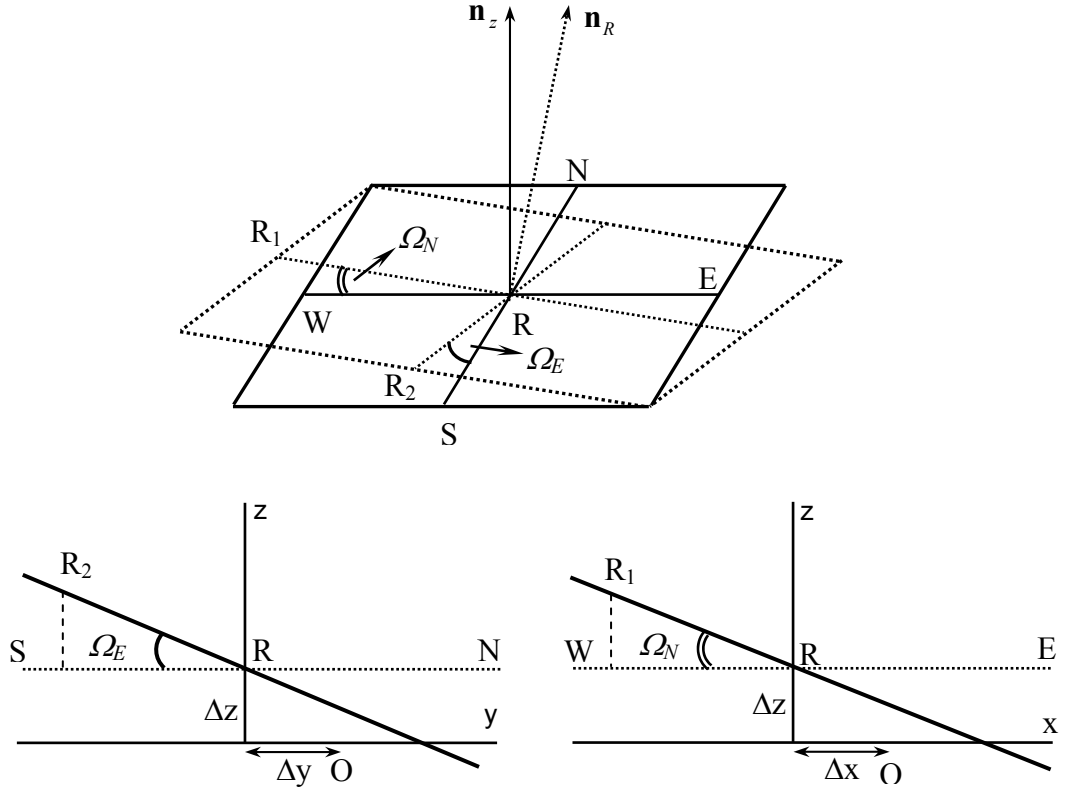


Figure A2. A ring laser sensor is tilted and shifted by seismic waves. $O\{0,0,0\}$ is the original location of the ring laser. $R\{\Delta x, \Delta y, \Delta z\}$ is new location of the ring laser under the effects of seismic wave. R_1 is chosen in the line of intersection between the ring laser plane and xOz plane with distance $RR_1 = 1$. R_2 is chosen in the line of intersection between the ring laser plane and yOz plane with distance $RR_2 = 1$.

Using (A1), (A2), (A3), (A6), and (A8), cosine of angles between normal unit vector \mathbf{n}_R of the ring laser and the unit basis vectors \mathbf{n}_P , \mathbf{n}_Z , \mathbf{n}_N , \mathbf{n}_E of the rotation axis of the Earth, vertical, north-south, and east-west axes at the ring laser location, respectively, are calculated by (see Appendix C):

$$\alpha_P = \frac{\cos(\Omega_N) \sin(\Lambda - \Omega_E)}{\sqrt{1 - \sin^2(\Omega_E) \sin^2(\Omega_N)}}, \quad (\text{A9a})$$

$$\alpha_Z = \frac{\cos(\Omega_E) \cos(\Omega_N)}{\sqrt{1 - \sin^2(\Omega_E) \sin^2(\Omega_N)}}, \quad (\text{A9b})$$

$$\alpha_N = \frac{-\sin(\Omega_E)\cos(\Omega_N)}{\sqrt{1-\sin^2(\Omega_E)\sin^2(\Omega_N)}}, \quad (\text{A9c})$$

$$\alpha_E = \frac{-\cos(\Omega_E)\sin(\Omega_N)}{\sqrt{1-\sin^2(\Omega_E)\sin^2(\Omega_N)}}. \quad (\text{A9d})$$

In seismology, Ω_E and Ω_N are small. The greatest value of the co-seismic tilts that has ever been observed is 4.0×10^{-4} rad (Nigbor, 1994). Thus, we can approximate (A9a,b,c,d) by

$$\alpha_P \approx \sin(\Lambda - \Omega_E), \quad (\text{A10a})$$

$$\alpha_Z \approx 1, \quad (\text{A10b})$$

$$\alpha_N \approx -\Omega_E, \quad (\text{A10c})$$

$$\alpha_E \approx -\Omega_N. \quad (\text{A10d})$$

Appendix B

Axis Transformations of Tilts

Assuming Cartesian coordinate system NZE is rotated an angle φ around Z to another coordinate system RZT (Figure B1). To set up the relationship between components of tilt in these coordinate systems, we start with the coordinate relationship between these two systems,

$$\begin{bmatrix} T \\ R \end{bmatrix} = \begin{bmatrix} \cos(\varphi) & -\sin(\varphi) \\ \sin(\varphi) & \cos(\varphi) \end{bmatrix} \begin{bmatrix} E \\ N \end{bmatrix} \quad (\text{B1})$$

$$\text{or} \quad T = \cos(\varphi)E - \sin(\varphi)N, \quad (\text{B2a})$$

$$R = \sin(\varphi)E + \cos(\varphi)N, \quad (\text{B2b})$$

$$\text{or} \quad E = \cos(\varphi)T + \sin(\varphi)R, \quad (\text{B2c})$$

$$N = -\sin(\varphi)T + \cos(\varphi)R. \quad (\text{B2d})$$

Calling U_Z the vertical component of displacement, the components of tilt around N , E , R , and T axes, respectively, are defined by (Cochard et al., 2006)

$$\Omega_N = -\frac{\partial U_Z}{\partial E}, \quad \Omega_E = \frac{\partial U_Z}{\partial N}, \quad (\text{B3})$$

$$\Omega_R = -\frac{\partial U_Z}{\partial T}, \quad \Omega_T = \frac{\partial U_Z}{\partial R}. \quad (\text{B4})$$

Now, using the chain rule leads to

$$\Omega_R = -\frac{\partial U_Z}{\partial T} = -\left(\frac{\partial U_Z}{\partial N} \frac{\partial N}{\partial T} + \frac{\partial U_Z}{\partial E} \frac{\partial E}{\partial T}\right), \quad (\text{B5})$$

$$\Omega_T = \frac{\partial U_Z}{\partial R} = \left(\frac{\partial U_Z}{\partial N} \frac{\partial N}{\partial R} + \frac{\partial U_Z}{\partial E} \frac{\partial E}{\partial R}\right). \quad (\text{B6})$$

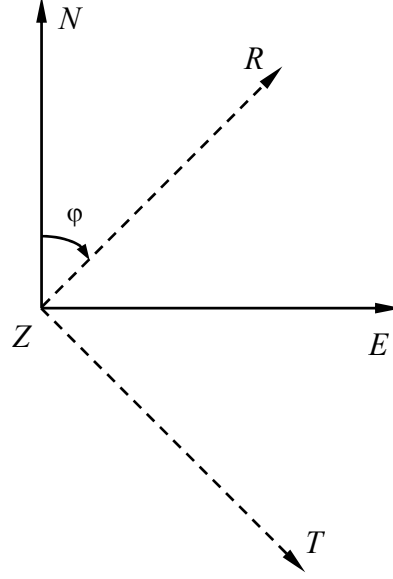


Figure B1. Axis transformations of tilts

From (B2c) and (B2d) we know that

$$\frac{\partial E}{\partial T} = \cos(\varphi), \quad \frac{\partial E}{\partial R} = \sin(\varphi), \quad \frac{\partial N}{\partial T} = -\sin(\varphi), \quad \frac{\partial N}{\partial R} = \cos(\varphi). \quad (\text{B7})$$

Combining (B3), (B5), (B6), and (B7) we have the relationship

$$\Omega_R = \Omega_E \sin(\varphi) - \Omega_N \cos(\varphi), \quad (\text{B8})$$

$$\Omega_T = \Omega_E \cos(\varphi) - \Omega_N \sin(\varphi), \quad (\text{B9})$$

$$\text{or} \quad \Omega_N = \Omega_R \cos(\varphi) - \Omega_T \sin(\varphi), \quad (\text{B10})$$

$$\Omega_E = \Omega_R \sin(\varphi) + \Omega_T \cos(\varphi). \quad (\text{B11})$$

Appendix C

Fundamental Formulas

1. Equation of a plane through given three non-linear points $M_1(x_1, y_1, z_1)$, $M_2(x_2, y_2, z_2)$, $M_3(x_3, y_3, z_3)$ can be determined by

$$\begin{vmatrix} x - x_1 & y - y_1 & z - z_1 \\ x_2 - x_1 & y_2 - y_1 & z_2 - z_1 \\ x_3 - x_1 & y_3 - y_1 & z_3 - z_1 \end{vmatrix} = 0. \quad (C1)$$

2. The normal unit vector of a plane $Ax + By + Cz + D = 0$ is expressed by

$$\left\{ \frac{A}{\sqrt{A^2 + B^2 + C^2}}, \frac{B}{\sqrt{A^2 + B^2 + C^2}}, \frac{C}{\sqrt{A^2 + B^2 + C^2}} \right\}. \quad (C2)$$

3. Cosine of angle between two vectors $\{A_1, B_1, C_1\}$ and $\{A_2, B_2, C_2\}$ can be calculated by

$$\frac{A_1 A_2 + B_1 B_2 + C_1 C_2}{\sqrt{A_1^2 + B_1^2 + C_1^2} \sqrt{A_2^2 + B_2^2 + C_2^2}}. \quad (C3)$$

Appendix D

Orthogonal System $\mathbf{l}, \boldsymbol{\theta}, \boldsymbol{\phi}$

The orthogonal system $\mathbf{l}, \boldsymbol{\theta}, \boldsymbol{\phi}$ used in Chapter 3 is defined as follows. With known unit vector $\mathbf{l} = (l_1, l_2, l_3)$, we set

$$\mathbf{p} = (l_1, -l_2, 0), \quad (\text{D1})$$

$$\mathbf{q} = (0, -l_3, l_2), \quad (\text{D2})$$

$$\mathbf{r} = (l_3, 0, -l_1). \quad (\text{D3})$$

If the magnitude of the cross product $|\mathbf{l} \times \mathbf{p}| > 0$, $\boldsymbol{\theta}$ and $\boldsymbol{\phi}$ are determined, respectively, by cross product of \mathbf{l} and \mathbf{p} and of \mathbf{l} and $\boldsymbol{\theta}$

$$\boldsymbol{\theta} = \mathbf{l} \times \mathbf{p} = (l_2 l_3, l_1 l_3, -2l_1 l_2), \quad (\text{D4})$$

$$\boldsymbol{\phi} = \mathbf{l} \times \boldsymbol{\theta} = (-2l_1 l_2^2 - l_1 l_3^2, l_2 l_3^2 + 2l_1^2 l_2, l_1 l_3^2 - l_2^2 l_3). \quad (\text{D5})$$

If $|\mathbf{l} \times \mathbf{p}| = 0$ and $|\mathbf{l} \times \mathbf{q}| > 0$, $\boldsymbol{\theta}$ and $\boldsymbol{\phi}$ are determined, respectively, by

$$\boldsymbol{\theta} = \mathbf{l} \times \mathbf{q} = (l_2^2 + l_3^2, -l_1 l_2, -l_1 l_3), \quad (\text{D6})$$

$$\boldsymbol{\phi} = \mathbf{l} \times \boldsymbol{\theta} = (0, l_3, -l_2). \quad (\text{D7})$$

If $|\mathbf{l} \times \mathbf{p}| = 0$ and $|\mathbf{l} \times \mathbf{q}| = 0$, $\boldsymbol{\theta}$ and $\boldsymbol{\phi}$ are determined, respectively, by

$$\boldsymbol{\theta} = \mathbf{l} \times \mathbf{r} = (-l_1 l_2, l_3^2 + l_1^2, -l_2 l_3), \quad (\text{D8})$$

$$\boldsymbol{\phi} = \mathbf{l} \times \boldsymbol{\theta} = (-l_3, 0, l_1). \quad (\text{D9})$$

Bibliography

- Aki, K. and P. G. Richards, 1980. *Quantitative Seismology: Theory and Methods*, W.H. Freeman and Company, San Francisco, California.
- Aki, K. and P. G. Richards, 2002. *Quantitative Seismology*, Second Edition, University Science Books, Sausalito, California.
- Awad, A. M. and J. L. Humar, 1984. Dynamic Response of Buildings to Ground Rotational Motions, *Canadian Journal of Civil Engineering*, **11**, 48-56.
- Bassin, C., G. Laske, and G. Masters, 2000. The Current Limits of Resolution for Surface Wave Tomography in North America, *EOS Trans AGU*, **81**, F897.
- Bernauer, M., A. Fichtner, and H. Igel, 2009. Inferring Near-Receiver Structure from Combined Measurements of Rotational and Translational Ground Motions, *Geophysics*, accepted.
- Bouchon, M., K. Aki, 1982. Strain, Tilt, and Rotation Associated with Strong Ground Motion in the Vicinity of Earthquake Faults, *Bull. Seismol. Soc. Am.*, **72**, 1717-1738.
- Booth, D.C, 2007. An Improved UK Local Magnitude Scale from Analysis of Shear and Lg-Wave Amplitudes, *Geophys. J. Int.*, **169**, 593-601, doi: 10.1111/j.1365-246X.2006.03324.x.
- Carcione, J. M., 2001. *Wave Fields in Real Media: Wave Propagation in Anisotropic, Anelastic and Porous Media* (Volume 31), PERGAMON, An Imprint of Elsevier Science.
- Chen, Y., L. Liu, H. Ge, B. Liu, and X. Qiu, 2008. Using an Airgun Array in a Land Reservoir as the Seismic Source for Seismotectonic Studies in Northern China: Experiments and Preliminary Results. *Geophysical Prospecting*, **56**, 601–612, doi:10.1111/j.1365-2478.2007.00679.x.

- Cochard, A., H. Igel, B. Schuberth, W. Suryanto, A. Velikoseltsev, U. Schreiber, J. Wassermann, F. Scherbaum, and D. Vollmer, 2006. Rotational Motions in Seismology: Theory, Observations, Simulation, in *Earthquake Source Asymmetry, Structural Media and Rotation Effects*, R. Teisseyre, M. Takeo, and E. Majewski (Editors), Springer-Verlag, New York, 391–412.
- Crampin, S., 1981. A Review of Wave Motion in Anisotropic and Cracked Elastic-Media, *Wave Motion*, **3**, 343-391.
- Crampin, S., R. A. Stephen, and R. McGonigle, 1982. The Polarization of P-Waves in Anisotropic Media, *Geophys. J. R. Astron. Soc.*, **68**, 477-485.
- Crampin, S., 1984. Effective Anisotropic Elastic-Constants for Wave Propagation through Cracked Solids, *Geophys. J. R. Astron. Soc.*, **76**, 135-145.
- Crampin, S., E. M. Chesnokov, and R. G. Hipkin, 1984. Seismic Anisotropy - the State of the Art II, *Geophys. J. R. Astron. Soc.*, **76**, 1-16.
- de la Puente, J., M. Käser, M. Dumbser, and H. Igel, 2007. An Arbitrary High Order Discontinuous Galerkin Method for Elastic Waves on Unstructured Meshes IV: Anisotropy, *Geophys. J. Int.*, **169**(3), 1210-1228, doi: 10.1111/j.1365-246X.2007.03381.x.
- de la Puente, J., 2008. *Seismic Wave Propagation for Complex Rheologies*, VDM Verlag, Dr. Müller, Saarbrücken, Germany.
- Dumbser, M., and M. Käser, 2006. An Arbitrary High Order Discontinuous Galerkin Method for Elastic Waves on Unstructured Meshes II: the Three-Dimensional Isotropic Case, *Geophys. J. Int.*, **167**(1), 319-336, doi:10.1111/j.1365-246X.2006.03120.x.
- Ferreira, A. and H. Igel, 2009. Rotational Motions of Seismic Surface Waves in a Laterally Heterogeneous Earth, *Bull. Seismol. Soc. Am.*, **99**, no. 2B, 1429-1436, doi: 10.1785/0120080149.
- Fichtner, A. and H. Igel, 2009. Sensitivity Densities for Rotational Ground Motion Measurements, *Bull. Seismol. Soc. Am.*, **99**, no. 2B, 1302-1314, doi: 10.1785/0120080064.
- Galitzin, F., 1914. Vorlesungen über Seismometrie. BG Teubner, Leipzig–Berlin (in German).
- Graizer, V. M., 2005. Effect of Tilt on Strong Motion Data Processing, *Soil Dyn. Earthq. Eng.*, **25**, 197-204.

- Graizer, V. M, 2006. Equation of Pendulum Motion Including Rotations and Its Implications to the Strong-Ground Motion, in *Earthquake Source Asymmetry, Structural Media and Rotation Effects*, 471-491.
- Guéguen, Y. and J. Sarout, 2009. Crack-Induced Anisotropy in Crustal Rocks: Predicted Dry and Fluid-Saturated Thomsen's Parameters, *Physics of the Earth and Planetary Interiors*, **172**, 116–124, doi:10.1016/j.pepi.2008.05.020.
- Huang, B. S., 2003. Ground Rotational Motions of the 1991 Chi-Chi, Taiwan, Earthquake as Inferred from Dense Array Observations, *Geophys. Res. Lett.*, **30**, no. 6, 1307–1310.
- Hennino, R., Trégourès N., Shapiro N. M., Margerin L., Campillo M., van Tiggelen B. A., and Weaver R. L., 2001. Observation of Equipartition of Seismic Waves, *Physical Review Letters*, **86**, 3447-3450, doi: 10.1103/PhysRevLett.86.3447.
- Hutton, L. K. and D.M. Boore, 1987. The M_L Scale in Southern California, *Bull. Seism. Soc. Amer.*, **77**, 2074-2097.
- Igel, H., A. Cochard, J. Wassermann, A. Flaws, U. Schreiber, A. Velikoseltsev, N. D. Pham, 2007. Broadband Observations of Earthquake Induced Rotational Ground Motions, *Geophys. J. Int.*, **168**, 182-196, doi: 10.1111/j.1365-246X.2006.03146x.
- Igel, H., U. Schreiber, A. Flaws, B. Schuberth, A. Velikoseltsev, A. Cochard, 2005. Rotational Motions Induced by the M8.1 Tokachi-oki Earthquake, September 25, 2003, *Geophys. Res. Lett.*, **32**, L08309, doi:10.1029/2004GL022336.
- Klimeš, L, 2002. Correlation Functions of Random Media, *Pure appl. geophys.*, **159**, 1811-1831.
- Larner, K., 1993, Dip-Moveout Error in Transversely Isotropic Media with Linear Velocity Variation in Depth, *Geophysics*, **58**, 1442-1453.
- Lay, T. and T. C. Wallace, 1995. *Modern Global Seismology*, Academic Press, San Diego, California.
- Lee, H. K.W., H. Igel, and M. D. Trifunac, 2009a. Recent Advances in Rotational Seismology, *Seismological Research Letters*, **80**(3), 479 – 490, doi: 10.1785/gssrl.80.3.479.

- Lee, H. K.W., M. Çelebi, M. I. Todorovska, and H. Igel, 2009b. Introduction to the Special Issue on Rotational Seismology and Engineering Applications, *Bull. Seismol. Soc. Am.*, **99**, no. 2B, 945–957, doi: 10.1785/0120080344.
- Li, H., L. Sun, and S. Wang, 2001. Improved Approach for Obtaining Rotational Components of Seismic Motion. *Transactions*, SmiRT, **16**, 1-8.
- Li, H., L. Sun, and S. Wang, 2002. Frequency Dispersion Characteristics of Phase Velocities in Surface Wave for Rotational Components of Seismic Motion. *Journal of Sound and Vibration*, **258** (5), 815-827.
- McLeod, D.P., G. E. Stedman, T. H. Webb, and U. Schreiber, 1998. Comparison of Standard and Ring Laser Rotational Seismograms, *Bull. Seismol. Soc. Am.*, **88**, 1495-1503.
- Newmark, N. M., 1969. Torsion in Symmetrical Buildings, *Proc. Fourth World Conference on Earthquake Engineering, Santiago, Chile*, **3**, 19-32.
- Nigbor, R. L., 1994. Six-Degree-of-Freedom Ground-Motion Measurement. *Bull. Seism. Soc. Amer.*, **84**, 1655-1669.
- Nigbor, R. L., J. R. Evans, and C. R. Hutt, 2009. Laboratory and Field Testing of Commercial Rotational Seismometers, *Bull. Seismol. Soc. Am.*, **99**, no. 2B, 1215–1227, doi: 10.1785/0120080247.
- Pancha, A., T. H. Webb, G. E. Stedman, D. P. McLeod, and U. Schreiber, 2000. Ring Laser Detection of Rotations from Teleseismic Waves, *Geophys. Res. Lett.*, **27**, 3553-3556.
- Pham, D.N., H. Igel, J. Wassermann, A. Cochard, U. Schreiber, 2009a. The Effects of Tilt on Interferometric Rotation Sensors, *Bull. Seismol. Soc. Am.*, **99**, no. 2B, 1352-1365, doi: 10.1785/0120080181.
- Pham, D.N., H. Igel, J. Wassermann, M. Käser, J. de la Puente, U. Schreiber, 2009b. Observations and Modelling of Rotational Signals in the P-Coda: Constraints on Crustal Scattering, *Bull. Seismol. Soc. Am.*, **99**, no. 2B, 1315-1332, doi: 10.1785/0120080101.
- Pham, D.N., H. Igel, J. de la Puente, M. Käser, and M. A. Schoenberg, 2009c. Rotational Motions in Homogeneous Anisotropic Elastic Media, *Geophysics*, submitted.

- Pillet, R. and J. Virieux, 2007. The Effects of Seismic Rotations on Inertial Sensors, *Geophys. J. Int.*, **171**, 1314–1323, doi: 10.1111/j.1365-246X.2007.03617.x
- Pillet, R., A. Deschamps, D. Legrand, J. Virieux, N. Béthoux, and B. Yates, 2009. Interpretation of Broadband Ocean-Bottom Seismometer Horizontal Data Seismic Background Boise, *Bull. Seismol. Soc. Am.*, **99**, no. 2B, 1333–1342.
- Richter, C. F., 1958. *Elementary Seismology*, W. H. Freeman, San Francisco, California.
- Sams, M. S., M. H. Worthington, and M. S. Khanshir, 1993. A Comparison of Laboratory and Field Measurements of P-Wave Anisotropy, *Geophys. Prosp.*, **41**, 189–206.
- Schreiber, U., H. Igel, A. Cochard, A. Velikoseltsev, A. Flaws, B. Schuberth, W. Drewitz, and F. Müller, 2005. The GEOsensor Project: A New Observable for Seismology, in *Observation of the System Earth from Space*, J. Flury, R. Rummel, C. Reigber, M. Rothacher, G. Boedecker, and U. Schreiber (Editors), Springer, Berlin, 427–443.
- Schreiber, U., G. E. Stedman, H. Igel, and A. Flaws, 2006. Ring Laser Gyroscopes as Rotation Sensors for Seismic Wave Studies, in *Earthquake Source Asymmetry, Structural Media and Rotation Effects*, R. Teisseyre, M. Takeo, and E. Majewski (Editors), Springer-Verlag, New York, 377–390.
- Schreiber, K. U., J. N. Hautmann, A. Velikoseltsev, J. Wassermann, H. Igel, J. Otero, F. Vernon, and J.-P. R. Wells, 2009. Ring Laser Measurements of Ground Rotations for Seismology, *Bull. Seismol. Soc. Am.*, **99**, no. 2B, 1190–1198.
- Shapiro, N. M., M. Campillo, L. Margerin, S. K. Singh, V. Kostoglodov, and J. Pacheco, 2000. The Energy Partitioning and the Diffusive Character of the Seismic Coda, *Bull. Seism. Soc. Am.*, **90**, 655–665.
- Singh, S. K., M. Santoyo, P. Bodin, and J. Gomberg, 1997. Dynamic Deformations of Shallow Sediments in Valley of Mexico, part II: Single-Station Estimates, *Bull. Seism. Soc. Am.*, **87**, 540–550.
- Spudich, P., L. K. Steck, M. Hellweg, J. B. Fletcher, and L. M. Baker, 1995. Transient Stresses at Parkfield, California, Produced by the M 7.4 Landers

- Earthquake of June 28, 1992: Observations from the UPSAR Dense Seismograph Array, *J. Geophys. Res.*, **100**, no. B1, 675–690.
- Stein, S. and M. Wyssession, 2003. *An Introduction to Seismology, Earthquake, and Earth Structure*, Blackwell Publishing, Oxford.
- Suryanto, W., H. Igel, J. Wassermann, A. Cochard, B. Schuberth, D. Vollmer, F. Scherbaum, U. Schreiber, and A. Velikoseltsev, 2006. First Comparison of Array-Derived Rotational Ground Motions with Direct Ring Laser Measurements, *Bull. Seismol. Soc. Am.*, **96**, 2059-2071.
- Suryanto, W., 2006. Rotational Motions in Seismology, Theory and Application. PhD. Dissertation, LMU Munich (<http://edoc.ub.uni-muenchen.de/7850/>).
- Stedman, G. E., 1997. Ring Laser Tests of Fundamental Physics and Geophysics, *Rev. Progr. Phys.*, **60**, 615-688.
- Stedman, G. E., Z. Li, and H. R. Bilger, 1995. Sideband Analysis and Seismic Detection in Large Ring Laser, *Appl. Opt.*, **34**, 7390-7396.
- Takeo, M. & H. M. Ito, 1997. What Can Be Learned from Rotational Motions Excited by Earthquakes? *Geophys. J. Int.*, **129**, 319-329.
- Takeo, M., 1998. Ground Rotational Motions Recorded in Near-Source Region of Earthquakes. *Geophys. Res. Lett.*, **25**, 789-792.
- Thomsen, L., 1986. Weak Elastic Anisotropy, *Geophysics*, **51**, 1954–1966.
- Trifunac, M. D. and M. I. Todorovska, 2001. A Note on the Usable Dynamic Range of Accelerographs Recording Translation. *Soil Dyn. and Earth. Eng.*, **21**(4), 275-286.
- Trifunac, M. D., 2009. Review: rotations in structural response, *Bull. Seismol. Soc. Am.*, **99**, no. 2B, 968–979.
- Tsvankin, I., 1996. P-wave Signatures and Notation for Transversely Isotropic Media: An Overview, *Geophysics*, **61**, no. 2, 467-483.
- Wang, Z., 2002. Seismic Anisotropy in Sedimentary Rocks, Part 2: Laboratory Data, *Geophysics*, **67**, no. 5, 1423–1440.

- Wassermann, J., S. Lehndorfer, H. Igel, U. Schreiber, 2009. Performance Test of a Commercial Rotational Motion Sensor, *Bull. Seismol. Soc. Am.*, **99**, no. 2B, 1449-1456; doi: 10.1785/0120080157.

Curriculum Vitae

Pham, Dinh Nguyen

Date and Place of Birth

11. 11. 1972

Thaibinh, Vietnam

Education

October 2005 – July 2009

PhD Student in Seismology at the Dept. of Earth and Environmental Sciences, Ludwig-Maximilians-Universität München, Germany.

2000 - 2002

Master Student in Geophysics at the College of Science, Hanoi National University, Hanoi, Vietnam.

1989 - 1994

Study Geophysics at the University of Mining and Geology, Hanoi, Vietnam.

1987 - 1989

Le-Quy-Don High School, Thaibinh, Vietnam.

1979 - 1989

Primary School in Thaibinh, Vietnam

Employment Record

1997 - present

Researcher, permanent position at the Institute of Geophysics, Vietnamese Academy of Science and Technology, Hanoi, Vietnam.

1995 - 1996

Research contract at the Institute of Geophysics, Vietnamese Academy of Science and Technology, Hanoi, Vietnam.

Publications Related to the PhD Project

- Pham, D.N., H. Igel, J. de la Puente, M. Käser, and M. A. Schoenberg, 2009. Rotational Motions in Homogeneous Anisotropic Elastic Media, *Geophysics*, submitted.
- Pham, D. N., H. Igel, M. Käser, 2009. Possible Use of Rotational Ground Motions in Oilfield Studies - Part II: Synthetic Seismograms and Processing Results, *A report under a Confidential Information Disclosure Agreement between the Ludwig-Maximilians-University, Munich, and Schlumberger K.K., Japan*.
- Igel, H., D. N. Pham, M. Bernauer, A. Fichtner, M. Käser, J. Wassermann, 2009. Possible Use of Rotational Ground Motions in Oilfield Studies - Part I: Theory, Observations, Processing, *A report under a Confidential Information Disclosure Agreement between the Ludwig-Maximilians-University, Munich, and Schlumberger K.K., Japan*.
- Pham, D.N., H. Igel, J. Wassermann, M. Käser, J. de la Puente, U. Schreiber, 2009. Observations and Modelling of Rotational Signals in the P-Coda: Constraints on Crustal Scattering, *Bull. Seismol. Soc. Am.*, **99**, no. 2B, 1315-1332, doi: 10.1785/0120080101.
- Pham, D.N., H. Igel, J. Wassermann, A. Cochard, U. Schreiber, 2009. The Effects of Tilt on Interferometric Rotation Sensors, *Bull. Seismol. Soc. Am.*, **99**, no. 2B, 1352-1365, doi: 10.1785/0120080181.
- Igel, H., A. Cochard, J. Wassermann, A. Flaws, U. Schreiber, A. Velikoseltsev, N. D. Pham, 2007. Broadband Observations of Earthquake Induced Rotational Ground Motions, *Geophys. J. Int.*, **168**, 182-196, doi: 10.1111/j.1365-246X.2006.03146x.